Czech Technical University in Prague

Faculty of Electrical Engineering

Department of Electrical Power Engineering

**Doctoral Thesis**

Lavr Vetoshkin

# Enhancing power system stability with grid-forming control of power converters

| | |
|---|---|
| Ph.D. Programme: | P2612 - Electrical Engineering and Information Technology |
| Branch of study: | 3907V001 - Electrical Power Engineering |
| Supervisor: | doc. Ing. Zdeněk Müller, Ph.D. |
| Supervisor-Specialist: | doc. Dr. Ing. Jan Kyncl |

Prague, August 2022

## Acknowledgements

I would like to thank my supervisor, doc. Ing. Zdeněk Müller, Ph.D., for his support and advice throughout my studies. Most importantly I want to thank my family for giving me opportunity and support in pursuing the degree.

I hereby declare that I have completed this thesis with the topic "Enhancing power system stability with grid-forming control of power converters" independently and that I have included a full list of used references.

In ................ date ................ signature of the author

## Abstrakt:

Rostoucí penetrace obnovitelných zdrojů energie v elektrizační soustavě vede ke snížení setrvačnosti systému z hlediska energie akumulované v rotujících hmotách. Schopnost elektrizační soustavy integrovat vetší podíl OZE bez ovlivnění stability závisí na okamžitě dostupném výkonu. Proto pro systém s nízkou setrvačností je možným řešením emulace setrvačnosti pomocí výkonových měničů, které připojují OZE k systému. Tato disertační práce zkoumá různé strategie řízení, které emulují setrvačnost v systému. V práci jsou porovnávány tři hlavní kategorie: grid-forming, grid-following a klasické vektorové řízení. Práce prezentuje výsledky modální analýzy a numerických simulací, které byly provedeny s použitím IEEE modelů testovacích systémů. Práce zkoumá, jak umístění virtuální setrvačnosti ovlivňuje stabilitu systému. Výsledky prezentované studie ukazují, že především dva faktory ovlivňují mody systému: umístění prvku v síti a algoritmus, který je použit pro implementaci virtuální setrvačnosti. Dále autor navrhuje stabilizátor napětí v stejnosměrném meziobvodu pro elektrárnu OZE s akumulací energie. Toto vylepšení zvyšuje stabilitu systému, který se dokonce chová jako konvenční synchronní generátor. Práce také analyzuje možnost aplikace grid-forming řízení na STATCOM. Pro porovnání navrhnuté strategie řízení s tradičním vektorovým řízením byla použita modální analýza, numerické simulace a přímá Ljapunovova metoda. Výsledky provedených výpočtů názorně ukazují, že aplikace grid-forming řízení STATCOMu skutečně zlepšuje stabilitu systému a umožnuje systému zůstat v synchronním chodu při delších dobách trvání poruch.

## Klíčová slova:

Stabilita elektrizační soustavy, Přechodná stabilita, Virtuální setrvačnost, Obnovitelné zdroje energie

## Abstract:

The challenge of low inertia in the system has appeared due to the higher penetration of renewable energy sources. The system's ability to accommodate a larger share of RES without losing stability is dependent upon inertia. Therefore, a possible solution for a low inertia system is to emulate inertia response using power converters that connect RES to the system. The thesis investigates different control techniques that emulate inertia in the system. There are three main categories that are compared in this work: grid-forming, grid-following, and traditional control. The thesis presents the results of small-signal analysis and numerical simulations, which were conducted using IEEE benchmark system models. Also, the work presents an analysis of virtual inertia placement in the system. The results of the presented study show that two factors play a significant role in the small-signal stability: the location and the algorithm that is used for virtual inertia implementation. The author also proposes a DC bus voltage stabilizer for the RES power plant with an energy storage system. That improvement enhances the system's stability and even allows to replace a conventional generator. Lastly, the work investigates the possibility of application of a grid-forming control to a STATCOM. Small-signal analysis, numerical simulations, and Lyapunov theory were applied in order to compare the researched approach to traditional vector control. The presented results show that the application of grid-forming control to STATCOMs might indeed increase system stability and allow the system to withstand longer clearing times.

## Keywords:

Power system stability, Transient stability, Virtual inertia, Renewable Energy Sources

# Contents

# 1. Modern Power Systems

## 1.1 Overview of current development in power systems

Energy systems have been transitioning from conventional energy sources toward renewable generation. Electric power systems are a vital part of more sustainable industrial systems since electricity can power not only traditional loads but also transportation and heating. The construction of renewable power plants, especially wind and solar, is supported by governments worldwide. The change in the energy landscape is drastic, according to [1] global electricity production from Renewable Energy Sources (RES) rose from 2% to more than 10%. The European commitment to energy transition is stronger than anywhere else. As a result, RES generation in European countries has overtaken nuclear for the first time in 2020 [1]. Germany is one of the countries that pursue zero-emission goals and has built a tremendous amount of RES generation capacity. Fig. 1.1 visualizes ENTSO-E data that show the change in installed capacity by energy source. According to the data, Germany has a higher total installed capacity of RES than more conventional sources combined. The shift towards sustainable energy sources is significant in other parts of the world as well. For example, in Australia, wind and solar accounted for 22 % of total electricity production in 2020-2021.

The energy transition changes the way the electric grid operates. In conventional power systems, the electricity is predominantly generated by synchronous generators. Thus, a conventional grid naturally responds to a significant power imbalance by releasing or storing some of the power in the inertia of synchronous generators. The inertia response plays a major role in the dynamic stability of the system. Furthermore, under normal operation, dispatchers can decide how much power each power plant should inject into the system, and thus, predicted power demand can be easily met. On the contrary, the power production by RES naturally fluctuates during even a small period of time. It is very difficult to predict how much irradiance will be or how strong the wind will be where the power plant is. Therefore, it complicates day-ahead power dispatching and requires more effort to meet power demand. To accomodate large share of RES, the grid has to be very flexible and respond quickly to possible power imbalances. Nevertheless, it is not only a disadvantage of RES power plants. They require converter-generation interface (CIG) units that are fundamentally different than synchronous machines. Power converters do not have inertia that can respond to

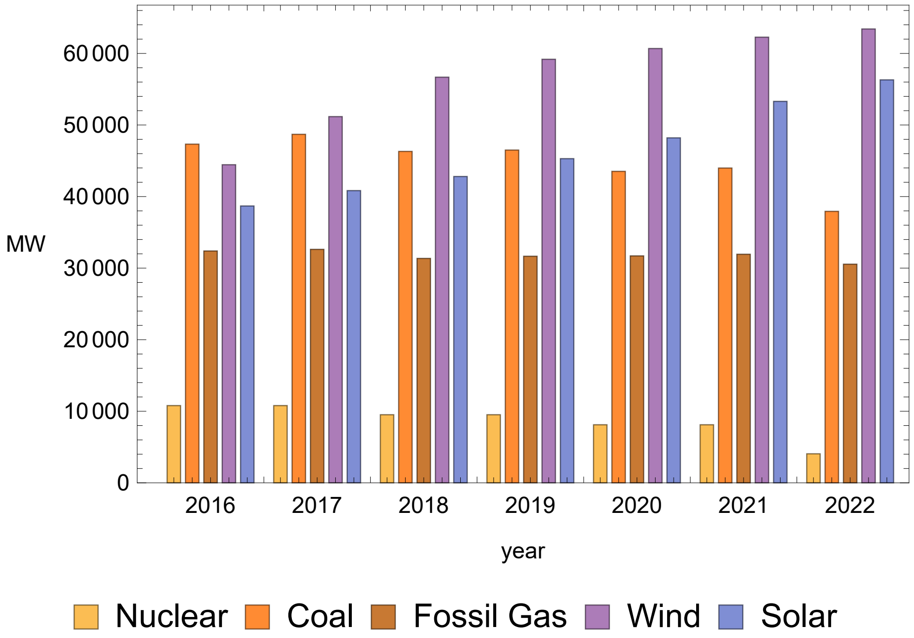

Figure 1.1: Installed capacity by energy scource in Germany. Data from [2]. Note: Oil, Hydro and smaller energy scources are excluded.

sudden power imbalance.

The increase in RES share has already impacted the stability of some grids. For instance, in 2016, part of the Australian power system experienced a blackout. The investigation showed that loss of wind generation was a major cause of the blackout [3]. Some of the wind power plants were lost due to excessive wind speed, and others were disconnected by protective devices due to voltage disturbance [3].

Furthermore, the low inertia condition had to be dealt with during demand shock in Great Britain due to COVID lockdowns. The decrease in electricity consumption produced by a response to the virus threat led to the halt of electricity production from conventional power plants [4]. Yet the RES are incentivized to produce as much as possible due to the cost of capital and zero fuel costs. Hence, the grid operator had to tackle low inertia condition in the power system by firing up auxiliary power plants [4]. This case demonstrates that the auxiliary service of providing inertia will certainly be in demand in the future.

The South Australian blackout demonstrates the challenges that come with an increased share of RES. The stability of the electric grid is vital for modern society, and even a short period of time without electricity can cause serious damage to the community and even a loss of lives. Thus, this work primarily deals with ways to integrate a larger share of RES into the electric grid without decreasing the system stability.

## 1.2 The consequences of the decrease in system inertia

The conventional power system is mostly supplied by synchronous generators. The rotor of a synchronous machine stores a lot of mechanical energy. Therefore, the generators naturally can respond to the supply-demand imbalance with their mechanical energy storage. The supply in the case of conventional power plants is defined by mechanical input from the governor. The demand part of the system comes from all the consumers of electricity, which can be industrial or regular households. The imbalance can occur on either side of the system, and inertia plays a major role in overcoming the disturbance. However, this causes frequency variation in the power system, which is undesirable. Hence, lower inertia of the system complicates frequency control and even can lead to loss of synchronism that can cause a cascading effect in the grid and further blackout.

Fig. 1.2 shows that inertia response is instant and crucial for frequency control in the first seconds after the disturbance. In conventional grids, the primary control by governors follows the initial inertia response. Both control mechanisms are crucial for the transient stability of the power system. However, they fundamentally differ, inertia response can only release/store energy in the rotating mass of a generator. On the other hand, the governor actually manipulates the mechanical power input. Thus the governor's response time to the disturbance is limited by time delays in its structure. Therefore, inertia can not be replaced by a primary response in any way. Though important, secondary and tertiary control cannot respond during fast transients.

The mathematical description of inertia response can be explained using a simple swing equation that is valid for any synchronous generator.

$$J\omega\dot{\omega} = p_m - p_l \tag{1.1}$$

where $J$ is inertia of the generator, $p_m$ is mechanical input and $p_l$ is load consumption. Thus inertia response covers the imbalance $p_m - p_l$. Also, from the equation (1.1) is clear that larger inertia suppresses frequency fluctuations in the system.

The introduction of RES decreases the overall number of conventional generators in the power system, thus reducing the total value of inertia. Moreover, fig. 1.2 shows that CIG response time to power imbalance is delayed compared to instant inertia response roughly by 100 ms [5]. There are other fundamental problems with power response by RES. First of all, the power plants are usually operated near maximum power point due to a combination of economic and

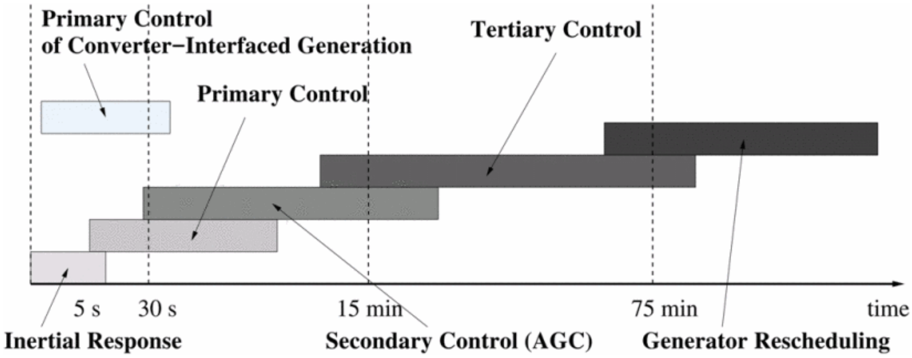

Figure 1.2: Time-inetervals of frequency control. Reprinted from [5].

technical reasons. Secondly, the energy available to CIGs instantly is stored in DC bus capacitors that are negligible compared to the inertia of a synchronous generator. Thirdly, the power production by the RES is unpredictable, hence they can be a cause of supply shortage in the system. Consequently, a normal CIG can not replace a synchronous generator in terms of inertia response and primary control. Furthermore, CIGs usually utilize a Phased Locked Loop (PLL) for synchronization with the grid. The PLL is a major cause of oscillations during the recovery after a disturbance [6].

Some grid operators identified the decrease of inertia as a major problem for the normal operation of power systems and began to set up requirements for RES power plants as early as 2003. For example, Hydro-Québec put up requirements for inertia response of wind power plants with rated power greater than 10MW [7]. The grid operator requires a plant to respond to under frequency and allow overproduction to at least 6% of rated power. This is actually only possible in the case of wind turbines since, in their rotating mass, kinetic energy is stored and can be used. The grid operator in Denmark chose a different approach. They set up requirements for wind power plants for a spinning reserve that can be used for frequency regulation [8]. The European agency ENTSO-E also tackles the issue of low inertia in the report [9]. However, they leave the development of the requirements to national grid operators. The spinning reserve is defined as a percentage of available power normally, it is 5%.

## 1.3 Overview of proposed solutions

The decrease in system inertia stimulated the debate in the professional community around the possible solution to the coming challenge. Several aspects have to be dealt with. The grid operator must ensure frequency stability while providing a dynamic response to the disturbance and securing uninterruptable supply for the customers. Furthermore, the energy sector is pressured by people and governments to increase the penetration of RES. The researchers proposed several solutions that could address the challenges of a new power system. There are several possible solutions, such as demand-side response, energy storage, synthetic inertia, and synchronous condensers [10].

- Demand-side response in itself is quite widely used in case of critical conditions in power systems. For instance, in the Czech Republic, the grid operator has the power to abruptly disconnect a consumer in case of unstable operating conditions to restore normal operation if other means are not available [11]. Other grid operators in ENTSO-E have similar competencies. However, to tackle the increased share of RES, such regulation approach has to become a service provided by electricity consumers. For example, in case of low wind speeds, an uncritical load such as a water heating load in the system can be disconnected by the operator, and the owner of the load will receive some compensation for providing such capability. However, making such control of the system flexible requires the desire and ability of electricity consumers to participate in such an arrangement. This approach is discussed in UK's national grid report [12] or in the paper [13]. Yet the report [12] highlights that the deliberate participation of industrial and public sectors is required to achieve efficacy in managing the grid in this way. That is somewhat improbable since many people are used to plug-and-play with electric devices.

- An intentional increase in inertia is also a possible solution. Moreover, it is probably the most desirable approach. Such an approach can incorporate synchronous condensers, algorithmic implementation of virtual inertia in RES power plants, or energy storage that provides inertia response. Synchronous condensers do not need any description since it is a well-known tool. Fundamentally, it is a synchronous machine that can add more rotating mass to the system. On the other hand, synthetic or virtual inertia is algorithmically implemented in CIGs. Thus, a RES power plant can emulate the behavior of a SG. Therefore, the converters with such control can be named Virtual Synchronous Generators (VSG) [14]. During a disturbance, a VSG will respond like a conventional SG thus, the system's control will not change much. However, there is a physical limitation to how much inertia a RES can provide. For instance, in the case of wind turbines, the energy necessary for inertia response can be borrowed from the rotating mass of the turbine. For the Photovoltaic power plants, the energy will come from DC bus capacitors [15]. Hence, the available energy is not comparable to SG's rotor. Nevertheless, this approach can improve the overall stability of the system. Besides, the RES plant can be equipped with an energy storage system that can increase available power.

- Energy storage systems (ESS) can utilize different means of energy storage. For instance, pumped hydro, compressed air, and flywheel use mechanical energy. Also, there are different types of storage, thermal energy storage and electrochemical (batteries and supercapacitors) [16]. Furthermore, a lot of work was put into developing efficient hydrogen storage. However, all of the ESS have some advantages and disadvantages. Thus, different ESS can be used for different regulation purposes. Pumped hydro is a well-known and well-established method of covering supply-demand imbalance throughout the day. However, building a pumped hydropower plant requires a lot of capital, and few locations are suitable for that. Electrical ESS based on supercapacitors or superconducting magnetic coils can quickly respond, but they do not store a lot of energy. Hence, they can only be used in inertia or primary response. Electrochemical ESS based on batteries can respond relatively fast and be used for energy balancing over longer periods of time. Fig. 1.3 visualizes different types of ESS and their possible application in power management.

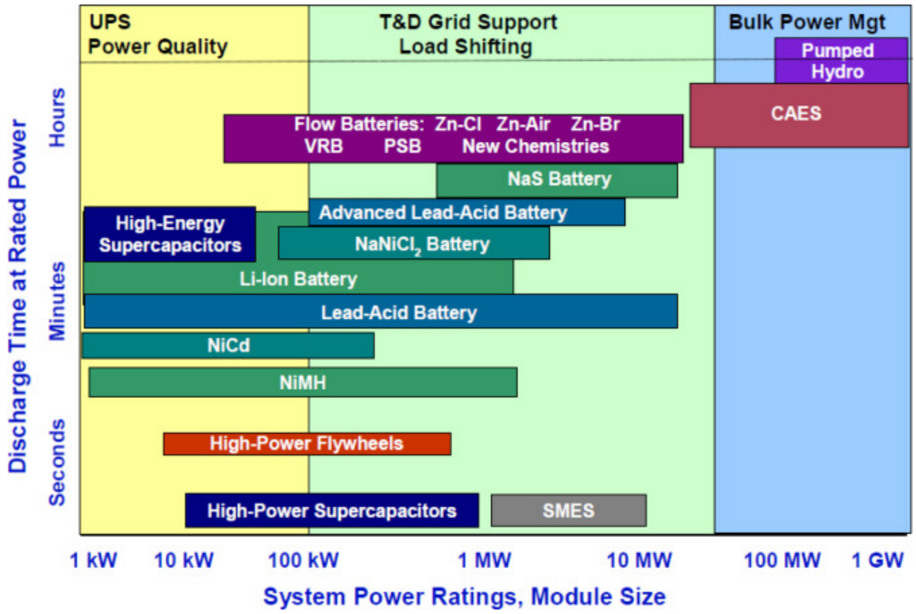

Figure 1.3: Application and rated power of different ESS types. Reprinted from [17].

Probably the single method cannot solve such a complex challenge, therefore a combination of the proposed approaches can be applied [10]. Furthermore, the Irish grid operator will ease the Rate of Change of Frequency (ROCOF) requirements [18]. That will prevent the unnecessary tripping of protective relays.

However, it could only go so far. On the contrary, the synthetic inertia of RES power plants will contribute immensely to the stability of the system [10].

## 1.4 Two fundamental approaches to virtual inertia implementation

The CIG controlling algorithm requires synchronization with the rotating $d-q$ frame of the grid. Under normal operation in steady-state, both $d-q$ frames are synchronized. There are two approaches how to synchronize a CIG with the grid, it can be either a dedicated synchronization unit or a Phased Locked Loop (PLL), or a virtual implementation of a synchronous machine, hence the synchronization is made by an active power calculation. Therefore, virtual inertia algorithms can be divided into grid-following, and grid-forming categories [5]. There are other classifications of virtual inertia topologies that will be provided later in the text, however, the author upholds the classification based on the grid synchronization technique.

### 1.4.1 Grid-following control

The grid-following control with virtual inertia is, to a degree, an extension of classical CIG control. The signal for synchronization is provided by PLL using measurement at the point of common coupling (PCC). The fundamental operating principle of the grid-following virtual inertia emulation method is to provide frequency measurement by PLL that can be used for inertia response. The inertia response can be implemented in different ways. A possible approach is to implement a power response to the change in frequency, thus the author named such algorithms Rate of Change of Frequency Virtual Synchronous Generator (RoCoF VSG) [15]. The RoCoF VSG emulates the SG behavior by responding to changes in grid frequency. The fig. 1.4 shows a principal scheme of a RoCoF VSG. The following formula can describe the power response to the change in frequency:

$$\Delta P_{VSG} = K_D \Delta\omega_{pll} + K_I \frac{\mathrm{d}\omega_{pll}}{\mathrm{d}t} \tag{1.2}$$

The RoCoF VSG can use both droop and RoCoF terms for the control. In the eq. (1.2) $K_D$ is the droop and $K_I$ is inertia constant correspondingly. Different topologies can employ the RoCoF response, but it is mostly an improvement to the vector control. Nevertheless, the frequency for the algorithm is provided by PLL, which is a major source of instability in CIGs [6].

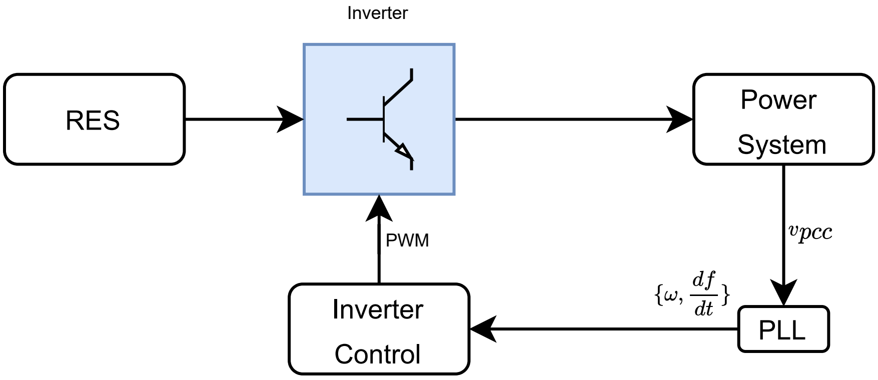

Figure 1.4: Principal scheme of RoCoF VSG.

Another approach is to emulate the mechanical part of the SG using the swing equation. In that case, the current and voltage measurements in PCC are used for computing the injected power. In the swing equation, the frequency reference from PLL is then used for improving droop control.

Fig. 1.5 shows the synchronous reference frame phase-locked loop (SRF-PLL) scheme that is widely used for synchronization with the grid. The frequency estimation uses the bus voltage in PCC as an input for the computation of grid frequency, RoCoF estimate, and grid electrical angle. Firstly by applying the Clarke transformation to the measured bus voltages, the $\alpha\beta$ coordinate voltages are obtained, then the Park Transformation gives the $d-q$ voltage vector. The $d-q$ PLL frame angle is controlled via a PI controller that forces $v_q$ to zero. Hence, this synchronization approach is dependent on the voltage signal in PCC that can be affected by the disturbance. Furthermore, the PI controller that produces the PLL angle delays the synchronization with the grid, which can cause an oscillatory response of the CIG after the fault [6].

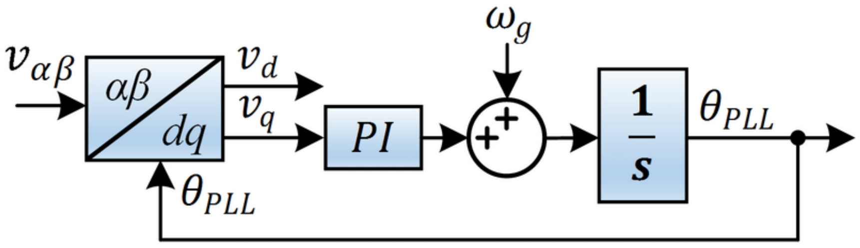

Figure 1.5: Principal scheme of SRF-PLL. Reprinted from [19].

### 1.4.2 Grid-forming control

The grid-forming type control approach does not require a dedicated synchronization unit. The synchronization is done via power balance calculation using the swing equation. Therefore, the grid-forming approach produces virtual angular velocity and virtual mechanical angle of the VSG. In the case of the grid-forming approach, under steady-state, the virtual $d - q$ frame is fully synchronized with the grid. The power injected into the grid is decided by the virtual load angle. Hence, the CIG functionally behaves like a SG. Furthermore, it can be said that the average of SGs' velocities and virtual velocities define the grid frequency. In such a case, during transient conditions, the virtual frequency is given by the power balance of power input and injected power of the CIG. That is, in principle, similar to the inertia response of the SG. The mathematical description of grid-forming control is following.

$$M\dot{\omega}_v = P_{v,m} - P_g + D(\omega_n - \omega_v) \tag{1.3}$$

$$\dot{\theta}_v = \omega_v \tag{1.4}$$

where $\omega_v$ is the virtual angular velocity, $\theta_v$ is the virtual mechanical angle, $M$ is inertia constant, $P_{v,m}$ is the virtual mechanical power input that is given by supply from the RES generator, and $P_g$ is power exchange with the grid. The droop response to the frequency $D(\omega_n - \omega_v)$ is also utilized, however can be excluded from the calculation.

The grid-forming approach does not have the main disadvantages of the PLL-based synchronization, which is dependent on a strong voltage signal in PCC. Furthermore, the grid frequency cannot be defined during the transient condition, hence the PLL-provided signal does not give the "true" grid frequency anyway. The grid-forming approach is a PD control of frequency given by a system's power balance. Therefore, it indeed emulates the SG behavior in the system. Also, the grid-forming approach can be deployed in weak grids with high penetration of RES or microgrids. It should be noted that the energy storage of CIG limits the inertia provided by the CIG, thus it cannot fully replace the conventional SG by itself.

## 1.5 A different classification of virtual inertia topologies

A different classification of virtual inertia algorithms is provided in [20]. This categorization gives the main aspect to the approach that emulates the inertia response. Thus, according to [20] there are four main categories: synchronous generator model based, swing equation base, frequency-power response based, and droop based approach.

### 1.5.1 Droop-based approach

The active power droop control is a widely known control scheme for parallel operation of converters that is inspired by a similar strategy in regulation of conventional generators [21]. Firstly, the droop control for converters was established solely on the relation between injected power and phase angle [22]. Hence, the traditional droop control can be formulated as follows:

$$\omega = \omega_{ref} - mP \tag{1.5}$$

$$m = \frac{\omega_{max} - \omega_{min}}{P_{max}} \tag{1.6}$$

However, this implementation has a fast response to the frequency deviation, which can lead to an overshoot in power response. Thus, the latter implementation of droop control included a low-pass filter to adjust the time response of the controller [22]. Fig. 1.6 demonstrates the principal control scheme of active/reactive power droop control. Hence, the mathematical description of the control scheme is as follows:

$$\omega = \omega_{set} + D_p(p_{set} - p_f) \tag{1.7}$$

where $\omega_{set}$ and $p_{set}$ are frequency and power setpoints, $D_p$ is active power droop constant and $p_f$ is filtered power measurement.

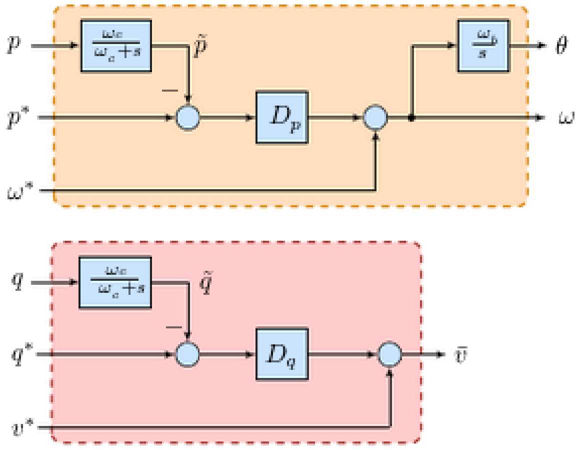

Figure 1.6: Principal scheme of active/reactive power cointrol scheme. Reprinted from [21].

The equation describing a low-pass filter with cutoff frequency $\omega_c$

$$p_f = \frac{\omega_c}{\omega_c + s} p \tag{1.8}$$

The reactive power droop control is similarly implemented in this control scheme. Hence, the voltage magnitude of the VSC is givven by following fomula:

$$v = v_{set} + D_q(q_{set} - q_f) \tag{1.9}$$

wher $v$ is voltage, $q_f$ is filtered reactive power measurement and $D_q$ reactive power droop constant.

It is fair to say that in some way, the droop control with a low pass filter adds inertia in the response of the converter [23]. There are also proposals on how to improve droop-based control by adding lead-lag compensators to the algorithm, which leads to better performance, though worse than the VSG [23].

### 1.5.2 Generator model based or Virtual Synchronous Generator

The control approach is based on emulating the behavior of a SG using a mathematical model. The author names these control methods Virtual Synchronous Generators since they indeed make an attempt to perform as a SG from the grid perspective. Different control topologies can be put into this category. Nevertheless, the two most common are synchronverter and Virtual Synchronous Machine (VISMA). The main difference between those two topologies is that VISMA goes for a more precise representation of the SG model, i.e. uses higher order mathematical model for emulation of a SG. Hence, in a way, synchronverter is a particular case of VISMA topology.

Fig. 1.7 shows a possible implementation of VISMA presented in [24]. It should be noted that this particular implementation has a PLL, nevertheless, it does not use PLL for synchronization only as an input for damping term of swing equation [24]. From fig. 1.7 is clear that VISMA uses inner current control loops, hence current spikes could be surpressed to some degree during transient which is an advantage of VISMA comparing to synchronverter. Nevertheless, such advantages come with higher computational complexity. There are some advantages to using VISMA since it employs current controllers.

The synchronverter control was firstly proposed in [25]. Fig. 1.8 shows the block diagram of the synchronverter topology. This control approach emulates SG using the second-order model of SG. The current and voltage measurements in PCC are used to calculate the virtual electrical torque, injected reactive power, and voltage reference. To calculate the virtual electric torque, the virtual mechanical angle and virtual magnetic flux ($M_f i_f$) are utilized as eq. (1.10) shows. It should be highlighted that the reactive power of the synchronverter is controlled directly without considering the excitation winding dynamics [14]. The eq. (1.12) shows how the reactive power is computed in synchronverter topology.

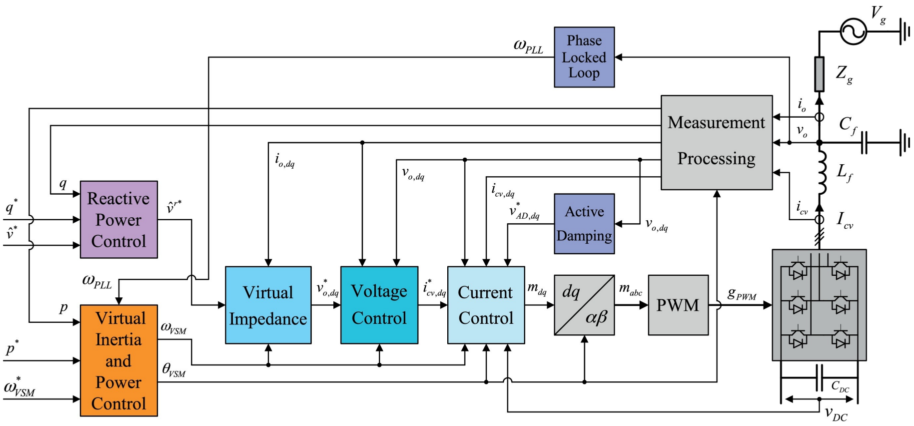

Figure 1.7: Block diagram of VISMA topology. Reprinted from [24].

Fig. 1.8 demonstrates the voltage reference produced by eq. (1.11) goes into the PWM generation unit that produces switching signals for the transistors in VSC [14, 26].

The swing equation with a droop term is used to implement the virtual mechanical part of the synchronverter. Thus, the synchronverter is categorized, according to the first presented classification, as a grid-forming device [15]. The equations describing the virtual mechanical part is similar to the (1.3) and (1.4).

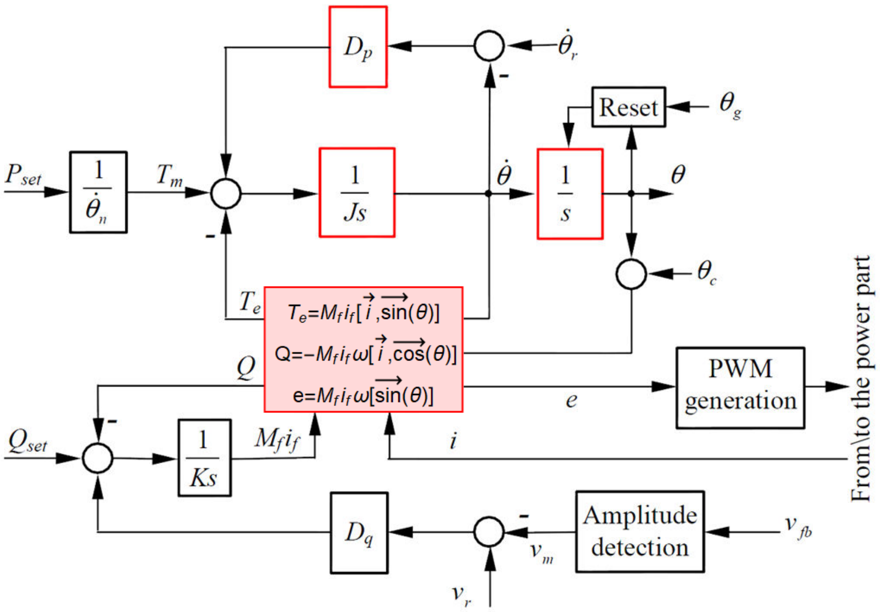

Figure 1.8: Synchronverter block diagram. Reprinted from [14].

$$T_e = M_f i_f[\overrightarrow{i}, \overrightarrow{sin}(\theta)] \tag{1.10}$$

$$e = \dot{\theta} M_f i_f \overrightarrow{sin}(\theta) \tag{1.11}$$

$$Q = -\dot{\theta} M_f i_f [\overrightarrow{i}, \overrightarrow{\cos}(\theta)] \tag{1.12}$$

where $\overrightarrow{i} = \begin{bmatrix} i_a \\ i_b \\ i_c \end{bmatrix}$ and $\overrightarrow{\sin}(\theta) = \begin{bmatrix} sin(\theta) \\ sin(\theta + \frac{2\pi}{3}) \\ sin(\theta - \frac{2\pi}{3}) \end{bmatrix}$

In the author's opinion, the two presented topologies can be called a true VSG since they provide inertia as a SG can do and do not require a dedicated synchronization unit. There are advantages and disadvantages to both implementations. The extensive studies of the discussed topologies were provided, for example, in [14,15,24,27]. The synchronverter is more intuitive in understanding and less computationally complex implementation while providing the expected benefits of the VSG.

### 1.5.3 Frequency-power based control or RoCoF VSG

The main requirement that a VSG should fulfill is to respond to frequency deviation similarly to a SG [28,29]. Hence, by releasing/absorbing energy depending on frequency fluctuation, a VSG emulates the physical inertia of a SG. The author names such frequency-power based topologies RoCoF VSG as was mentioned earlier, since they respond to the frequency change but still require a dedicated synchronization unit. Compared to droop-based control, the RoCoF VSG participates in dynamic frequency regulation [15]. The droop-based approach is similar to a proportional regulator in terms of frequency control, whereas RoCoF VSG is a proportional-derivative (PD) controller. It is closer to a SG with a turbine-governor system that is essentially a PID frequency controller in the electric grid. This approach is relatively simple and can be implemented on top of vector control [15]. Fig. 1.9 shows the block diagram of a simple RoCoF VSG. The output power increase in proportion to frequency change was formulated previously in eq. (1.2). The equation shows that RoCoF VSG can indeed be seen as a PD frequency controller from a grid perspective. The damping $K_D$, as it is called sometimes, is actually frequency droop and the derivative of frequency provided by PLL gives the inertia response. It is clear that the PLL plays a major role in frequency control in this case. The PLL is the major aspect affecting the stability and performance of this topology [6].

Various implementation of the RoCoF VSG were proposed in [30]. The main effort is focused on improving the dynamic response and stability of such control topologies. Some researchers attempted to incorporate inertia response in vector control, and some put it directly into current reference [31], others try to improve stability and add inertia control into DC bus voltage regulator. These attempts

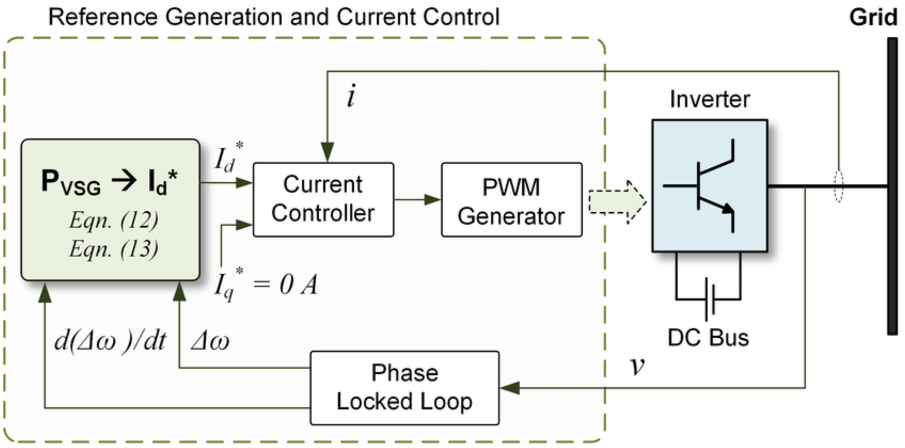

Figure 1.9: Block diagram of RoCoF VSG. Reprinted from [20].

yield quiet, stable performance that indeed provides the expected inertia response. However, any improvement cannot change the fundamental problems with PLL errors, especially under grid faults, harmonic distortions etc. [32]. Moreover, RoCoF VSG cannot work in an island mode since it is a grid-following control [20].

### 1.5.4 Swing equation based topology

This type of topology is quite similar to a particular case of VSGs, a synchronverter. However, it does not try to emulate the SG internal dynamics. The Ise lab's topology presented in [33] is a great example of a swing equation-based topology. Fig. 1.10 shows the block diagram of the Ise lab's topology. The measurements in PCC provide signals for power output of the converter ($P_{out}$) and grid frequency ($\omega_g$). These two signals then go into the swing equation, which yields virtual angular velocity ($\omega_v$) and virtual electrical angle ($\theta_v$) for the PWM generator. The swing equation takes the following form:

$$J\omega_v\dot{\omega}_v = P_{in} - P_{out} - K_D(\omega_v - \omega_g) \tag{1.13}$$

$$\dot{\theta}_v = \omega_v \tag{1.14}$$

The damping term $K_D$ is given by the difference between virtual angular velocity and grid frequency measured by PLL. The benefit of such topology is that it can be switched to grid-forming operation, and instead of damping, use the droop control [20]. The power input ($P_{in}$) into the swing equation (1.13) is decided by virtual governor. The governor model is shown in fig. 1.11, it is of the first-order with time-constant ($T_d$) and gain ($K$). This topology is a step between RoCoF VSG and VSG in some way. It does not require PLL to calculate

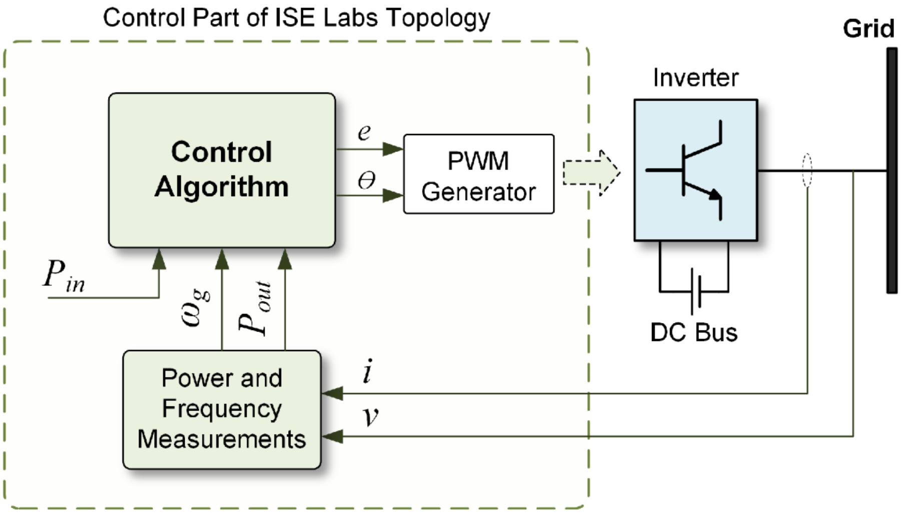

Figure 1.10: Block diagram of Ise lab topology. Reprinted from [20].

the frequency change since it is provided by the swing equation (eq. (1.13)) [20]. However, this topology does not bring the full benefits of true VSG. Hence, not many researchers are interested in developing this type of control algorithm.

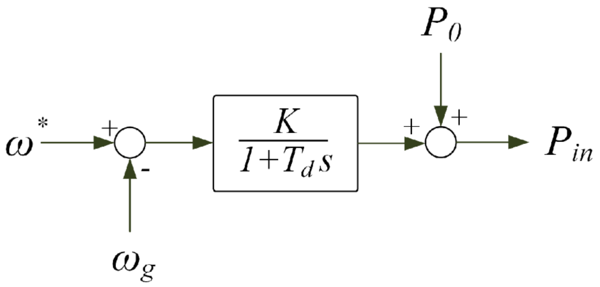

Figure 1.11: The model of the virtual governor used in Ise lab's topology. Reprinted from [20].

### 1.5.5 Comparison of topologies according to second classification

The second presented classification does not rely on the type of synchronization but rather on the structure and approach to providing inertia response. Table 1.1 outlines the major advantages and disadvantages of the presented topologies. It should be noted, that many researchers lean towards a true VSG topology since it fulfills the requirements the most. Also, it is an elegant way to increase the share of RES in the grid without completely rebuilding the power system, which is almost impossible. There were even propositions to convert to DC grids since most RES are essentially DC sources [34]. However, the capital and time required to do so make it impossible even without considering technical challenges.

Table 1.1: Comparison

| **Topology** | **Advantages** | **Disadvantages** |
|---|---|---|
| Droop-based | • Frequency derivative not neccessary<br>• PLL is used only for synchronization | • Essentially only proportional control of frequency<br>• possible overshoot in regulation that could lead to current spikes |
| RoCoF VSG | • Simple to implemented on top of vector control<br>• Includes inner current loops, hence does not produce current spikes | • Requiers PLL for synchronization<br>• Due to PLL frequency derivative can be estimated with error |
| VSG | • Emulates SG behaviour<br>• Does not require PLL<br>• Grid-forming | • Can produce current spikes |
| Swing equation based | • Uses PLL only for synchronization<br>• Simpler implementation than VSG | • It is operated as a voltage source, hence can produce current spikes |

## 1.6 Organization and contributions of the thesis

### 1.6.1 Contributions

This work presents an analysis of power system stability in the presence of grid-forming control of power converters. The research included a comparison of a power system with different control topologies for power converters. The grid-forming VSG was compared to traditional vector control and grid-following VSG using modal analysis and numerical simulations. The results provided in the text demonstrate the superiority of the grid-forming control to other topologies. The system with a true VSG has better small-signal stability characteristics and can withstand longer clearing times.

This thesis also includes an analysis of the VSG with an energy storage system. The author proposes a DC bus voltage stabilizer that enhances the stability of the system. The proposed DC bus voltage stabilizer makes VSG with ESS perform like a conventional synchronous generator.

Lastly, the author researched the possibility of grid-forming control application to STATCOMs. Thorough stability analysis of the system with VSG control of STATCOM is presented in the text. VSG topology is compared to conventional vector control using modal analysis and numerical simulations. Besides, an estimation of the region of attraction for the SMIB case is presented in the text for both examined control strategies. The comparison yielded that VSG control improves the system's stability relative to traditional control of STATCOMs.

The research conducted for the thesis was also published in journal papers. The comparison of grid-forming control to other control topologies was reported in paper [15]. Furthermore, the analysis of STATCOM with VSG control produced the paper issued in IEEE Access [14].

### 1.6.2 Organization of the thesis

The thesis is divided into six chapters, whose contents are outlined hereafter.

The first chapter is an introduction that familiarizes the reader with the problematics of modern power systems. In the chapter, the challenge of low inertia due to the replacement of conventional generators with Renewable energy sources is discussed. Furthermore, the overview of proposed solutions is presented. The chapter outlines different control topologies that can implement virtual inertia.

The second chapter defines power system stability and presents its classification. Furthermore, the mathematical tools that are helpful for power system analysis are outlined in the text.

The third chapter deals with the modeling of power sytem for stability studies. Dynamic models of essential devices in a power system are presented. Furthermore, the chapter discusses how to put together a multimachine mathematical model of a power system.

In the fourth chapter, the stability of examined control strategies is presented. The comparison includes a section on modal analysis of the system with different control topologies. Furthermore, the last section investigates the possibility of increasing virtual inertia capability using ESS. Also, in the text, a DC bus voltage stabilizer is proposed. The last section also deals with the stability analysis of the VSG with ESS.

The fifth chapter studies a STATCOM with the grid-forming control approach. The stability analysis of the SMIB system with STATCOM is presented for traditional and VSG control of STATCOM. The results were then verified in a larger IEEE 39 bus system.

In the last chapter, the research results are summarized, and the possible application of grid-forming control is reviewed. Also, the author discusses the future work.

# 2. Power System Stability

This chapter presents an overview of power system stability with classification and definitions. Also, the basic mathematical tools used for power system analysis are described. Furthermore, the challenges brought by the increased share of RES are also discussed in this section. The objective of this chapter is to immerse the reader of this work in fundamental problematics of power system stability and the effects of green transformation on it.

## 2.1 Definition of power system stability

Power system stability is a significant part of power system operation. The problematics of power system stability evolved with the development of interconnected grids. The modern power systems include a lot of different generators and loads. The correct definition of power system stability is an essential part of ensuring the normal operation of the electric grid. The definition provided in [35] by IEEE/CIGRE joint task force tries to incorporate the physical aspect and definitions given in system theory while maintaining comprehensibility for an electrical engineer.

Definition of power system stability given by IEEE/CIGRE

Power system stability is the ability of an electric power system, for a given initial operating condition, to regain a state of operating equilibrium after being subjected to a physical disturbance, with most system variables bounded so that practically the entire system remains intact [35].

This definition is indeed very broad and applies to the whole power system. It also adds that some parts of a system can be disconnected while the major part can stay intact [36]. However, in power system stability analysis, the parts of the system can be studied separately or in transition to an island mode. Furthermore, an engineer can be interested in the instability of a particular machine generator or motor that essentially does not affect the whole system but only local parameters.

According to system classification, an electric grid is a hybrid dynamical system that exhibits both continuous and discrete dynamic behavior [37]. That means that a system can change the state continuously or discretely due to control algorithms built into the system. A power system is an excellent example of a hybrid dynamical system since it is in fact, an electromechanical system.

Continuous differential equations describe the electromechanical dynamics. Most of the discrete part of the electric grids comes from switching the devices i.e., in fact, changing the configuration of the grid. Also, the CIGs can be categorized under discrete switches in the system. For the mathematical description of such a system, differential-algebraic equations are used for the modeling of the dynamics of power systems.

The power system has nonlinear, complex behavior and changes its operation parameters constantly. In a real power system, there is a connection/disconnection of loads every moment. It is a simple example of a disturbance that can produce a deviation from equilibrium, which actually changes the equilibrium point. However, in case of a small disturbance like switching of a load, the correctly tuned controller will bring the system to a new equilibrium without a problem. When a severe disturbance occurs, such as a short circuit or a loss of generation unit, the system can be divided into an isolated islands or sustain damage [35].

A power system under certain operating conditions can be stable in case of a particular disturbance and unstable in case of another. This is expected by grid operators since to make a power system stable for every possible disturbance is uneconomical and impractical [35]. Therefore, the stability analysis and studies should help to assure that the power system will remain stable under possible disturbances. The possible scenarios are extensively studied, and contingency plans are created for grid operators. Mathematical tools help to find regions of attraction that can guarantee the return to the equilibrium after the disturbance.

The definition given by the IEEE/CIGRE joint task force is very broad and abstract. However, most importantly, it sets the expectations for the power system. Hence, the conducted stability studies should reasonably assure that system will remain stable under probable disturbances. Furthermore, the power system community always attempts to find new approaches to enhance the system's performance and enlarge the stability region.

## 2.2 Classification of power system stability

The power system stability is a complex problem. Therefore to study a particular case, some simplifying assumptions have to be made to reduce complexity but not the accuracy of the result. Different assumptions are made based on what factor of instability is investigated. Hence, the main categories of stability should be discussed first. Three main factors influence the instability of the system. Firstly, the physics of the phenomenon that drives the system mode. Secondly, the size and time period of the disturbance that probably can occur. Lastly, the devices and processes that play the major role in the particular case [35]. Fig.

2.1 shows the classification of power system stability provided by IEEE/CIGRE joint task force [35].

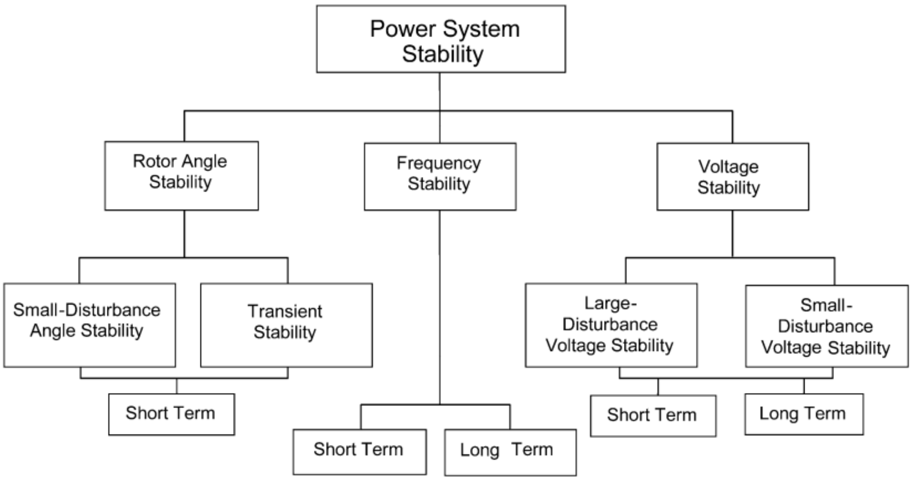

Figure 2.1: Classfication of power system stability provided by IEEE/CIGRE joint task forc. Reprinted from [35].

Fig. 2.2 demonstrates the time scales of the phenomena affecting power system operation. The conventional power system that was dominated by electric machines gave an opportunity to conduct simulations with the assumption that fundamental frequency in the grid is almost a constant value. A modeling approach based on current and voltage phasors was developed. Such approach neglects the fast switching dynamics of power converters that in most computations are represented by average models [6]. Nevertheless, the developed models are not obsolete since they allow the study of almost all of the stability categories. It only shows that researchers should be aware of the limitations of applied mathematical models.

### 2.2.1 Rotor angle stability

Definition of rotor angle stability given by Kundur

Rotor angle stability refers to the ability of synchronous machines of an interconnected power system to remain in synchronism after being subjected to a disturbance [36].

The rotor angle stability is essentially a problem of power system oscillations [35]. The rotor angle is directly affected by the difference between mechanical torque input and torque produced by electromagnetic forces. Under normal operating conditions in a steady-state, the difference is zero. Hence, the rotor angle remains unchanged. The perturbation in the power system produces a deviation in electromagnetic torque, which leads to the imbalance in torque that,

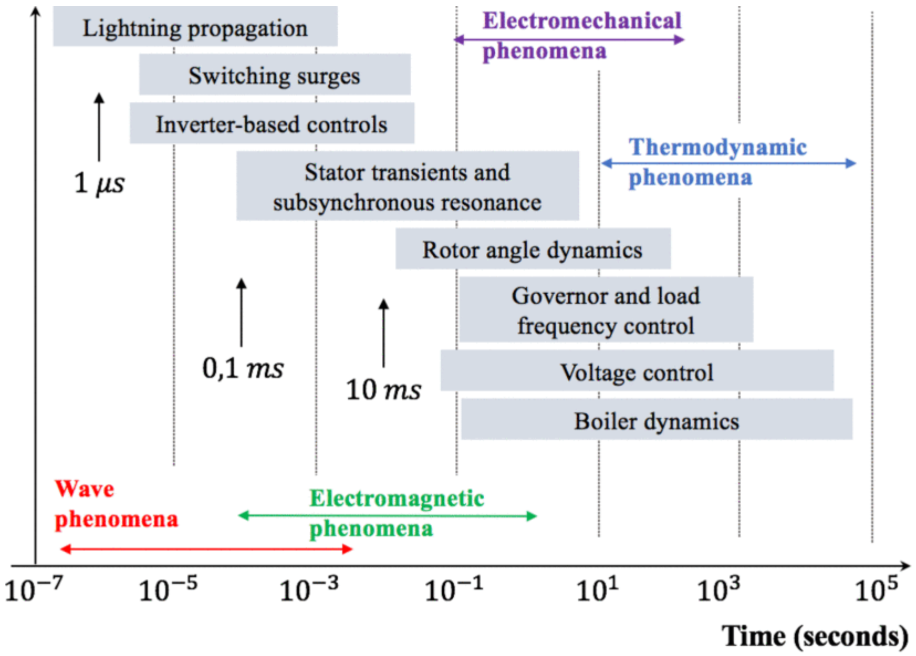

Figure 2.2: Time scales of phenomena in an electric grid. Reprinted from [6].

as a result, changes the speed of the rotor i.e. the rotor angle equilibrium is disturbed. After a disturbance, a generator's angular velocities can change relative to each other. This leads to a change in power injected into the system by each generator. The faster machine increases the power supplied into the grid, which leads to its deceleration. In a correctly designed system, the synchronism between machines will be restored naturally. However, the power transfer from the machine has a highly nonlinear dependence on the rotor angle. A generator can speed up to a certain rotor angle when the naturally occurring synchronization torques do not persist. The case when a generator or several generators do not rotate with a similar speed as others are called loss of synchronism [35]. This is an undesirable condition in the power system. After the disturbance, the electromagnetic torque changes because of two components. The difference in electromagnetic torque can be described as follows:

$$\Delta T_e = T_s \Delta\delta + T_D \Delta\omega \tag{2.1}$$

where $T_s\Delta\delta$ is the synchronizing torque that is dependent on differnce in rotor angle ($\Delta\delta$) and the synchronizing coefficient ($T_s$) of the particular device. The damping torque $T_D\Delta\omega$ is defined by the speed deviation ($\Delta\omega$) and ($T_D$) damping coefficient.

The rotor angle stability requires the participation of both components. According to [36] without sufficient synchronizing torque, the aperiodic drift of rotor angle occurs, and the damping torque prevents oscillatory instability. Fig. 2.1

shows that the rotor angles stability, depending on the nature of the phenomena driving it, is divided into two subcategories: small-disturbance (small-signal) angle stability and transient (dynamic) stability.

Small-signal stability is the ability of the system to maintain synchronism under small disturbances [36]. In a real power system, small changes in loads, generation, switching etc. take place all the time, these perturbations can be considered small disturbances. As was mentioned in the text above, power systems have nonlinear dynamics, thus, to analyze small-signal stability, the system of differential-algebraic equations is linearized. This is a tolerable assumption since the disturbances are small and state variables do not deviate far from equilibrium during an initial phase. The power system response to a disturbance is oscillatory in general [38] as shown in fig. 2.3a. If the system can properly suppress the unwanted oscillations and return to an equilibrium state, then the system is stable. Two main mechanisms participate in forcing the power system to an equilibrium: synchronization torque and damping torque. In case of insufficient synchronization torque, the rotor angle steadily increases, which leads to the loss of synchronism. Fig. 2.3b shows the general case of non-oscillatory instability. These cases appear when the generator does not have an automatic voltage regulator. Nowadays, the generators can be equipped with power system stabilizers (PSS) that change the field voltage to produce the synchronization torque. Hence, in today's power system, the most common case is oscillatory instability which arises due to the lack of damping torque. Fig. 2.3c shows the general evolution of rotor angle in time in case of oscillatory instability.

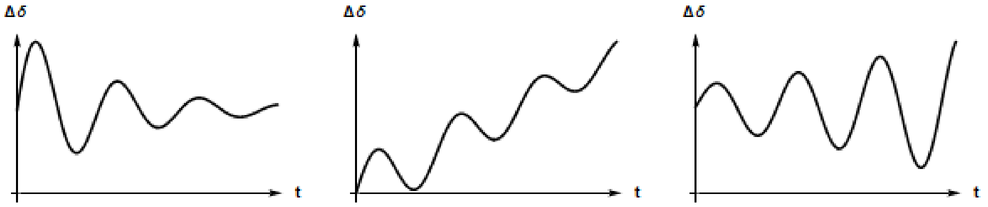

(a) Stable. (b) Non-oscillatory instability. (c) Oscillatory instability.

Figure 2.3: Response of a generator to a small-disturbance

Many oscillations are driven by synchronous generators swinging relative to each other. Hence such electromechanical oscillations usually have frequencies of 0.1 to 2 Hz [39]. Kundur in [36], divides components that drive oscillations into four categories:

- Local modes that are related to electromechanical modes of a generator that can swing relative to other machines in the system.

- Interarea modes relate to machines in one area of the power system that swings relative to the rest of the grid. This is caused by the weak coupling between areas of the power system [39].

- Control modes are associated with controllers in generating units such as excitation or speed governors.

- Torsional modes that relate to turbine-generator shaft components.

CIGRE task force on power system oscillations outlines a few important points in the paper [39]. Firstly, most oscillations are caused due to natural modes of the system components, hence hardly can be eliminated. Secondly, in most cases, the damping of those modes can be improved by correctly tuning the controllers and using PSSs for electromechanical modes.

Transient stability (dynamic stability[1]) is the ability of the system to maintain synchronism after a large disturbance [35]. Short-circuits, generation unit loss, or transmission line disconnection are examples of a large disturbance. Hence, transient stability is concerned with the studying system during a large deviation of the state from the equilibrium. The stability of the system, i.e. an ability to return to equilibrium, depends on the initial state and type of the disturbance. Furthermore, during large disturbances, the system exhibit nonlinear behavior. Also, the configuration of the grid has to be adjusted after short-circuits to disconnect the faulted line. All these factors complicate the transient stability models that should describe the dynamics of the system under large disturbances.

Nowadays, computer-aided numerical simulations are the most used tool to study the transient stability of the power system. Hence, to evaluate the dynamic stability of the system, the DAEs should be solved for the particular contingency. Then the evolution of the state variables in time can be assessed. Usually, the transient stability is concerned with 3 to 15 seconds after the disturbance occurs. Fig. 2.4 shows typical evolution of rotor angle after a large disturbance. Case 1 demonstrates a normal stable response of the system i.e. the generator will remain in synchronism. The 2. case shows the instability after the first swing of the generator. This type of rotor angle instability can be caused by insufficient synchronizing torque. Also, the larger the inertia, the lesser the deviation of the mechanical angle at the first swing. Moreover, case 3 demonstrates the instability caused by growing oscillations. Some oscillatory modes can emerge after the disconnection of the faulted component of the system [39]. Hence, the topology

---

[1] This term is mostly used in European literature and engineering practice. In this work, both terms are used interchangeably. However, in North American literature, it sometimes refers to small-signal stability with the presence of controllers [36].

of the system changed in a way that produced a new mode that is small-signal unstable.

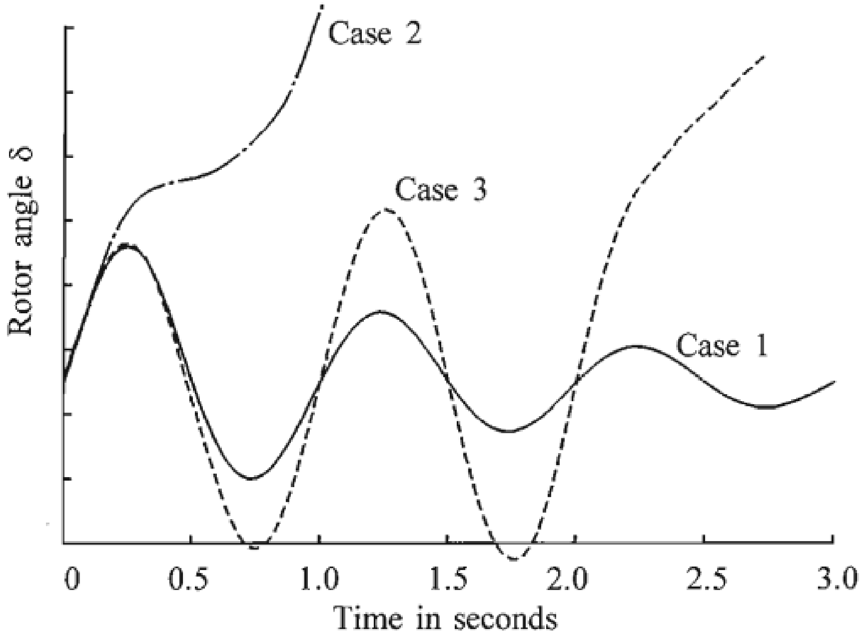

Figure 2.4: Typical responses of rotor angle after a large disturbance. Reprinted from [36].

It should be noted that transient stability studies can focus on one or group of the generators or on the whole system dynamics. In the case of a smaller part of the system, a more detailed model can be used. However, this model might not show interarea electromechanical modes that can exist. The models that describe the dynamics of the interconnected power system usually use less detailed models of the components. Nevertheless, such studies provide valuable results about the interaction of the machines in the system and potentially unstable conditions.

### 2.2.2 Voltage stability

Definition of voltage stability given by Kundur

Voltages stability is the ability of a power system to maintain steady acceptable voltages at allbusses in the system uner normal operating conditions and after being subjected to a disturbance [36].

During a disturbance, the voltage drops, which can be caused by different factors like a sudden increase in load, short-circuit fault, or loss of the reactive power-producing unit. The drop in voltage can cause an uncontrollable cascading effect. The voltage instability occurs in case of insufficient reactive power supply to maintain the required voltage level [36]. Voltage stability is a local phenomenon

[36]. Nevertheless, voltage collapse in one bus can affect the other devices and propagate through the system. Also, the voltage drop can be associated with the loss of synchronism of a generator. Usually, the main factor causing the voltage instability is loads, that in its dependent on voltage levels. Active loads such as electric motors can consume a lot of reactive power at the beginning of the operation. Hence, the limits of the voltage stability in the bus should be considered.

A simple 2-bus system case can explain the fundamental concept of voltage stability. The active power transfer from the grid node 1 to load is given by eq. (2.2) and reactive power eq. (2.2).

$$P = \frac{V_g V_l}{X} \sin\delta \tag{2.2}$$

$$Q = \frac{V_g V_l}{X} \cos\delta - \frac{V_l^2}{X} \tag{2.3}$$

Normalizing the equation with the assumption $v = V_l/V_g$, $p = PX/V_g^2$ and $q = QX/V_g^2$:

$$p = v \sin\delta \tag{2.4}$$

$$q = v \cos\delta - v^2 \tag{2.5}$$

By adding up, rearranging and squaring the normalized equations, the following relation can be obtained:

$$v^4 + v^2(2q - 1) + (p^2 + q^2) = 0 \tag{2.6}$$

By solving eq. (2.6) for the normalized voltage, the relation between voltage and power transfer can be found. Fig. 2.5 visualizes the voltage - active power curves in a simple two node system. The set of points above the gray line (locus of critical points) represents a stable operating condition.

The effects of the active loads can be studied using voltage-reactive power curves as fig. 2.6 shows. The system is stable where the $dQ_R/dV_R > 0$. The limit of stability is at the point where the derivative is zero.

In a real power system, the voltage collapse can be caused by numerous factors such as power transfer levels, controllers, faulted devices etc. [36]. The voltage stability, as well as rotor angle stability, can be divided into two major categories large-disturbance and small-signal disturbance [35].

- Small-disturbance voltage stability is the ability of the system to withstand and return to equilibrium voltage after small disturbances such as load variation. This is given by controllers, power transfer limits at the steady-state. Hence static analysis can be applied to find stability limits of the

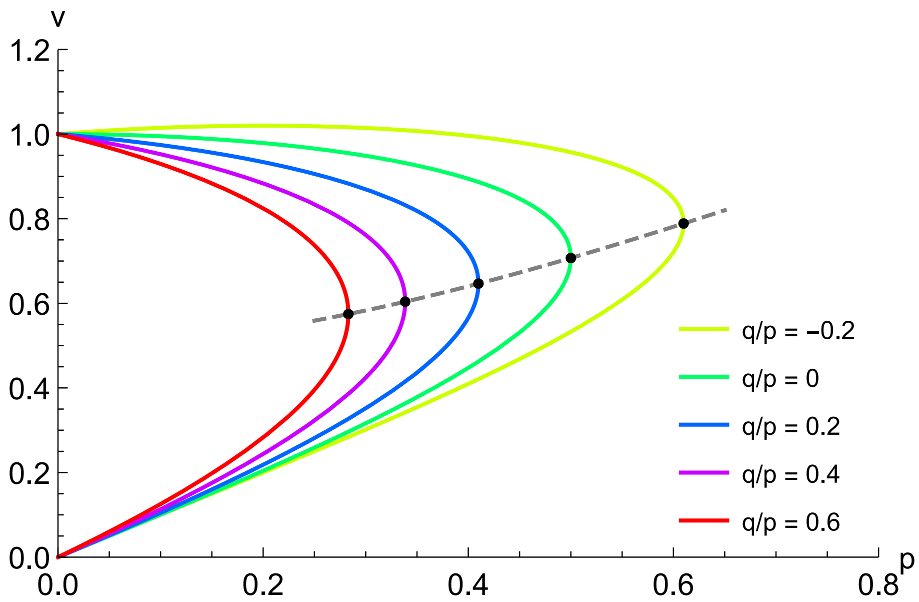

Figure 2.5: $V-P$ curves in the simple two bus system generated by solving eq. (2.6).

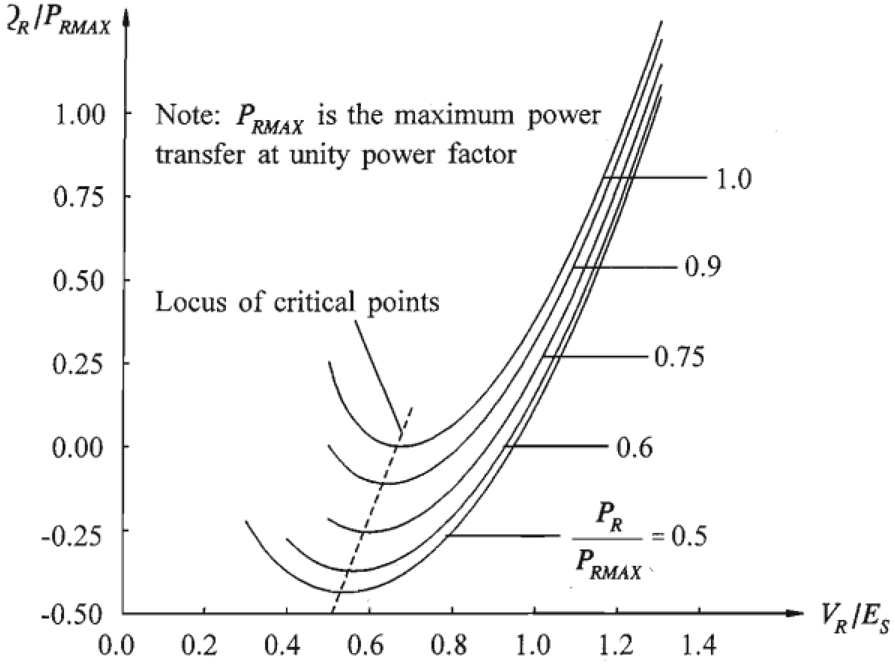

Figure 2.6: $V_R - Q_R$ relation in the simple two bus system. Reprinted from [36].

system [36].

- Large-disturbance voltage stability is an ability of the system after experiencing a large disturbance (such as short-circuit, loss of generator etc.) to return to normal operation and maintain appropriate voltage levels. Since the dynamics of the system devices and its controllers is nonlinear in its nature. Long-term simulations of contingencies varying from a few seconds up to several minutes are utilized to study the response of the system.

### 2.2.3 Frequency stability

Definition of frequency stability given by IEEE/CIGRE

Frequency stability refers to the ability of a power system to maintain steady frequency following a severe system upset resulting in a significant imbalance between generation and load [35].

The frequency in the power system is given by the angular velocity of generators, after the disturbance, the power imbalance may cause the generators to speed up or slow down. Severe faults may cause a large power imbalance in the system thus resulting in a large deviation from the nominal value. Furthermore, a protection device can trip and disconnect a part of a power system. Hence, the system will operate at least partially in an island mode.

The time scale of the frequency fluctuations varies significantly. An example of short-term frequency instability may be the following case. After a severe disturbance, a part of the system is disconnected and continues to operate in an island mode with a power imbalance that causes the frequency to drop. In case of the inadequate load shading, the following tripping of the generators causes the blackout of the island in a few seconds [35]. The long-term stability of the power system is mostly affected by the slower thermal dynamics of power plants and governors that control power input in the system. Nevertheless, load shedding plays a role in power balancing in the system if necessary to maintain the normal operation.

Generally, the frequency stability studies are a special case of transient stability where the configuration of the system may change significantly [36]. A system may be divided into islands etc. The investigated dynamics affect the complexity of the mathematical models and time steps. A model that mostly focuses on the long-term frequency dynamics does not need a precise representation of the devices in the grid. Fundamentally, it requires an accurate representation of power flow during the simulation.

## 2.3 Mathematical tools for the power system stability analysis

The previous section discussed the fundamental aspects and definitions of power system stability. This section provides an overview of basic mathematical tools used in the computation of stability of dynamic systems with application to power systems.

### 2.3.1 State-space model

The dynamics of an electromechanical system, like a power system, can be represented by a set of first-order nonlinear differential equations [36]. This representation can shortly be written in vector form as follows:

$$\dot{\mathbf{x}} = \mathbf{f}(\mathbf{x}, \mathbf{u}, t) \tag{2.7}$$

where vector $\mathbf{x}$ is the state vector that contains all state variables, vector $\mathbf{u}$ is an input vector, and the variable representing time is $t$.

The output of the system that can be observed is given by equations that depend on the state variable. The following expression puts it in mathematical form:

$$\mathbf{y} = \mathbf{g}(\mathbf{x}, \mathbf{u}, t) \tag{2.8}$$

where $\mathbf{y}$ is the vector containing the outputs and $\mathbf{g}$ is the vector of functions that link the state of the system and the output.

The state variables describe the evolution of the system in time depending on the previous state value or input into the system. The number of state variables is chosen to provide the necessary information about the dynamics of the system. In the case of the power system model, state variables can represent the physical dynamics of the devices, such as the angular velocity of a generator or a field current etc. Also, they include control variables associated with e.g., governor dynamics or turbine control.

If the derivative of state variables of the system are not directly dependent on time, then the system can be called time-invariant. Hence, the sate-representation can be written:

$$\begin{cases} \dot{\mathbf{x}} = \mathbf{f}(\mathbf{x}, \mathbf{u}) \\ \mathbf{y} = \mathbf{g}(\mathbf{x}, \mathbf{u}) \end{cases} \tag{2.9}$$

### 2.3.2 Linear state-space model and Linearization

The linear time-invariant (LTI) state-space model is a basis for many methods that are used in modeling control and analysis of power systems. The LTI state-space representation has the following form:

$$\begin{cases} \dot{\mathbf{x}} = \mathbf{A}\mathbf{x} + \mathbf{B}\mathbf{u} \\ \mathbf{y} = \mathbf{C}\mathbf{x} + \mathbf{D}\mathbf{u} \end{cases} \tag{2.10}$$

where $\dot{\mathbf{x}}$ is vector of state variables derivatives. $\mathbf{A}$ is state or system matrix, $\mathbf{B}$ is the input matrix, $\mathbf{C}$ is output matrix, $\mathbf{D}$ is feedforward matrix.

As was previously mentioned, the power system is represented by nonlinear equations. Hence, to obtain the LTI state-space model in the form like in eq. (2.10) from nonlinear state-space model (eq. (2.10)) the linearization is needed.

Linearization is an approximation of the nonlinear system of equations with the system of linear differential equations. Let us consider a single nonlinear model (2.11). Eq. (2.12) shows how the function $f(x)$ can be approximated by a Taylor series around an equilibrium point $x_e$. Neglecting quadratic and higher terms of Taylor expansion in eq. (2.12), the linear state-space representation can be obtained.

$$\dot{\mathbf{x}} = \mathbf{f}(\mathbf{x}) \tag{2.11}$$

$$f(x) \approx f(x_e) + \frac{\partial f}{\partial x}(x - x_e) + \frac{1}{2}\frac{\partial^2 f}{\partial x^2}(x - x_e)^2 + O(x^3) \tag{2.12}$$

The Taylor series expansion is performed on all functions of the nonlinear state-space model. This is easier to put into matrix form:

$$\mathbf{A} = \begin{bmatrix} \frac{\partial f_1}{\partial x_1} & \dots & \frac{\partial f_n}{\partial x_1} \\ \dots & \dots & \dots \\ \frac{\partial f_n}{\partial x_1} & \dots & \frac{\partial f_n}{\partial x_n} \end{bmatrix} \mathbf{B} = \begin{bmatrix} \frac{\partial f_1}{\partial u_1} & \dots & \frac{\partial f_n}{\partial u_1} \\ \dots & \dots & \dots \\ \frac{\partial f_n}{\partial u_1} & \dots & \frac{\partial f_n}{\partial u_n} \end{bmatrix} \tag{2.13}$$

$$\mathbf{C} = \begin{bmatrix} \frac{\partial g_1}{\partial x_1} & \dots & \frac{\partial g_n}{\partial x_1} \\ \dots & \dots & \dots \\ \frac{\partial g_n}{\partial x_1} & \dots & \frac{\partial g_n}{\partial x_n} \end{bmatrix} \mathbf{D} = \begin{bmatrix} \frac{\partial g_1}{\partial u_1} & \dots & \frac{\partial g_n}{\partial u_1} \\ \dots & \dots & \dots \\ \frac{\partial g_n}{\partial u_1} & \dots & \frac{\partial g_n}{\partial u_n} \end{bmatrix} \tag{2.14}$$

### 2.3.3 Stability of dynamic systems

Definition of stability

The point $x(0)$ is stable if for the solution $x(t)$ of the system of differential equations with inital condition $\sigma$ valid: $\forall \epsilon > 0 \ \exists \delta(\epsilon) > 0$, $||x(0) - \sigma|| < \delta \implies ||x(t, x(0)) - x(t, \sigma)|| < \epsilon \ \forall t \geq 0$ [40].

In other words, if the initial condition $\sigma$ is inside the circle with radius $\delta$ and center in $x(0)$ and the $x(t, \sigma)$ will remain in the proximity of the $x(t, x(0))$ so that the norm of the difference between two solutions will be less than $\epsilon$ [40]. Then the solution is stable in the sense of Lyapunov. Fig. 2.7 illustrates the stability in the sense of Lyapunov. A special case of Lyapunov stability is when the investigated point $x(0)$ is an equilibrium point $x_e$. Then it is fair to say that the $x_e$ is stable. Furthermore, it implies that solutions starting in the proximity of the $x_e$ will remain close to the $x_e$ forever.

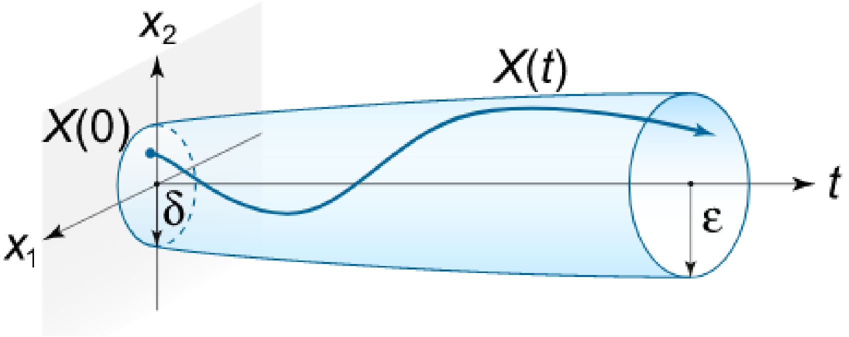

Figure 2.7: Illustation of stability in the sense of Lyapunov

Definition of asymptotic stability

The equilibrium point $x(0)$ is (locally) asymptotically stable if it fullfils conditions:

1. the point $x(0)$ is stable in the sense of Lyapunov
2. $\exists\delta(\epsilon) > 0, ||x(0) - \sigma|| < \delta \implies \lim_{t\to\infty} ||x(t, x(0)) - x(t, \sigma)|| = 0$ $\forall t \geq 0$.

The asymptotic stability means that all points in the proximity of the equilibrium point will eventually converge to the equilibrium point. Fig. 2.8 demonstrates the asymptotically stable point and the possible trajectory of the solution with the initial condition in the proximity of the $x(0)$.

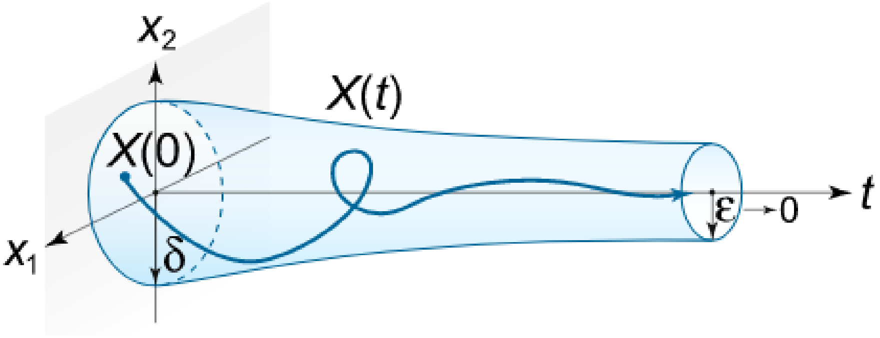

Figure 2.8: Illustation of asymptotic stability

Region of attraction

The region of attraction of equilibrium point $x_e$ is a ball with radius $\delta$: $B_r(x_e) = x \in \mathbb{R}^n : ||x - x_e|| < \delta$ It is the set of inital condtions that converge to the $x_e$

The asymptotic stability can be local and global. The difference is given by the region of attraction. Hence, the system is globally asymptotically stable if it converges to the equilibrium point for all $x(0)$.

The stability of the system can be analyzed using two Lyapunovs methods without directly solving the differential equations [36]. The first indirect Lyapunov method is based on finding eigenvalues of the system matrix. Thus, this method is only applicable to the LTI system. The analysis based on the first Lyapunov indirect method can yield three outcomes:

1. If all eigenvalues have negative real parts, then the system is asymptotically stable
2. If at least one eigenvalue has a positive real part, then the system is unstable
3. It is not possible to determine whether the system is stable or not if an eigenvalue has a zero real part.

The second Lyapunov method is based on Lyapunov functions, sometimes called energy functions. This method is applicable to a nonlinear system, assuming the system is given by equations $\dot{\mathbf{x}} = \mathbf{f}(\mathbf{x})$. Lyapunov function $V : \mathbb{R}^n \to \mathbb{R}$ should have the following properties:

1. $V(0) = 0$ if and only if $x = 0$
2. $V(x) > 0$ if $x \neq 0$
3. $\dot{V}(x) = \nabla V \cdot f(x) \leq 0$

The system is locally asymptotically stable in the neighborhood $\mathbb{B}$ if $\dot{V}(x) < 0$ $\forall x \in \mathbb{R}^n$. It should be noted that Lyapunov functions for physical systems can be related to the energy of the studied system. Hence, the derivative of the Lyapunov function indicates wether the system is dissipating energy or increasing it. The dissipation of energy thus leads to the convergence to an equilibrium point.

### 2.3.4 Modal analysis

.

Modal analysis is a typical stability study that applies Lyapunov theory to power system analysis. This is a small-signal stability analysis conducted using the system's eigenvalues. Modal analysis studies eigenvalues, eigenvector, participation factors, and mode shapes. The eigenvalues are given by the $\lambda$ values such that the following equation has a nontrivial solution [36]:

$$\mathbf{A}\mathbf{x} = \lambda\mathbf{x} \tag{2.15}$$

where $\mathbf{A}$ is the state matrix of the studied physical system. The equation can be rearranged in the form:

$$(\mathbf{A} - \mathbf{I}\lambda)\mathbf{x} = 0 \tag{2.16}$$

Hence, non-trivial solutions are given by:

$$det(\mathbf{A} - \mathbf{I}\lambda) = 0 \tag{2.17}$$

The mode given by eigenvalues $\lambda_i$ produces dynamics $e^{\lambda_i t}$. Hence, the behavior of the system is determined by the eigenvalues. If the system is stable and the eigenvalue is strictly real, then the corresponding mode is non-oscillatory [36]. The dynamics corresponding to the mode will decay faster with the increasing value of the $\lambda$. A complex eigenvalue with the negative real part produces an oscillatory mode. Complex eigenvalue always has a conjugate pair:

$$\lambda = \sigma \pm j\omega \tag{2.18}$$

The dynamics of the conjugate pair is given:

$$(a + jb)e^{(\sigma - j\omega)t} + (a - jb)e^{(\sigma + j\omega)t} \tag{2.19}$$

Using trigonometric simplifications:

$$e^{\sigma t}\sin(\omega t + \theta) \tag{2.20}$$

Thus, the amplitude of the sinusoid with frequency $\omega$ will decay exponentionally if the system is stable (i.e. $\sigma < 0$). Fig. 2.9 and fig. 2.10 show examples of trajectores for different types of eigenvalues. It should be noted that all cases in fig. 2.9 are stable in the sennce of Lyapunov. In addition, nodal sink (2.9b) and spiral sink (2.9c) types are asymptotically stable.

The real part of the eigenvalues dictates the rate of decay, and the imaginary part the frequency of oscillation. The damping of the frequency is given by the ratio:

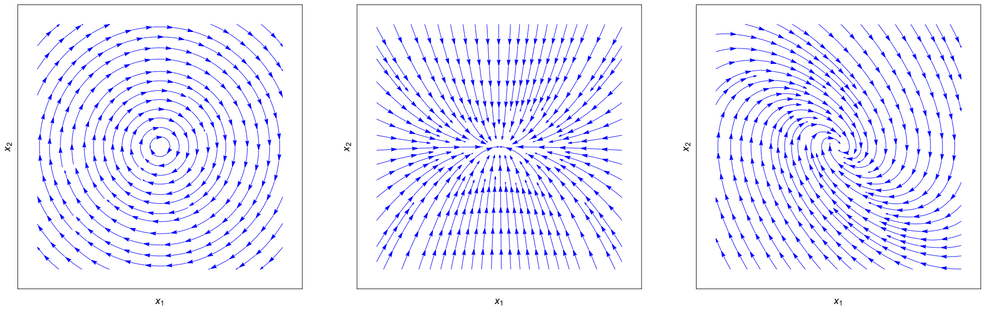

(a) Vortex. $\sigma = 0$ and $\omega > 0$ (b) Nodal sink. $\sigma < 0$ and $\omega = 0$ (c) Spiral sink. $\sigma < 0$ and $\omega > 0$

Figure 2.9: Possible combinations of stable eigenvalues.

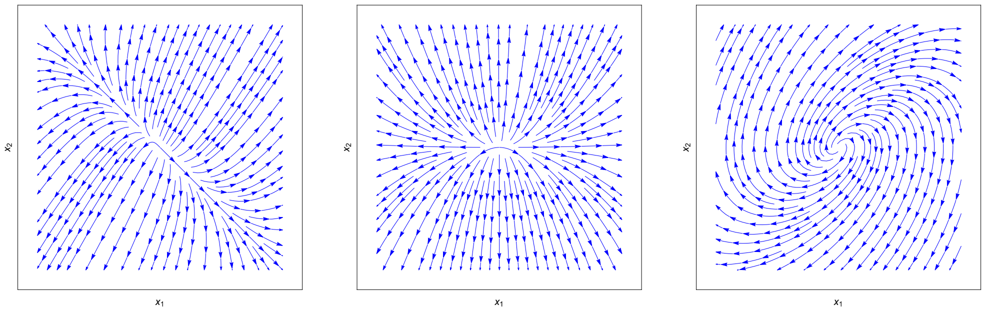

(a) Sadle. Some real parts $\sigma < 0$ and $\omega = 0$ (b) Nodal source. All real parts $\sigma > 0$ and $\omega = 0$ (c) Spiral source. $\sigma > 0$ and $\omega > 0$

Figure 2.10: Possible combinations of unstable eigenvalues.

$$\zeta = \frac{\sigma}{\sqrt{\sigma^2 + \omega^2}} \tag{2.21}$$

Participation factors are an important part of the modal analysis determining which state variable participates significantly in the mode. The results given by participation factors can be applied to improve the stability or damping of the modes. Also, it is useful for model reduction. Participation factor is a sensitivity measure of eigenvalue to a diagonal entry of the system matrix [41]. The definition of participation factor is as follows:

$$p_{k,i} = \frac{w_{k,i} h_{k,i}}{w_i^t h_{k,i}} \tag{2.22}$$

where $w_{k,i}$ and $h_{k,i}$ are $k^{th}$ elements of left $(w)$ and right $(h)$ eigenvectors associatted with $i^{th}$ eigenvalue. Eigenvectors for the $i^{th}$ eigenvalue are difned as follows:

$$\mathbf{A h_i} = \lambda_\mathrm{i} \mathbf{h_i} \tag{2.23}$$

$$\mathbf{w_i^t A} = \mathbf{w_i^t} \lambda_\mathrm{i} \tag{2.24}$$

The sum of all participation factors corresponding to the mode is equal to unity. In order to compute participation factors for complex eigenvalues eq. (2.22) is modified, thus becomes:

$$p_{k,i} = \frac{|w_{k,i}||h_{k,i}|}{\sum_{k=1}^{n} |h_{k,i}||w_{k,i}|} \tag{2.25}$$

### 2.3.5 Energy function method

The direct method of determining the stability of the system without solving the equations uses Lyapunov functions. In the previous section, the criteria for the Lyapunov function candidate were given. The Lyapunov function for power systems uses the energy definition. The fundamental concept of the energy Lyapunov energy function is visualized in fig. 2.11. In the steady-state, the ball remains in the stable equilibrium point (SEP). When the kinetic energy is transferred to the ball, it will roll. If the kinetic energy given to the ball is enough to go over the bowl's rim, then the system will go to the unstable region. Hence, the rim of the bowl represents the critical potential energy boundary (PEBS), and the surface of the bowl is the potential energy surface [36]. Therefore, the main objective of the direct Lyapunov method is to find the region where the system will be stable by computing the energy required to cross the PEBS.

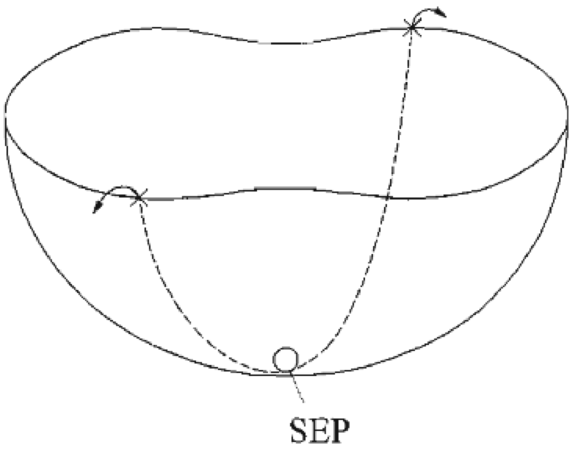

Figure 2.11: A ball rolling in the bowl. Reprinted from [36]

Similiar dynamics happen to a generator. After the fault occurs, the generator gains kinetic and potential energy during the fault-on period. After the fault is cleared, the generator returns to a new SEP since the protective relays had to disconnect the faulted part thus, the equilibrium point changes. If the fault is not cleared in time before the generator's energy surpasses PEBS, the system loses synchronism. Fig. 2.12 shows the principal dynamics of a generator during and after the fault as well as its region of attraction.

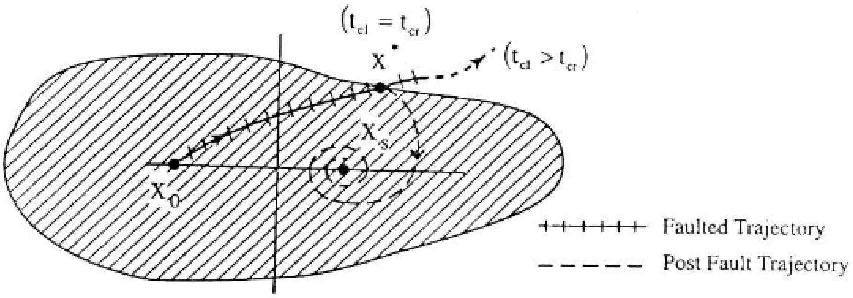

Figure 2.12: Region of atraction and generators trajectories. Reprinted from [41]

To better illustrate the Lyapunov function, let's define it for a Single Machine infinite bus case (fig.2.13 ). The energy function is as follows:

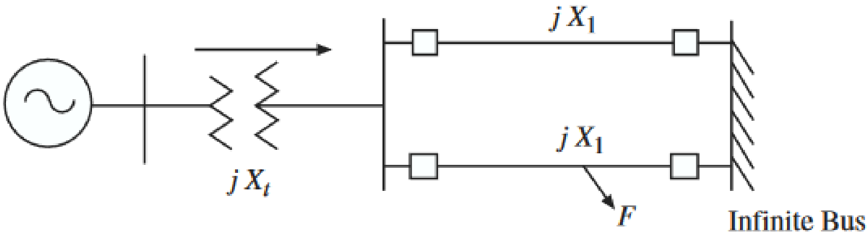

Figure 2.13: Single machine infinite bus system. Reprinted from [41]

$$V(\delta, \omega) = V_{KE}(\omega) + V_{PE}(\delta) \tag{2.26}$$

$$V_{KE}(\omega) = \frac{J\omega^2}{2} \tag{2.27}$$

$$V_{PE}(\delta) = -P_{mech}(\delta - \delta_s) - P_{el}^{max}(\cos(\delta) - \cos(\delta_s)) \tag{2.28}$$

For such stability studies, a simple second-order model of the generator is utilized. Hence, the dynamic system is described using the following equations:

$$\delta_g = \Delta\omega \tag{2.29}$$

$$J\frac{\mathrm{d}\omega}{\mathrm{d}t} = P_{mech} - P_{el} - D\Delta\omega \tag{2.30}$$

The power injected by the generator is given by:

$$P_{el} = Re(E_g e^{j\delta_g} I_g^*) \tag{2.31}$$

where the current $I_g$ is given by the connected impedance. Thus the equationas are valid for the during the fault-on and post fault system only the impedance changes.

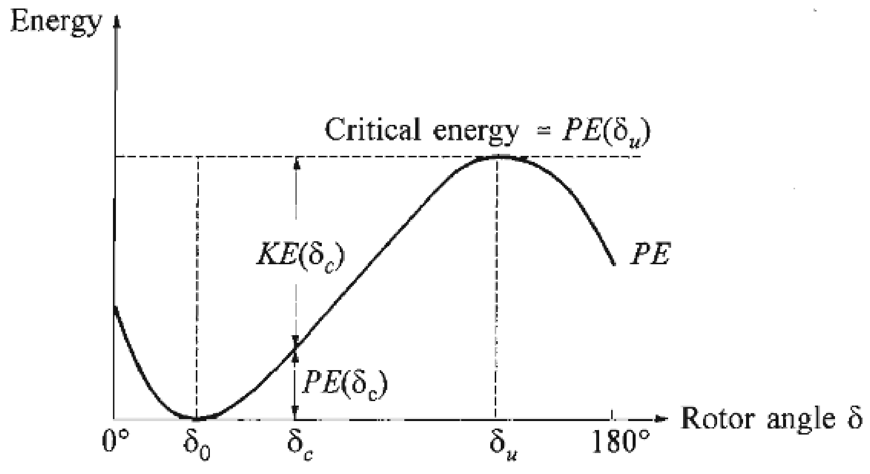

Figure 2.14: A simple visualization of energy function. Reprinted from [36]

In the fig. 2.14 the unstable rotor angle $\delta_u$ is shown. The critical energy is estimated using the $\delta_u$.

$$V_{cr} = V_{PE}(\delta_u) \tag{2.32}$$

However, the $\delta_u$ is given for a particular case of postfault system and voltage levels. This approach is extendable to the multimachine system.

# 3. Power system modeling

The previous chapter defined the state-space representation of a physical model. Besides, the state-space model's application for the system's stability studies was presented. This chapter discusses the mathematical modeling of the devices in the power system. Also, it provides simplifications and assumptions that are made in power system modeling. Furthermore, the chapter also demonstrates how the multimachine model can be put together for further analysis. Since this work is concerned with power system stability and implementation of virtual inertia to improve the said stability, the section includes the modeling of generators with some turbine-governor models and excitation control, voltage source converter model and its control and power flow equations that connect the devices into the grid.

## 3.1 Synchronous generator

The synchronous generator is a fundamental device in a power system. The modeling of synchronous machines has been developing for over 100 years. There is a lot of good literature that provides model derivation and different models (e.g. [36, 38, 41]). Therefore, this section only provides essential information for mathematical modeling of the generator. Fig.3.1 shows the complete principal diagram of the power generation unit connected to the grid. Therefore, this section describes mathematical model of generator in $d-q$ frame as well as exciters and turbine-governor models that are useful for some studies.

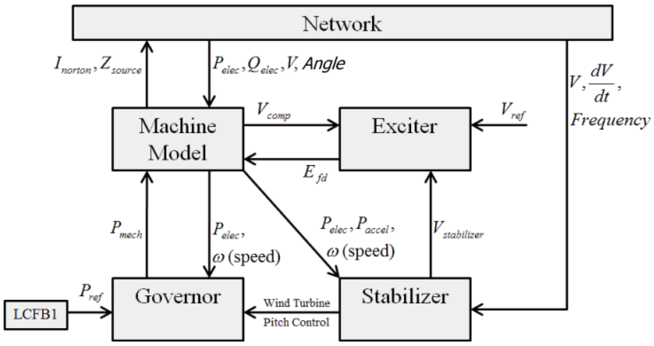

Figure 3.1: Block diagram of a power generation unit

### 3.1.1 Mathematical model of a synchrnous generator in $d-q$ frame

Let us start with a commonly accepted equivalent circuit of a synchronous machine as fig. 3.2 depicts. This particular representation assumes that the rotor is represented by three windings, one field, and one damper winding in each axis. The damper windings describe the effects of wedge chain, rotor body and amortisseures [42]. The generator model is convenient to represent in per unit (p.u.) system. Thus, the equivalent circuit reflects that the field current/voltage are transformed to the stator-based values.

As fig. 3.2 shows, the direct axis ($d-$axis) has two terminals, one is the stator terminal, and the second corresponds to the field. The simplified model of the machine can only include two windings in $d-$axis, field, and stator. Nevertheless, to represent the dynamics of a generator with higher precision, the damping winding has to be included. In the model provided here, the voltages in $d-$axis are stator- $v_d$, field - $v_f$ and damping - $v_D$. Since there is no voltage source in damping winding the $v_D = 0$. The equations describing the dynamics of the $d-$axis windings are:

$$v_d = -R_s i_d + \frac{d\psi_d}{dt} - \omega\psi_q \tag{3.1}$$

$$v_f = R_f i_f + \frac{d\psi_f}{dt} \tag{3.2}$$

$$0 = R_D i_D + \frac{d\psi_D}{dt} \tag{3.3}$$

where $\psi_d$,$\psi_f$ and $\psi_D$ are fluxes coressponding to stator, field and damping windings.

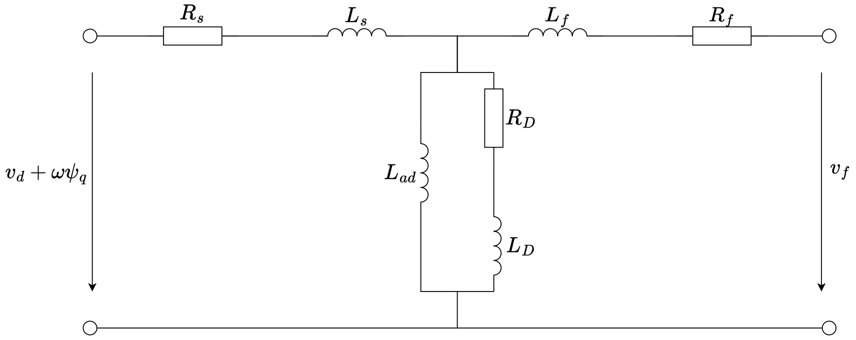

Figure 3.2: An equivalent circuit of synchronous generator's $d-$axis.

The relation between fluxes and currents can be written in matrix form:

$$\begin{bmatrix}\psi_d\\ \psi_f\\ \psi_D\end{bmatrix} = \begin{bmatrix}-L_{dd} & L_{fd} & L_{Dd}\\ -L_{dd} & L_{ff} & L_{Df}\\ -L_{dD} & L_{fD} & L_{DD}\end{bmatrix} \cdot \begin{bmatrix}i_d\\ i_f\\ i_D\end{bmatrix} \tag{3.4}$$

where the diagonal elements of the inductance matrix is:

$$L_{i,i} = L_{ad} + L_{l,i} \tag{3.5}$$

where $i$ stands for index of the winding, $L_l$ is the leakage inductance of the winding and $L_{ad}$ is mutual inductance.

It is common to accept the equal mutual inductances, thus $L_{fd} = L_{dD} = L_{fD} = L_{ad}$. However, this assumption results to some impercision in the model of a synchronous machine. Therefore, to account in the difference between the mutual inductance between rotor windings and armature winding to rotor windings, the differnetial-leakage inductance $L_{dl}$ can be introduced [42]. Hence, the $L_{fD} = L_{Df} = L_{ad} + L_{dl}$.

Fig. 3.3 shows the quadrature axis ($q-$axis) equivalent circuit of the generator. The $q-$axis has only one terminal port at the stator winding. In this particular representation, only one damping winding is present. However, the simplest model does not include damping windings at all. Mostly, the equivalent circuit has one or two windings at $q-$axis. However, most precise models can include two damper windings in $d-$axis and up to three in $q-$axis [42].

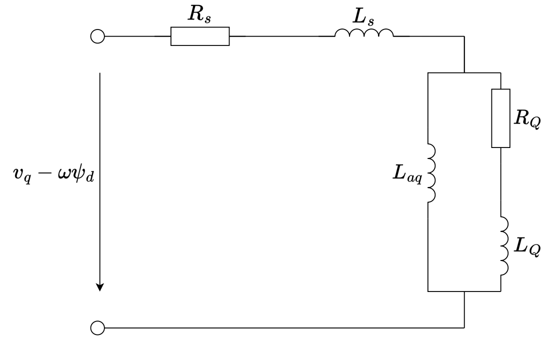

Figure 3.3: An equivalent circuit of synchronous generator's $q-$axis.

Form the fig. 3.3 is clear that the voltage of the damper winding is equal to zero. Hence, the following equations are valid for the windings of the generator in $q-$axis:

$$v_q = -R_s i_q + \frac{d\psi_q}{dt} + \omega\psi_d \tag{3.6}$$

$$0 = R_Q i_Q + \frac{d\psi_Q}{dt} \tag{3.7}$$

The relation between fluxes and current in vecotor-matrix formk is as follows:

$$\begin{bmatrix} \psi_q \\ \psi_Q \end{bmatrix} = \begin{bmatrix} -L_{qq} & L_{aq} \\ -L_{aq} & L_{QQ} \end{bmatrix} \cdot \begin{bmatrix} i_q \\ i_Q \end{bmatrix} \tag{3.8}$$

where $L_{aq}$ is mutual inductance in $q-$axis and diagonal elements of the matrix are given by the sum of leakage and mutual inductances of the corresponding winding.

The electric torque produced by the electromagnetic field of the generator in per-unit system is given by the following relation [36]:

$$T_e = \psi_d i_q - \psi_q i_d \tag{3.9}$$

The swing equation describes the mechanical dynamics of the machine

$$J\frac{\omega}{dt} = T_{mech} - T_e \tag{3.10}$$

where $T_{mech}$ is mechanical torque and $J$ is the inertia of the generator[1].

Thus, the load angle or the angle between the synchronous reference frame of the grid and of the generator is:

$$\frac{d\delta}{dt} = \omega - \omega_s \tag{3.11}$$

In industry a simplified model with neglected stator transients is oflten utilized. The two-axis model or $4^{\text{th}}$ order model assumes that generator has only one rotor winding in each axis. In $d-$axis it is field winding and one damper in $q-$axis. The derivation of the model is beyond the scope of the work, besides it is commonly known and utilized model, and its derivation can be found in Sauer's book [41]. Hence, the following equations plus the swing equation descrive the two-axis model.

Firstly, stator algebraic equations are:

$$E_q = R_s i_q + x'_d i_d + v_q \tag{3.12}$$

$$E_d = R_s i_d - x'_q i_q + v_d \tag{3.13}$$

The modified differential equations with fluxes substituted by transient voltages:

$$T_{d0}\frac{\mathrm{d}E_q}{\mathrm{d}t} = -E_q - (x_d - x'_d)i_d + E_{fd} \tag{3.14}$$

---

[1] Inertia constant: Many software tools use the inertia constant $H$ instead of inertia, which is calculated by dividing the rotational kinetic energy at rated speed by base power. Hence, in p.u. system $J = 2H$

$$T_{q0}\frac{\mathrm{d}E_d}{\mathrm{d}t} = -E_d + (x_q - x_q')i_q \tag{3.15}$$

where $E_q, E_d$ are transient voltages in $d-q$ axis, $E_{fd}$ is field voltage, $i_q, i_d$ are currents in $d-q$ axis.

The electromagnetic torque is computed as follows:

$$T_{el} = E_q i_q + E_d i_d - (x_d + x_d')i_d i_q \tag{3.16}$$

### 3.1.2 Exciter model with PSS

The excitation system is an essential part of the generator that provides current to the field winding. Furthermore, the excitation system takes part in the control of the voltage/ reactive power in PCC. Also, the excitation system can be equipped with power system stabilizers (PSS) that improve system stability. This section briefly introduces commonly used models for power system modeling and stability studies. More on the practical application of different excitation system models can be found in IEEE guideline [43].

Fig. 3.4 shows a commonly known IEEE Type I excitation system. It is widely used in power system modeling as a generic choice for the exciter. This model represents an exciter with a field control DC machine and voltage regulator.

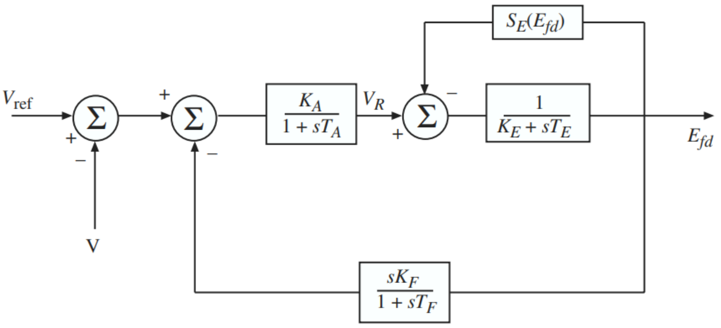

Figure 3.4: IEEE type I exciter. Reprinted from [41]

The dynamics of the excitation system is described by following equations:

$$\frac{dE_{fd}}{dt} = -\frac{K_e + S_e(E_{fd})}{T_e}E_{fd} + \frac{V_r}{T_e} \tag{3.17}$$

$$\frac{dV_r}{dt} = -\frac{V_r}{T_a} + \frac{K_a}{T_a}R_f - \frac{K_a K_f}{T_a T_f}E_{fd} + \frac{K_a}{T_a}(v_{ref} - v_{pcc}) \tag{3.18}$$

$$\frac{dR_F}{dt} = -\frac{R_f}{T_f} + \frac{K_F}{T_f^2}E_{fd} \tag{3.19}$$

the nonlinearity corresponding to the effect of exciter saturation that is hidden in the term $S_e(E_{fd})$ is usually approximated using the following relation:

$$S_e(E_{fd}) = A_e e^{B_e E_{fd}} \tag{3.20}$$

Another commonly utilized exciter model is AC4A type which is based on an alternator-suppled controlled rectifier. The block diagram of the static exciter is shown in fig. 3.5. The lead-lag block provides stabilization for the system, and the time constant $T_a$ represents the time constant corresponding to the regulator and thyristor bridge. The equations describing the dynamics are:

$$\frac{E_{fd}}{dt} = \frac{1}{T_a}(K_a x_t - E_{fd}) \tag{3.21}$$

$$\frac{dV_f}{dt} = \frac{1}{T_r}(V_t - V_f) \tag{3.22}$$

$$\frac{dx_{ll}}{dt} = V_{err} - \frac{x_{ll}}{T_b} \tag{3.23}$$

$$x_t = \frac{T_c}{T_b}V_{err} + \frac{T_b - T_c}{T_b^2}x_{ll} \tag{3.24}$$

$$V_{err} = V_{ref} - V_f + V_{pss} \tag{3.25}$$

where $x_t$ is the output of lead-lag block and $x_{ll}$ its state variable.

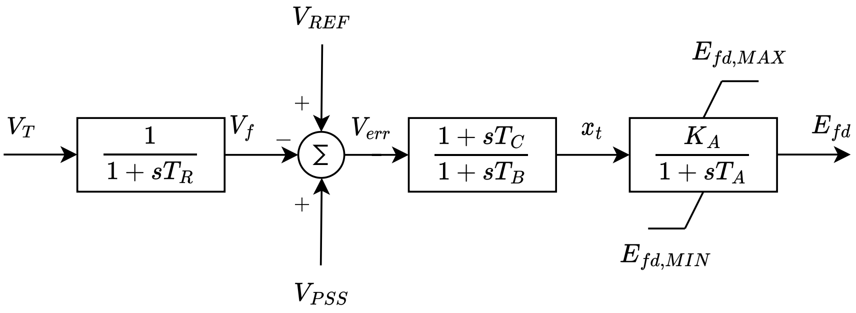

Figure 3.5: IEEE type AC4A excitation system.

### 3.1.3 Power System Stabilizers

A PSS adds a control signal to the excitation system in order to enhance the generator's damping [36]. As an input to the PSS generator's angular velocity is usually used, other inputs such as power, torque, or voltage are used less frequently. It should be noted that the PSS utilizes local measurement but nevertheless affects both local and global modes. Fig. 3.6 shows the block diagram of a simple PSS. The first block is a washout filter, which is essentially a highpass filter since the slow velocity changes are associated with overall grid dynamics. The lead-lag block provides phase compensation, so the PSS, when necessary, changes field voltage to create damping torque. The main tool for tuning and analyzing the system with PSS is modal analysis since the PSS can affect unstable modes.

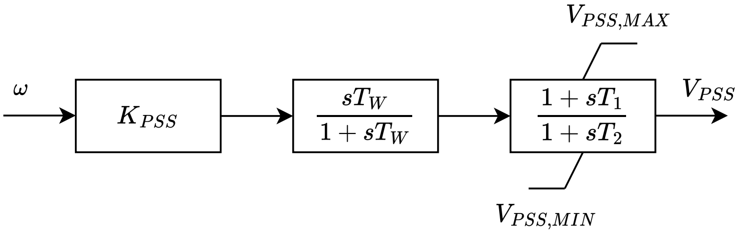

Figure 3.6: Simple PSS block diagram.

It is easier to write the linear state-space model of the simple PSS, thus:

$$\begin{bmatrix}\dot{x}_1\\ \dot{x}_2\end{bmatrix} = \begin{bmatrix}0 & 1\\ -\frac{1}{T_wT_2} & -\frac{T_w+T_2}{T_wT_2}\end{bmatrix} \cdot \begin{bmatrix}x_1\\ x_2\end{bmatrix} + \begin{bmatrix}0\\ 1\end{bmatrix} \cdot \omega \tag{3.26}$$

$$v_{pss} = K_{pss} \cdot \begin{bmatrix}-\frac{T_1}{T_wT_2^2} & \frac{1}{T_2} - \frac{T_1(T_w+T_2)}{T_wT_2^2}\end{bmatrix} \cdot \begin{bmatrix}x_1\\ x_2\end{bmatrix} + \begin{bmatrix}\frac{K_{pss}T_1}{T_2}\end{bmatrix} \cdot \omega \tag{3.27}$$

The conventional PSS is shown in fig. 3.7. It is also known as STAB1 i.e., IEEE classification. It is commonly utilized in stability studies. It is more accurate compared to the simplest configuration since most PSSes utilize at least two lead-lag blocks for phase compensations and is quite similar to IEEEST [43] besides the filter.

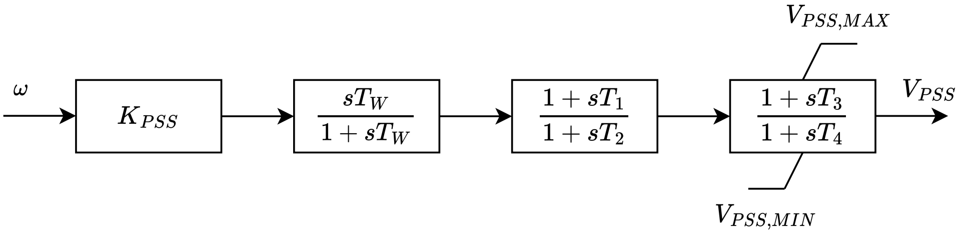

Figure 3.7: Conventional PSS block diagram.

The state-psace model of the conventional PSS is as follows:

$$\begin{bmatrix}\dot{x}_1\\ \dot{x}_2\\ \dot{x}_3\end{bmatrix} = \begin{bmatrix}0 & 1 & 0\\ 0 & 0 & 1\\ -\frac{1}{T_2T_4T_w} & -\frac{T_2+T_4+T_w}{T_2T_4T_w} & -\frac{T_2T_4+T_2T_w+T_4T_w}{T_2T_4T_w}\end{bmatrix} \cdot \begin{bmatrix}x_1\\ x_2\\ x_3\end{bmatrix} + \begin{bmatrix}0\\ 0\\ 1\end{bmatrix} \cdot \omega \tag{3.28}$$

$$v_{pss} = K_{pss} \cdot \begin{bmatrix} -\frac{T_1T_3}{T_2^2T_4^2T_w} \\ \frac{1}{T_2T_4} - \frac{T_1T_3(T_2+T_4+T_w)}{T_2^2T_4^2T_w} \\ \frac{T_1T_w+T_3T_w}{T_2T_4T_w} - \frac{T_1T_3(T_2T_4+T_2T_w+T_4T_w)}{T_2^2T_4^2T_w} \end{bmatrix}^T \cdot \begin{bmatrix} x_1 \\ x_2 \\ x_3 \end{bmatrix} + \begin{bmatrix} \frac{K_{pss}T_1T_3}{T_2T_4} \end{bmatrix} \cdot \omega \quad (3.29)$$

### 3.1.4 Governor models

The previous chapter discussed the stability of power systems. The turbine-governor drives the mechanical dynamics of the generator, thus affecting the whole system. Therefore, the stability, especially rotor angle stability and frequency stability, are affected by it. Also, in small-signal stability, the incorporation of the turbine-governor model gives a better representation of the eigenvalue placement of the system. The modeling of the turbine dynamics is a well-developed field. Many models exist that represent different types of power plants that can be driven by a steam turbine, hydro, or gas turbine. Hence, there is no need to go into the depth of the turbine modeling problematics since it is beyond the scope of the work. A curious reader may find more on the topic in references [36,44,45]. There are two commonly utilized models for steam turbines, the TGOV1 and IEEEG1 (IEEE type I). Fig. 3.8 shows the simple TGOV1 model. The model represents the governor droop $R$, the main steam control valve constant $T_1$, and the lead-lag block corresponding to the dynamics of the reheater and turbine [45].

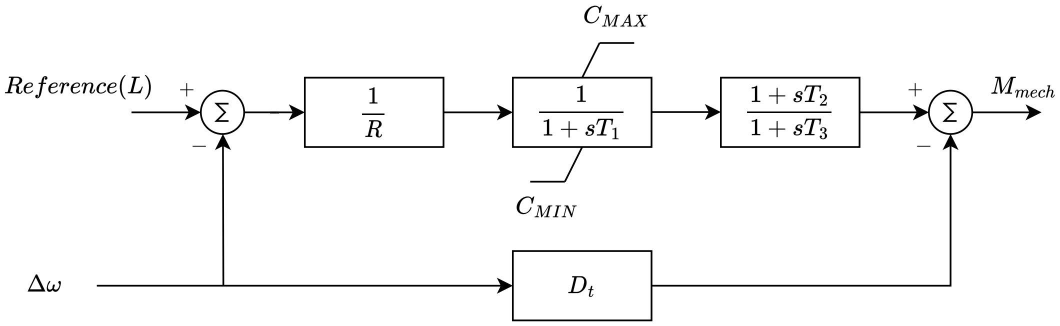

Figure 3.8: The TGOV1 steam turbine model.

It is again easier to put it into a linear state-space model with auxiliary state variables $x_1, x_2$. Thus, the mathematical model of TGOV1 is as follows:

$$\begin{bmatrix} \dot{x}_1 \\ \dot{x}_2 \end{bmatrix} = \begin{bmatrix} 0 & 1 \\ -\frac{1}{T_1T_3} & -\frac{T_1R+T_3R}{T_1T_3R} \end{bmatrix} \cdot \begin{bmatrix} x_1 \\ x_2 \end{bmatrix} + \begin{bmatrix} 0 & 0 \\ 1 & -1 \end{bmatrix} \cdot \begin{bmatrix} L \\ \Delta\omega \end{bmatrix} \quad (3.30)$$

$$M_{mech} = \begin{bmatrix} \frac{1}{T_1T_3R} & \frac{T_2}{T_1T_3R} \end{bmatrix} \cdot \begin{bmatrix} x_1 \\ x_2 \end{bmatrix} + \begin{bmatrix} 0 & -D_t \end{bmatrix} \cdot \begin{bmatrix} L \\ \Delta\omega \end{bmatrix} \quad (3.31)$$

Fig. 3.9 shows the IEEE type I steam turbine model. It can be used to model four-steam stages and cross-compound units. This turbine model is often used in simulations of interconnected grids stability [45]. The IEEEG1 is implemented in the majority of power system simulation software tools.

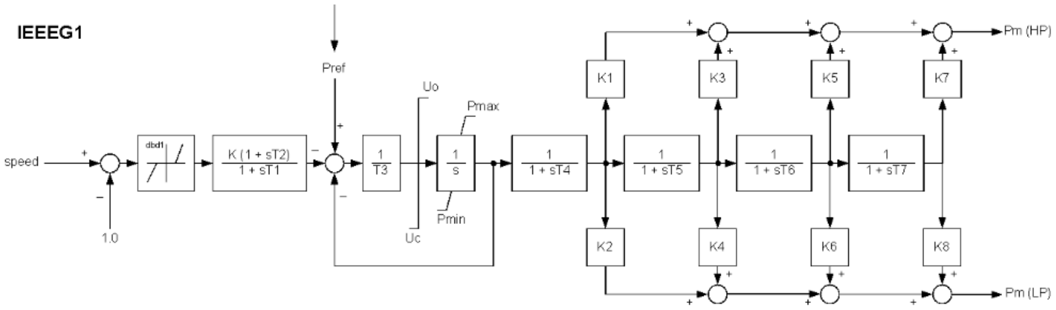

Figure 3.9: The IEEEG1 steam turbine model. Reprinted from [45]

Assuming that there are no other turbines i.e. all $K$ are equal to zero, the matrices for the state-space model of the IEEEG1 are:

$$\mathbf{A} = \begin{bmatrix} 0 & 1 & 0 & 0 & 0 & 0 & 0 & 0 \\ -\frac{1}{T_2T_3} & -\frac{T_2+T_3}{T_3T_2} & 0 & 0 & 0 & 0 & 0 & 0 \\ 0 & 0 & 0 & 1 & 0 & 0 & 0 & 0 \\ 0 & 0 & -\frac{1}{T_2T_3} & -\frac{T_2+T_3}{T_3T_2} & 0 & 0 & 0 & 0 \\ 0 & 0 & 0 & 0 & 0 & 1 & 0 & 0 \\ 0 & 0 & 0 & 0 & 0 & 0 & 1 & 0 \\ 0 & 0 & 0 & 0 & 0 & 0 & 0 & 1 \\ -\frac{1}{T_2T_3} & -\frac{T_1}{T_2T_3} & \frac{1}{T_2T_3} & \frac{1}{T_3} & -\frac{1}{T_4T_5T_6T_7} & a_{8,6} & a_{8,7} & a_{8,8} \end{bmatrix} \tag{3.32}$$

where

$$a_{8,6} = -\frac{T_4+T_5+T_6+T_7}{T_4T_5T_6T_7}$$

$$a_{8,7} = -\frac{T_6T_7+T_5\left(T_6+T_7\right)+T_4\left(T_5+T_6+T_7\right)}{T_4T_5T_6T_7}$$

$$a_{8,8} = -\frac{1}{T_5} - \frac{1}{T_6} - \frac{1}{T_7} - \frac{1}{T_4}$$

$$\mathbf{B} = \begin{bmatrix} 0 & 1 & 0 & 0 & 0 & 0 & 0 & 0 \\ 0 & 0 & 0 & 1 & 0 & 0 & 0 & 0 \end{bmatrix}^T \tag{3.33}$$

the input vector $u = \begin{bmatrix} \Delta\omega & P_{ref} \end{bmatrix}$

$$\mathbf{C} = \begin{bmatrix} 0 & 0 & 0 & 0 & \frac{1}{T_4T_5T_6T_7} & 0 & 0 & 0 \end{bmatrix} \tag{3.34}$$

$$\mathbf{D} = \begin{bmatrix} 0 & 0 \end{bmatrix} \tag{3.35}$$

## 3.2 Power electronics grid model

This section outlines the model of the Voltage Source converter. The VSCs are the most common CIG to this day, and they make up to 80% of all CIGs in the power systems [6]. Hence, in the stability studies that include RES power plants, they are used as a model for the CIGs. Furthermore, the section also provides the vector control approach that is a traditional control strategy for the VSCs. The detailed derivation of the models is not necessary since they are commonly accepted. More on the modeling of the power converters in $d-q$ frame can be found in [46–49])

### 3.2.1 Electrical part of VSC

This section state the mathematical model of the electrical part of the VSC in $d-q$ frame. Fig. 3.10 shows the schematic diagram of a VSC connected to the grid through an L-type filter. The dynamics of the VSC's filter is as follows:

$$\frac{\mathbf{m_d} v_{dc}}{2} = L_f \frac{di_d}{dt} - \omega_s L_f i_q + R_f i_d + v_d \tag{3.36}$$

$$\frac{\mathbf{m_q} v_{dc}}{2} = L_f \frac{di_q}{dt} + \omega_s L_f i_d + R_f i_q + v_q \tag{3.37}$$

where $L_f$ is filter inductance and $R_f$ is filter resistance. The modulation of power electronic signal is a vector that has two components in direct axis $\mathbf{m_d}$ and in quadrature axis it is $\mathbf{m_q}$. The control algorithm decides the control vector $\begin{bmatrix} \mathbf{m_d} & \mathbf{m_q} \end{bmatrix}$.

Since the presented average model is primarily focused on the interaction within the power system, the DC side and switching losses are neglected. Hence, the dynamics of DC bus voltage is defined as follows:

$$C_{dc} \frac{\mathrm{d}v_{dc}}{\mathrm{d}t} = \frac{p_{pv} - p_{vsc}}{v_{dc}} \tag{3.38}$$

where $C_{dc}$ is DC capacitor, $p_{pv}$ si the power output of Photovoltaic panels and $p_{vsc}$ is power exchange with the grid.

The power injected into the grid can be computed using the following formula:

$$p_{vsc} = (\mathbf{m_d} v_{dc} i_d + \mathbf{m_q} v_{dc} i_q)/2 \tag{3.39}$$

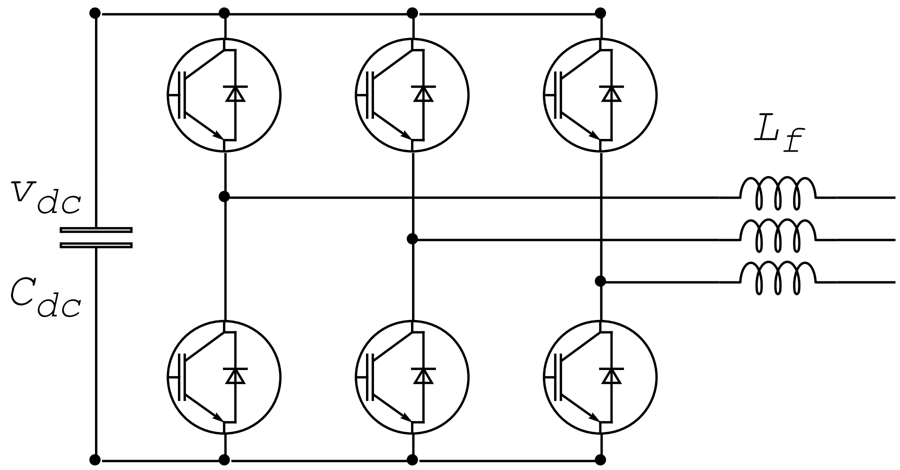

Figure 3.10: Voltage Source Converter diagram. Reprinted from [15]

### 3.2.2 Vector control of VSCs

This section fundametally is concerned with providing the description of control loops that generate swithcing signals $\mathbf{m_d}$ and $\mathbf{m_q}$ for individual switches in VSC. Vector control is the most used control strategy for the VSC. The main advantage that vector control brings is the separate regulation of the injected active and reactive power. Fig. 3.11 shows the block diagram of the vector control. Typically the vector control has an active power outer control loop and inner current controllers that prevent the current spikes. The chosen model utilizes an integral regulator for the control of voltage in PCC. The measurements in PCC are used for the inner current control loops and synchronization via PLL. Additionally, for the voltage shift compensation due to filter resistance and reactance, the feedforward shift is used for modulation [46].

Sometimes in the power system stability studies, the PLL is omitted since especially when the dynamics of large interconnected grids are studied. According to [50], the SRF-PLL model is often used. The SRF-PLL mathematical mode is as follows:

$$\frac{d\omega_{pll}}{dt} = I_{pll} + K_{p,pll}(v_q^c - v_q^{ref}) \tag{3.40}$$

$$\frac{dI_{pll}}{dt} = K_{i,pll}(v_q^c - v_q^{ref}) \tag{3.41}$$

$$\frac{d\theta_{pll}}{dt} = \omega_{pll} - \omega_s \tag{3.42}$$

where $I$ is the integrator state variable, $\omega_{pll}$ is PLL's electric angular velocity, $K_{p,pll}$ and $K_{i,pll}$ are proportional and integral constants of PLL

The DC bus voltage is controlled using PI regulator through $d-$axis current hence the control equations are the following:

$$\frac{di_{d,ref}}{dt} = K_{i,p}(p_{reg,pi} + K_{p,dc}(v_{dc} - v_{dc,ref}) - p_{vsc}) \tag{3.43}$$

$$\frac{dp_{reg,pi}}{dt} = K_{i,dc}(v_{dc} - v_{dc,ref}) \tag{3.44}$$

where $p_{reg,pi}$ is the state variable of the PI controller. Coefficients of DC bus voltage PI controller are $K_{p,dc}$ and $K_{i,dc}$.

The voltage in PCC is controled via $q-$axis current:

$$\frac{i_{q,ref}}{dt} = K_{i,v}(v_{ref} - v_{pcc}) \tag{3.45}$$

The current controllers integrators[2] are described as follows:

$$\frac{dM_d}{dt} = K_{i,i_d}(i_{d,ref} - i_d) \tag{3.46}$$

$$\frac{dM_q}{dt} = K_{i,i_q}(i_{q,ref} - i_q) \tag{3.47}$$

where $M_d$ and $M_q$ are state variables of current controllers.

Hence, the modulation signals with feedforward compenstation are:

$$\mathbf{m_d} = v_d - \omega_s L_f i_q + K_{p,i_d}(i_{d,ref} - i_d) + M_d \tag{3.48}$$

$$\mathbf{m_q} = v_q + \omega_s L_f i_q + K_{p,i_q}(i_{q,ref} - i_q) + M_q \tag{3.49}$$

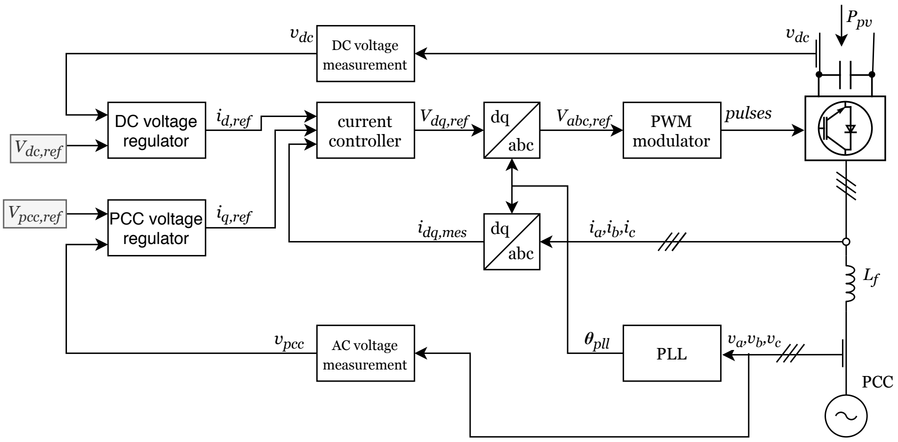

Figure 3.11: Vector control block diagram. Reprinted from [15]

---

[2] $K_{p,i_d}$ equals $K_{p,i_q}$ and $K_{i,i_d}$ equals $K_{i,i_q}$ since current controllers though decoupled use same parameters

## 3.3 Multimachine model

This section describes the steps of putting together a multimachine model with other devices. Normally, in transient stability studies, the line dynamics is neglected because the time constants of propagation in lines are much smaller than the time constants of the machine. Nevertheless, in large interconnected grids, this simplification can lead to some inaccuracies in results [36]. The network equations or sometimes power flow equations have algebraic forms. The dynamics of the devices such as generators, exciters or VSC are described using differential equations. Hence, the general form of a mathematical model of a power system is a differential-algebraic system of equations.

$$\dot{\mathbf{x}} = \mathbf{f}(\mathbf{x}, \mathbf{y}, t) \tag{3.50}$$

$$0 = \mathbf{g}(\mathbf{x}, \mathbf{y}, t) \tag{3.51}$$

where $\mathbf{x}$ is vector of state variables, $\mathbf{y}$ is vector of algebraic variables that usually correspond to voltages.

The power flow equations can be written in matrix form as follows:

$$\mathbf{Y} \cdot \mathbf{v} - \mathbf{i}(\mathbf{x}, \mathbf{v}) = 0 \tag{3.52}$$

where the $\mathbf{i}(\mathbf{x}, \mathbf{v})$ corresponds to power injection be the generating units and variable loads. Nevertheless, for stability studies is convenient to use impedance loads, which is often done [36, 41]. Therefore, the algebraic equations have the following form:

$$\mathbf{Y} \cdot \mathbf{v} = \mathbf{i}(\mathbf{x}) \tag{3.53}$$

To connect different machines, the transformation between their $d{-}q$ reference frame and grid reference form has to be done. In the authors' opinion, it is easier to implement the machine equations in their reference frame and only transform voltages and currents between reference frames. Fig.3.12 shows how the transformation between different frames can be done using Park transformation (eq. (3.54)).

$$T_{dq} = \sqrt{\frac{2}{3}} \begin{bmatrix} \cos(\theta) & \cos(\theta - \frac{2\pi}{3}) & \cos(\theta + \frac{2\pi}{3}) \\ -\sin(\theta) & -\sin(\theta - \frac{2\pi}{3}) & -\sin(\theta + \frac{2\pi}{3}) \\ \frac{1}{2} & \frac{1}{2} & \frac{1}{2} \end{bmatrix} \tag{3.54}$$

Let us show how the transformation between two $d - q$ reference frames can

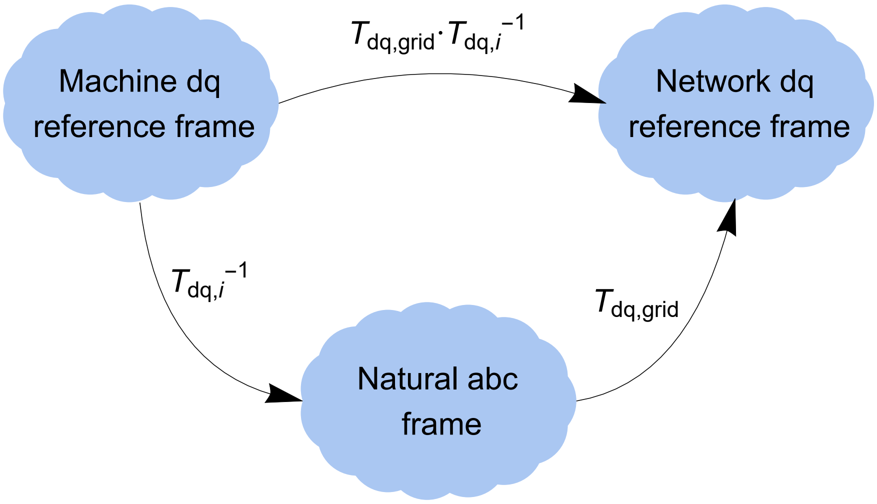

Figure 3.12: Transformation between refernce frames. Reprinted from [15]

be done. The generator velocity is $\omega_g$, and the grid synchronous angular velocity is $\omega_s$. In power system simulations, the synchronous grid velocity can be chosen to be the angular velocity of a generator or the center of inertia [36, 41]. The machine's electrical angle can be calculated:

$$\theta_g = \int \omega_g dt \tag{3.55}$$

Alternatively, it can be substituted considering that between reference frames, there is load angle $\delta$:

$$\theta_g = \omega_s t + \delta \tag{3.56}$$

As fig. 3.12 shows, the inverse Park transformation with machine electrical angle $\theta_g$ is applied to transform the variables from the generator reference frame. Afterward, the variables from the natural *abc* frame are transformed to the synchronous $d-q$ grid frame using the electrical grid angle.

The transformation can be written in matrix form as follows:

$$\mathbf{f}^{grid} = T_{dq}(\theta_s) \cdot T_{dq}^{-1}(\theta_g)\mathbf{f}^{gen} \tag{3.57}$$

where $\mathbf{f}$ can be a vector of either currents or voltages.

Simplifying the transformation matrix:

$$\begin{bmatrix} f_d^{grid} \\ f_q^{grid} \end{bmatrix} = \begin{bmatrix} \sin(\delta) & \cos(\delta) \\ -\cos(\delta) & \sin(\delta) \end{bmatrix} \cdot \begin{bmatrix} f_d^{gen} \\ f_q^{gen} \end{bmatrix} \tag{3.58}$$

# 4. VSG application

This chapter discusses the mathematical modeling of chosen virtual synchronous generator algorithms in $d-q$ frame. Furthermore, the comparison of grid-following and grid-forming types of VSG is presented. The stability analysis of both control strategies is conducted. Also, the effects of placement of converter with virtual inertia are investigated. The results of the stability analysis yielded that the grid-forming converter has better performance. Therefore, the last section describes the model of the VSG with Energy Storage System (ESS) that enables an increase in virtual inertia capability. Moreover, the author proposes an improvement for VSG DC bus voltage regulation in the presence of ESS.

## 4.1 Modeling of VSG in $d-q$ frame

The modeling of VSG has essentially two parts. The first part models the electrical elements of the VSC provided in section 3.2.1, and the second part describes the control system that generates switching signals for the VSC. Hence, this section provides the mathematical model of grid-forming and grid-following types of VSG. The synchronverter control was chosen to represent the grid-forming VSG and RoCoF VSG (presented in [30]) control topology grid-following.

### 4.1.1 Mathematical model of a grid-forming VSG: synchronverter

Fig. 4.1 shows the block diagram of the VSC connected to the grid through an L-type filter with synchronverter control. It should be noted that the model used in this work respects the dynamics of DC bus capacitor, which many research papers do not. This subsection states the mathematical model of the grid-forming VSG (synchronerter) in $d-q$ frame.

The synchronverter mimics synchronous generator behavior, which was the original inspiration behind the topology [25]. Hence, the mathematical model is similar to the model of the generator in $d-q$ frame [15]. The assumption is that the VSG, in the case of the synchronverter, has only three virtual windings. Two are stator windings in each axis, and one is rotor winding, producing the field flux. Hence, the following equations describe the three winding model:

$$v_d = R_d i_d + \frac{\mathrm{d}\psi_d}{\mathrm{dt}} - \omega\psi_q \tag{4.1}$$

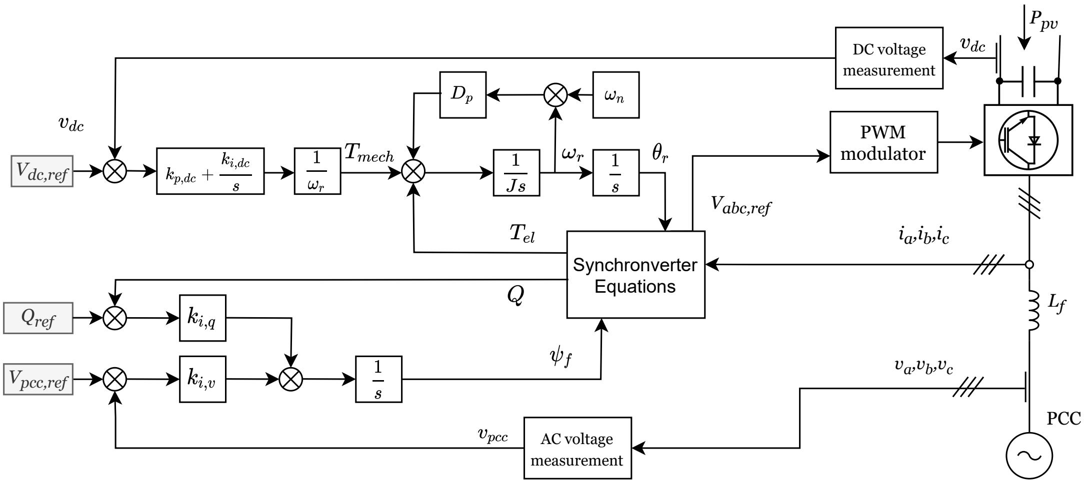

Figure 4.1: The detailed block diagram of synchronverter. Reprinted from [15]

$$v_q = R_q i_q + \frac{\mathrm{d}\psi_q}{\mathrm{dt}} + \omega\psi_d \tag{4.2}$$

$$v_f = R_f i_f + \frac{\mathrm{d}\psi_f}{\mathrm{dt}} \tag{4.3}$$

The relation between fluxes and currents is easier to put in the vector-matrix form:

$$\begin{bmatrix} \psi_d \\ \psi_q \\ \psi_f \end{bmatrix} = \begin{bmatrix} -L_{dd} & 0 & L_{fd} \\ 0 & -L_{qq} & 0 \\ -L_{df} & 0 & L_{ff} \end{bmatrix} \cdot \begin{bmatrix} i_d \\ i_q \\ i_f \end{bmatrix} \tag{4.4}$$

where $L_{fd}$ si magnetic coupling between the field winding and stator. In the synchronverter, on the contrary to the real machine, there is only one-way coupling, thus, $L_{df}$. Furthermore, the inductance of $d-$axis of the stator winding is actually the filter inductance which in a real machine is leakage inductance, hence $L_{dd} = L_f$. Furthermore, the dynamics of the field winding is neglected, therefore the derivative of the filed current is 0. Assuming that resistance in direct and quadrature axes are similar and in synchronverter is represented by the filter resistance: $R_d = R_q = R_f$. The equations (4.1)-(4.3) may be simplified further:

$$v_d = -R_f i_d + \omega_r L_f i_q - L_f \frac{di_d}{dt} \tag{4.5}$$

$$v_q = -R_f i_q - \omega_r L_f i_d - L_f \frac{di_q}{dt} + \omega_r \psi_f \tag{4.6}$$

Clearly (4.5) and (4.6) resemble the equations of the VSC electrical part provided in section 3.2.1 [15]. Thus modulations signals become $\mathbf{m_d} = 0$ and

$$\mathbf{m_q} = \omega_r \psi_f \tag{4.7}$$

The mechanical part of the VSG is emulated using the swing equation:

$$J\frac{\mathrm{d}\omega_r}{\mathrm{d}t} = \frac{p_{mech}}{\omega_r} - \frac{p_{synch}}{\omega_r} - D_p(\omega_r - \omega_n) \tag{4.8}$$

where power injected by synchronverter $p_{synch}$ in a VSG $d-q$ frame is calculated considering assumptions (3.39) and (4.7). Thus,

$$p_{synch} = \frac{\omega_r \psi_f v_{dc}}{2} i_q^r \tag{4.9}$$

The DC bus voltage is controlled through the virtual mechanical power input $p_{mech}$ [15]. Hence, the controller dynamics is:

$$p_{mech} = K_{p,p}(v_{dc} - v_{dc,ref}) + p_{reg,pi} \tag{4.10}$$

$$\frac{\mathrm{d}p_{reg,pi}}{\mathrm{d}t} = K_{i,p}(v_{dc} - v_{dc,ref}) \tag{4.11}$$

where $K_{p,p}$ and $K_{i,p}$ that are proportional and integral constants respectively

The angle between synchronverter refernce frame and synchronous refrence frame is computed as follows:

$$\frac{\mathrm{d}\delta}{\mathrm{d}t} = \omega_r - \omega_s \tag{4.12}$$

The control of the voltage or reactive power in PCC is done via field flux [15, 51]. As figure 1.8 shows the droop control can be utilized. Assuming that the synchronverter is set to be P-V node then $K_{i,q} = 0$

$$\frac{\mathrm{d}\psi}{\mathrm{d}t} = K_{i,v}(v_{ref} - v_{pcc}) + K_{i,q}(q_{ref} - q) \tag{4.13}$$

where $v_{pcc}$ is the voltage amplitude in PCC and $K_{i,v}$ is integral constant of voltage regulator.

### 4.1.2 Mathematical model of a grid-following VSG: RoCoF VSG

This section outlines the model of a RoCoF VSG that was presented in [30]. Fig. 4.2 shows the block diagram of the analysed RoCoF VSG. This particular topology is built on top of vector control which is not uncommon, as was discussed in the first chapter. Fundamentally, it is not necessary to restate the whole model of vector control, only to add a control signal that introduces the virtual inertia response. It should be noted that in fig. 4.2 the control block that emulates inertia response are highlighted in red.

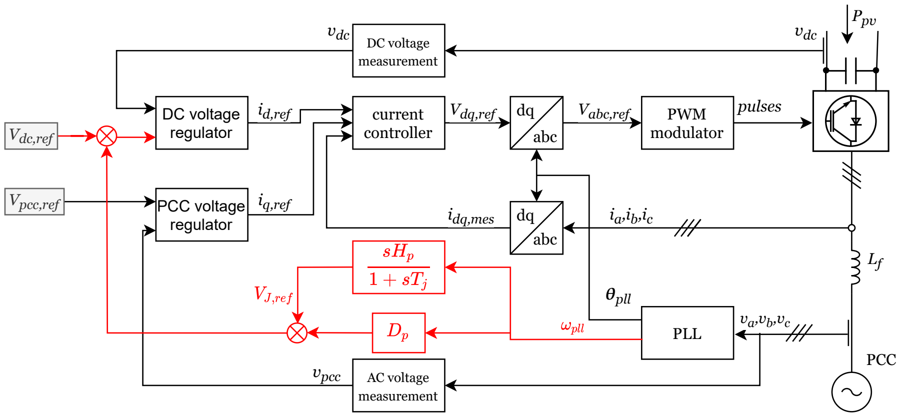

Figure 4.2: The detailed block diagram of RoCoF VSG. Reprinted from [15]

The RoCoF VSG by measuring the frequency changes the DC bus voltage reference. The PLL measures the frequency, hence the stability of the system is affected by its constants. The SRF-PLL model was stated in section 3.2.2. Consequently, as fig. 1.9 demonstrates that DC bus voltage reference consists of two signals the actual reference and the virtual inertia control signal. Therefore, the DC bus voltage reference is given by the following relation:

$$v_{dc,ref} = v_{dc,nominal} + V_{J,ref} + D_p(\omega_{pll} - \omega_n) \tag{4.14}$$

where $D_p$ is damping constant $\omega_{pll}$ is the angular velocity measured by PLL, $\omega_n$ nominal angular velocity of the power system and $V_{J,ref}$ is the control signal that emulates inertia.

The signal that emulates inertia response is described by a differential equation:

$$\frac{dV_{J,ref}}{dt} = (H_p \frac{d\omega_{pll}}{dt} - V_{J,ref})/T_j \tag{4.15}$$

where $H_p$ is virtual inertia constant and $T_j$ is time delay that simulates the gradual power reslease from the kinetic energy stored of the rotor.

## 4.2 A comparison of different control topologies

This section analyzes the stability of the grid-forming VSG and compares it to the grid-following RoCoF VSG and traditional vector control. Firstly, the modal analysis of a common IEEE 9 bus test system with VSC with different control strategies was conducted. Afterward, the transient stability study was done. And the last subsection investigates the effects of placement of virtual inertia in a power system using a larger benchmark system.

### 4.2.1 Modal analysis

This section provides the results of the modal analysis of the IEEE 9 bus system with a VSC connected to the 6th node. The IEEE 9 bus benchmark system was chosen because it is well known and common for research purposes. Furthermore, it is relatively simple, and the results can be easily interpreted. The electric parameters of elements and controller constants can be foound in the Sauer's book [41]. Fig. 4.3 shows the line diagram of the IEEE 9 bus sytem. The VSC in the analyzed model is controlled as a synchronverter, RoCoF VSG or using vector control (parameters are provided in paper [15]).

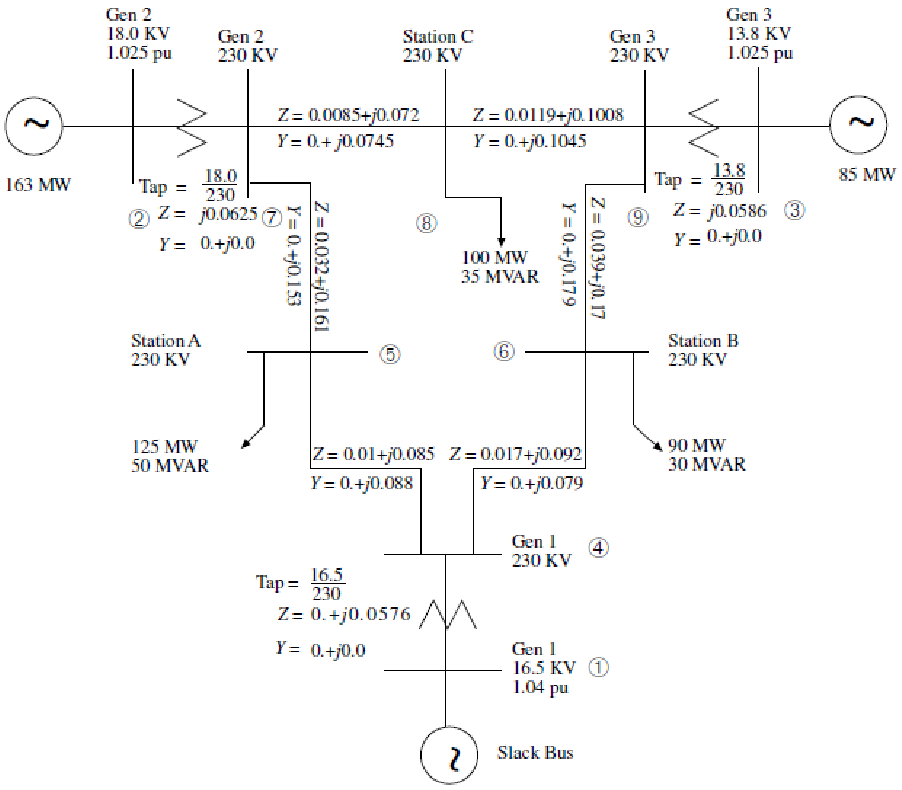

Figure 4.3: The line diagram of the IEEE 9 bus benchmark system. Reprinted from [41].

The first step for the analysis of the system stability is the construction of the mathematical model of the analyzed grid. The generator two-axis model was used with IEEE type 1 exciters and TGOV1 turbine-governor model, all were provided in the chapter on the modeling of power systems. The model of the electrical part is described in section 3.2.1. The implementation of analyzed control topologies is provided at the chapter's beginning. To perform modal analysis, the system matrix has to be obtained as explained in the section 2.3.4. After the linearization, the linear state-space model of the power system has the following form:

$$\mathbf{\Delta\dot{x}} = \mathbf{A} \cdot \mathbf{\Delta x} + \mathbf{B} \cdot \mathbf{\Delta v} \tag{4.16}$$

where $\mathbf{\Delta x}$ is the state vector $\mathbf{A}$ is the system matrix corresponding to devices constants and $B$ is the input matrix that correlates with node voltages. The power flow in the grid can be computerd as follows:

$$\mathbf{\Delta i} = \mathbf{Y_N} \cdot \mathbf{\Delta v} \tag{4.17}$$

where $\mathbf{Y_N}$ network admittance matrix and $\mathbf{\Delta i}$ is the vector of currents.

The currents injected by the devices can be calculated as follows:

$$\mathbf{\Delta i} = \mathbf{C_D} \cdot \mathbf{\Delta x} + \mathbf{D_D} \cdot \mathbf{\Delta v} \tag{4.18}$$

where $\mathbf{C_D}$ and $\mathbf{D_D}$ is matrix corresponding to individual devices.

The right hand sides of the previous two equations has to be equal:

$$\mathbf{Y_N} \cdot \mathbf{\Delta v} = \mathbf{C_D} \cdot \mathbf{\Delta x} + \mathbf{D_D} \cdot \mathbf{\Delta v} \tag{4.19}$$

Solving the equation for the voltages:

$$\mathbf{\Delta v} = (\mathbf{Y_N} - \mathbf{D_D})^{\mathbf{-1}}\mathbf{C_D} \cdot \mathbf{\Delta x} \tag{4.20}$$

Then, the algebraic equations can be eliminated by substituted the vector of voltages:

$$\mathbf{\Delta\dot{x}} = \mathbf{A} \cdot \mathbf{\Delta x} + \mathbf{B}(\mathbf{Y_N} - \mathbf{D_D})^{\mathbf{-1}}\mathbf{C_D} \cdot \mathbf{\Delta x} \tag{4.21}$$

Consequently, $\mathbf{A_{sys}} = \mathbf{A} + \mathbf{B}(\mathbf{Y_N} - \mathbf{D_D})^{\mathbf{-1}}\mathbf{C_D}$ is new system matrix with reduced algebraic equation. Thus, the small-signal stability can be analyzed by finding the eigenvalues of $\mathbf{A_{sys}}$.

The computed eigenvalues of the system with different control strategies are provided in the tab. 4.1- 4.3. Furthermore, the participation factor matrices are shown in fig. 4.5 - 4.7. Only the states with participation factors greater than 0.2 are shown in the table. In the tables, the modes with the smallest damping are highlighted. Fig. 4.4 visualizes the results for different control strategies. The dashed lines correspond to the lowest-mode damping of the system with different control topologies. The smallest mode damping of the system with vector control is $\xi_{min} = 0.0062$. From fig. 4.4 is clear that the application of RoCoF VSG improves overall damping of the system and moves some of the modes to the left. The lowest-mode damping of the system with RoCoF VSG is $\xi_{min} = 0.0112$. The system with synchronverter has better lowset damping $\xi_{min} = 0.0298$. Besides, 4.4 shows that most of the modes are shifted to the left compared to the system's similar modes with other control topologies. It should be noted that $\max(Re(\lambda))$ is much greater than for other cases. As was explained in the section 2.3.4 the larger the real part of the mode, the faster the exponent decays. Therefore, the system should converge faster when the modes are shifted to the left from the $y$ axis.

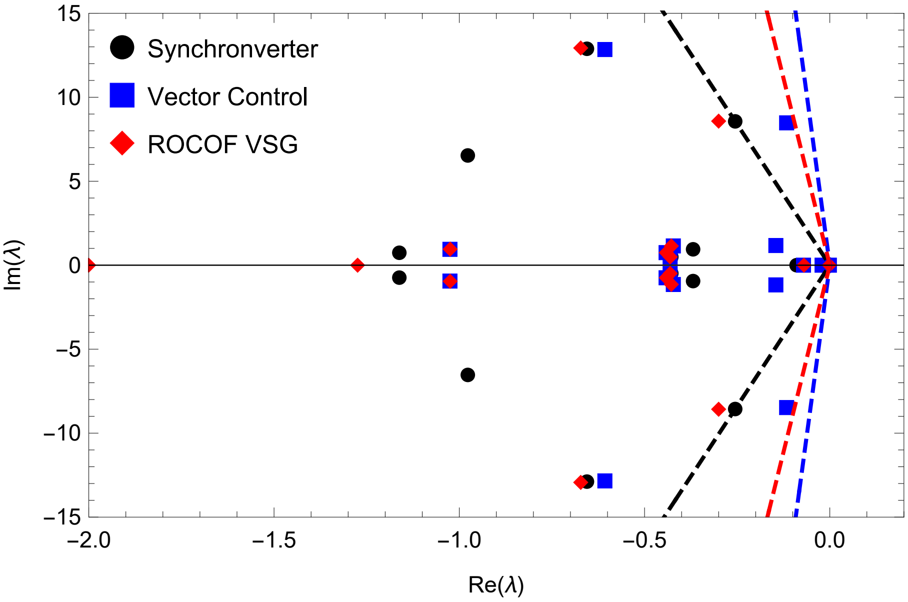

Figure 4.4: Modes of the system

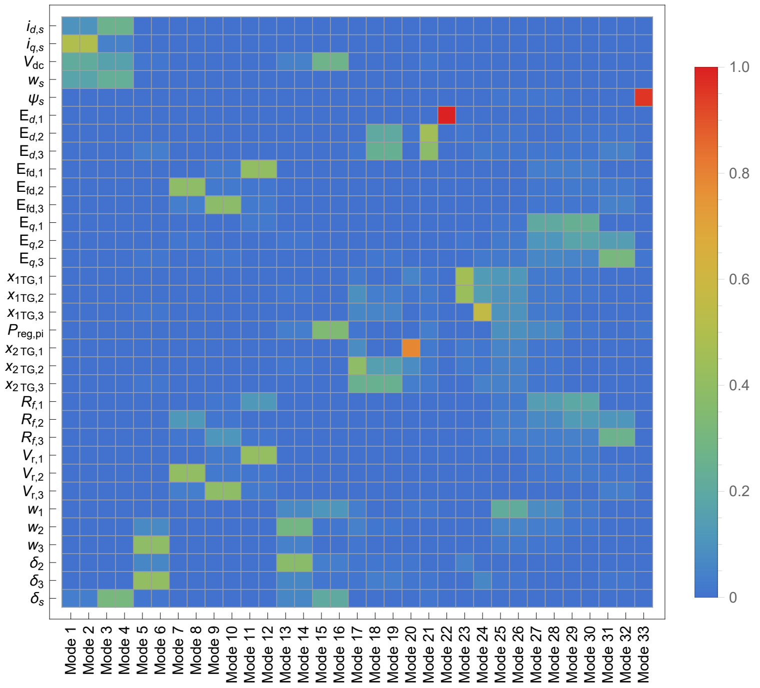

Figure 4.5: Participation matrix for the system with synchronverter

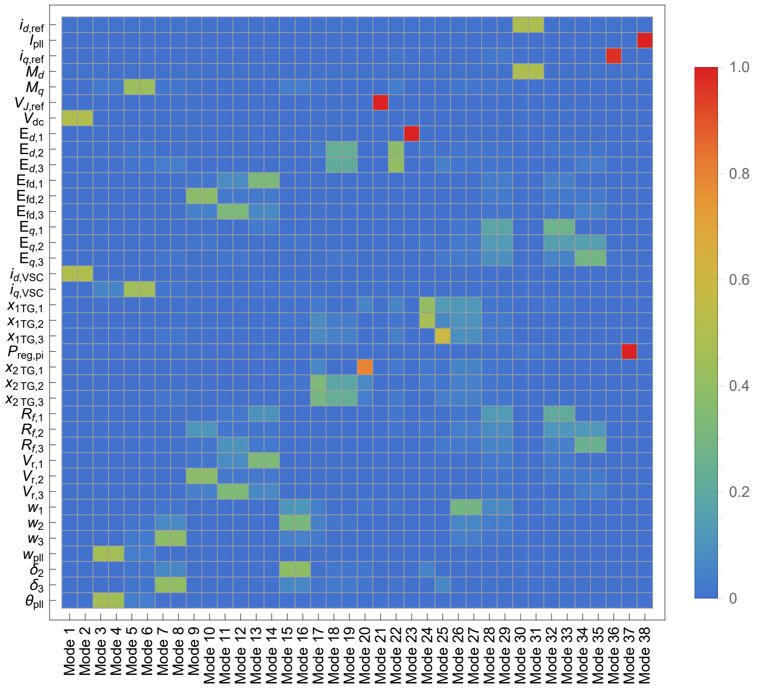

Figure 4.6: Participation matrix for the system with RoCoF VSG

Table 4.1: The eigenvalues and participation factors of the system with synchronverters

| **Eigenvalues** | **Variable** | **PF** |
|---|---|---|
| $\lambda_{1,2} = -72.53 \pm 1265.85j$ | $i_{q,s}, V_{dc}$ | $0.5, 0.2$ |
| $\lambda_{3,4} = -170.41 \pm 305.73j$ | $\delta_s, i_{d,s}, \omega_s$ | $0.32, 0.27, 0.22$ |
| $\lambda_{5,6} = -0.64 \pm 12.86j$ | $\omega_3, \delta_3$ | $0.38, 0.39$ |
| $\lambda_{7,8} = -5.5 \pm 7.95j$ | $E_{fd,2}, V_{r,2}$ | $0.4, 0.4$ |
| $\lambda_{9,10} = -5.34 \pm 7.93j$ | $E_{fd,3}, V_{r,3}$ | $0.38, 0.39$ |
| $\lambda_{11,12} = -5.25 \pm 7.86j$ | $E_{fd,1}, V_{r,1}$ | $0.39, 0.41$ |
| $\lambda_{13,14} = \mathbf{-0.25 \pm 8.56j}$ | $\omega_2, \delta_2$ | $0.29, 0.37$ |
| $\lambda_{15,16} = -1.15 \pm 6.69j$ | $p_{reg,pi}, V_{dc}$ | $0.37, 0.32$ |
| $\lambda_{17} = -5.76$ | $P_{sv,2}, P_{sv,3}$ | $0.27, 0.38$ |
| $\lambda_{18,19} = -5.26 \pm 0.45j$ | $E_{d,2}, E_{d,3}, P_{sv,3}$ | $0.2, 0.24, 0.25$ |
| $\lambda_{20} = -5.17$ | $P_{sv,1}$ | $0.79$ |
| $\lambda_{21} = -3.82$ | $E_{d,2}, E_{d,2}$ | $0.39, 0.44$ |
| $\lambda_{22} = -3.23$ | $E_{d,1}$ | $1$ |
| $\lambda_{23} = -2.37$ | $M_{mech,1}, M_{mech,2}$ | $0.44, 0.45$ |
| $\lambda_{24} = -2.32$ | $M_{mech,3}$ | $0.56$ |
| $\lambda_{25,26} = -1.12 \pm 0.82j$ | $\omega_1$ | $0.23$ |
| $\lambda_{27,28} = -0.39 \pm 0.97j$ | $E_{q,1}$ | $0.2$ |
| $\lambda_{29,30} = -0.44 \pm 0.75j$ | $E_{q,1}, R_{f,1}$ | $0.25, 0.2$ |
| $\lambda_{31,32} = -0.43 \pm 0.49j$ | $E_{q,3}, R_{f,3}$ | $0.26, 0.31$ |
| $\lambda_{33} = -0.09$ | $\psi_s$ | $0.99$ |

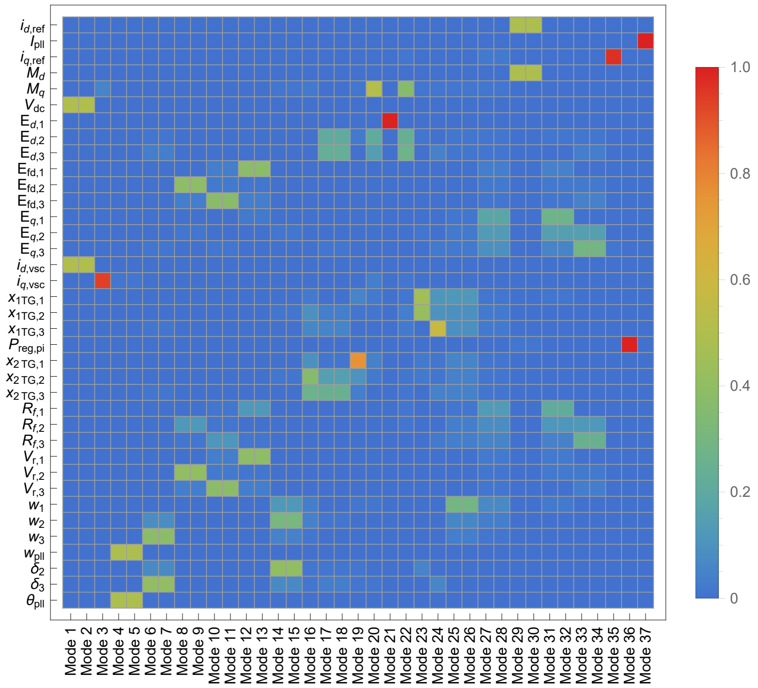

Figure 4.7: Participation matrix for the system with vector control

Table 4.2: The eigenvalues and participation factors of the system with RoCoF VSG

| **Eigenvalues** | **Variable** | **PF** |
|---|---|---|
| $\lambda_{1,2} = \mathbf{-8.27 \pm 739.62}j$ | $i_{d,vsc}, V_{dc}$ | $0.49, 0.5$ |
| $\lambda_{3,4} = -1.25 \pm 26.25j$ | $\omega_{pll}, \theta_{pll}$ | $0.44, 0.45$ |
| $\lambda_{5,6} = -11.41 \pm 13.03j$ | $i_{q,vsc}, M_q$ | $0.44, 0.4$ |
| $\lambda_{7,8} = -0.67 \pm 12.91j$ | $\omega_3, \delta_3$ | $0.39, 0.4$ |
| $\lambda_{9,10} = -5.49 \pm 7.95j$ | $E_{fd,2}, V_{r,2}$ | $0.38, 0.38$ |
| $\lambda_{11,12} = -5.32 \pm 7.91j$ | $E_{fd,3}, V_{r,3}$ | $0.32, 0.33$ |
| $\lambda_{13,14} = -5.24 \pm 7.82j$ | $E_{fd,1}, V_{r,1}$ | $0.32, 0.33$ |
| $\lambda_{15,16} = -0.31 \pm 8.56j$ | $\omega_2, \delta_2$ | $0.31, 0.39$ |
| $\lambda_{17} = -5.85j$ | $P_{sv,2}, P_{sv,3}$ | $0.3, 0.32$ |
| $\lambda_{18,19} = -5.26 \pm 0.44j$ | $E_{d,2}, E_{d,3}, P_{sv,3}$ | $0.21, 0.22, 0.23$ |
| $\lambda_{20} = -5.17$ | $P_{sv,1}$ | $0.81$ |
| $\lambda_{21} = -4.99$ | $V_{J,ref}$ | $0.98$ |
| $\lambda_{22} = -3.29$ | $E_{d,2}, E_{d,3}$ | $0.37, 0.39$ |
| $\lambda_{23} = -3.23$ | $E_{d,1}$ | $1$ |
| $\lambda_{24} = -2.37$ | $M_{mech,1}, M_{mech,2}$ | $0.4, 0.48$ |
| $\lambda_{25} = -2.31$ | $M_{mech,3}$ | $0.6$ |
| $\lambda_{26,27} = -1.01 \pm 0.96j$ | $\omega_1$ | $0.28$ |
| $\lambda_{28,29} = -0.44 \pm 1.17j$ | $E_{q,1}$ | $0.2$ |
| $\lambda_{30,31} = -0.02 \pm 1.17j$ | $i_{d,ref}, M_d$ | $0.45, 0.45$ |
| $\lambda_{32,33} = -0.44 \pm 0.75j$ | $E_{q,1}, R_{f,1}$ | $0.22, 0.28$ |
| $\lambda_{34,35} = -0.43 \pm 0.49j$ | $E_{q,3}, R_{f,3}$ | $0.24, 0.29$ |
| $\lambda_{36} = -0.07$ | $i_{q,ref}$ | $0.97$ |
| $\lambda_{37} = -0.02$ | $p_{reg,pi}$ | $1$ |
| $\lambda_{38} = -0.02$ | $I_{pll}$ | $1$ |

Table 4.3: The eigenvalues and participation factors of the system with vector control

| **Eigenvalues** | **Variable** | **PF** |
|---|---|---|
| $\lambda_{1,2} = -34.72 \pm 738.89j$ | $i_{d,vsc}, V_{dc}$ | $0.49, 0.5$ |
| $\lambda_3 = -74.59$ | $i_{q,vsc}$ | $0.92$ |
| $\lambda_{4,5} = \mathbf{-0.17 \pm 27.3}j$ | $\omega_{pll}, \theta_{pll}$ | $0.49, 0.49$ |
| $\lambda_{6,7} = -0.61 \pm 12.84j$ | $\omega_3, \delta_3$ | $0.38, 0.39$ |
| $\lambda_{8,9} = -5.5 \pm 7.95j$ | $E_{fd,2}, V_{r,2}$ | $0.39, 0.4$ |
| $\lambda_{10,11} = -5.33 \pm 7.92j$ | $E_{fd,3}, V_{r,3}$ | $0.37, 0.38$ |
| $\lambda_{12,13} = -5.24 \pm 7.84j$ | $E_{fd,1}, V_{r,1}$ | $0.38, 0.39$ |
| $\lambda_{14,15} = -0.12 \pm 8.48j$ | $\omega_2, \delta_2$ | $0.31, 0.4$ |
| $\lambda_{16} = -5.76 \pm$ | $P_{sv,2}, P_{sv,3}$ | $0.26, 0.36$ |
| $\lambda_{17,18} = -5.26 \pm 0.45j$ | $E_{d,2}, E_{d,3}, P_{sv,3}$ | $0.21, 0.23, 0.25$ |
| $\lambda_{19} = -5.16$ | $P_{sv,1}$ | $0.76$ |
| $\lambda_{20} = -4.28$ | $M_q$ | $0.53$ |
| $\lambda_{21} = -3.23$ | $E_{d,1}$ | $1$ |
| $\lambda_{22} = -3.04$ | $E_{d,2}, E_{d,3}, M_q$ | $0.25, 0.28, 0.3$ |
| $\lambda_{23} = -2.37$ | $M_{mech,1}, M_{mech,2}$ | $0.41, 0.46$ |
| $\lambda_{24} = -2.31$ | $M_{mech,3}$ | $0.59$ |
| $\lambda_{25,26} = -1.03 \pm 0.95j$ | $\omega_1$ | $0.29$ |
| $\lambda_{27,28} = -0.42 \pm 1.15j$ | $E_{q,1}$ | $0.2$ |
| $\lambda_{29,30} = -0.15 \pm 1.17j$ | $i_{d,ref}, M_d$ | $0.49, 0.48$ |
| $\lambda_{31,32} = -0.44 \pm 0.75j$ | $E_{q,1}, R_{f,1}$ | $0.21, 0.28$ |
| $\lambda_{33,34} = -0.43 \pm 0.49j$ | $E_{q,3}, R_{f,3}$ | $0.24, 0.29$ |
| $\lambda_{35} = -0.07$ | $i_{q,ref}$ | $0.97$ |
| $\lambda_{36} = -0.02$ | $p_{reg,pi}$ | $1$ |
| $\lambda_{37} = -0.02$ | $I_{pll}$ | $1$ |

### 4.2.2 Transient stability

Transient stability was defined in the second chapter. The most severe disturbance that can occur in the power system is three-phase fault. Hence, this section presents the results of the simulation of the transient stability of the IEEE 9 bus system for different control topologies of VSC. In the scenario of the study, the fault occurs on line 8-9 at $t_{sim} = 1s$. The faulty line is disconnected after the fault is cleared. In this study two clearing times were considered: $t_{cl} = 0.1s$ and $t_{cl} = 0.2s$. A clearing time of 200ms is a conservative estimation that is used in stability studies by European grid operators [52]. The simulation was run for 20s to demonstrate the response of the generator load angles to a severe disturbance.

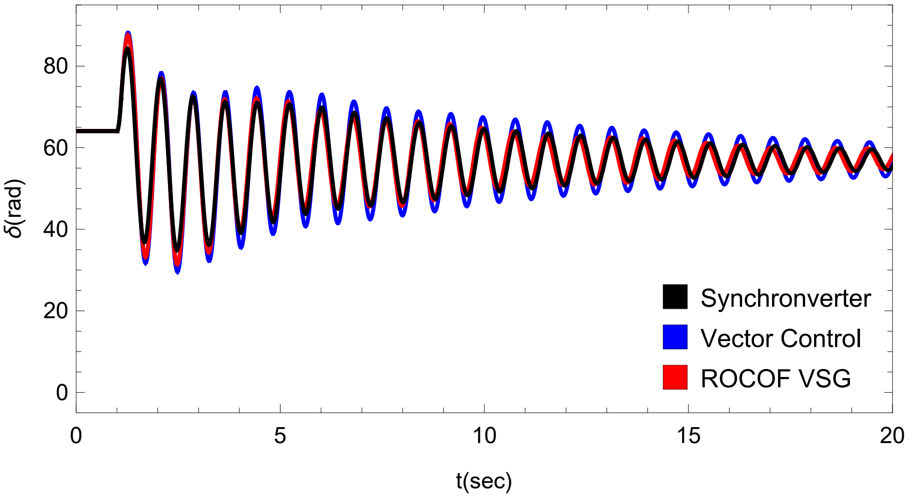

Figure 4.8: Load angle of the second generator after threee phase fault for $t_{cl} = 0.1s$.

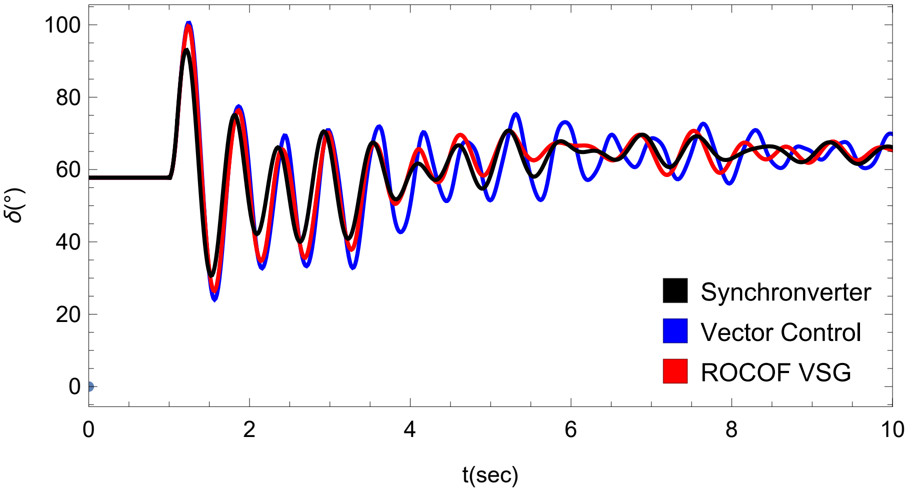

Figure 4.9: Load angle of the third generator after threee phase fault for $t_{cl} = 0.1s$.

Fig. 4.8 and 4.9 show the response of load angles of the second and third machine during and after the three-phase fault that was cleared in 100ms. From

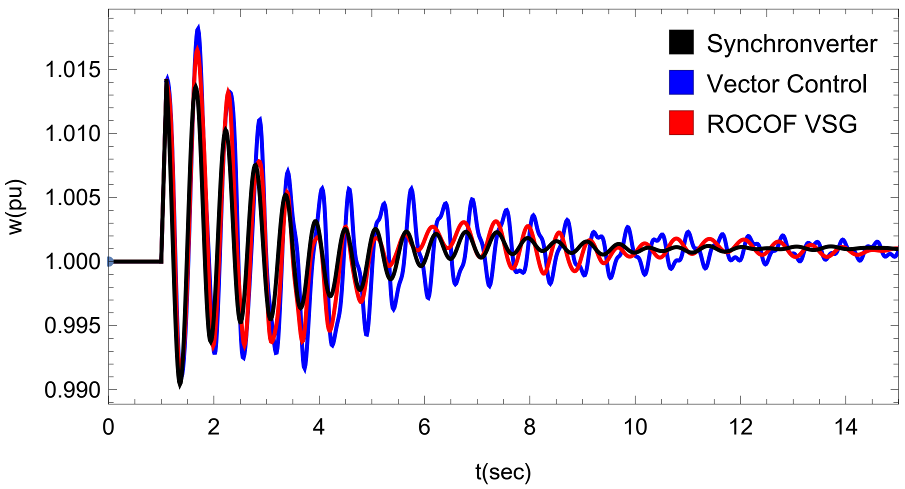

Figure 4.10: Angular velocity of the third generator after threee phase fault for $t_{cl} = 0.1s$.

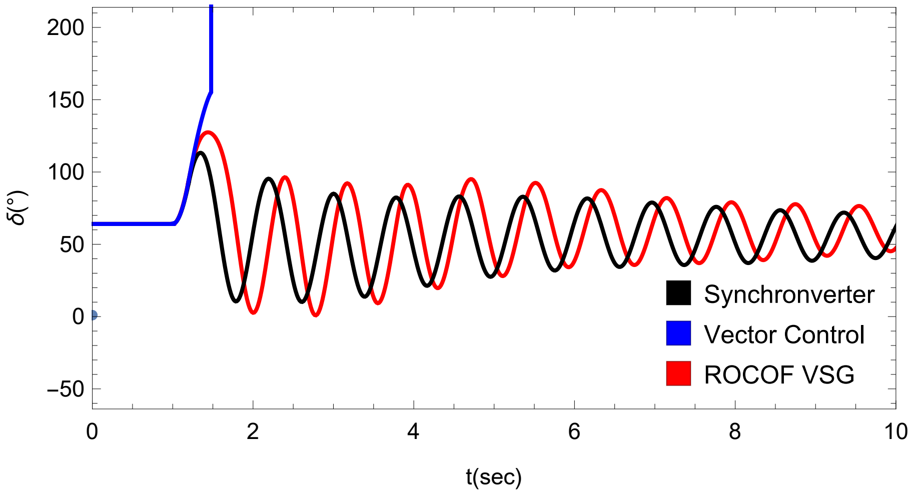

Figure 4.11: Load angle of the second generator after threee phase fault for $t_{cl} = 0.2s$.

the figure is clear that the system with vector control performes the worst of all three. The system with synchronverter (black line) has better performance than the system with RoCoF VSG both in terms of maximal load angle deviation and overall damping of oscillations. That is not surprising since that was expected from the results of the modal analysis.

Fig. 4.10 shows the angular velocity of the third generator during the simulation. Essentially the oscillations of the generator speed propagate to the load angle thus, the result is similar. In the case of vector control, the angular velocity has the highest deviation from the nominal value. It likewise demonstrates more effective damping of the oscillations in the system with a synchronverter.

The results of the simulation for $t_{cl} = 0.2s$ are provided in fig. 4.11 and 4.12. For the clearing time of 200ms the system witht vector control is unstable. These

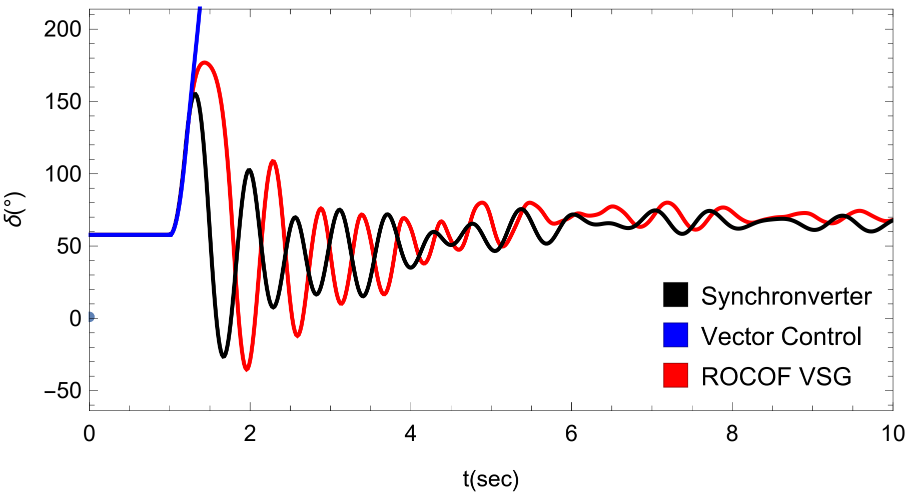

Figure 4.12: Load angle of the third generator after threee phase fault for $t_{cl} = 0.2s$.

results demonstrate that undoubtedly grid-following VSG improves the system's stability. Nevertheless, the synchronverter provides a better initial response i.e. the generators do not speed up as much and better damping of oscillations as well. In this study different placements of the VSCs were considered. Two PV power plants, each producing 0.8 p.u., were connected to different nodes, excluding the nodes with generators.

### 4.2.3 Effects of placement of virtual inertia

The importance of virtual inertia placement was emphasized in [53]. To investigate the effects of placement of different control topologies on the stability of the system, a larger benchmark grid was utilised. Fig. 4.13 shows IEEE 39 bus, it is a common test case system for research and analysis. The system parameters can be found in the IEEE PES report [54] and parameters of the examined control strategies are provided in the paper [15].

The effects of inertia placement were investigated using modal analysis since it allows to gain insights about system behavior without directly solving differential equations. The control quality criteria that were discussed previously in 2.3.4 were calculated for the possible configurations of the grid. The lowest-mode damping and $max(Re(\lambda))$ were the chosen criteria for comparison.

Fig. 4.14 4.15 and 4.16 show the results of the calcualtion of the lowest-mode damping. Comparing these fig. one may conclude that overall the application of the grid-forming control improves the damping of the system. As expected, the RoCoF VSG (fig. 4.15 ) improves the lowest damping mode comparing to the system with vector control (fig.4.14), less than a synchronverter though.

The computed $max(Re(\lambda))$ for different control strategies are presented in fig.

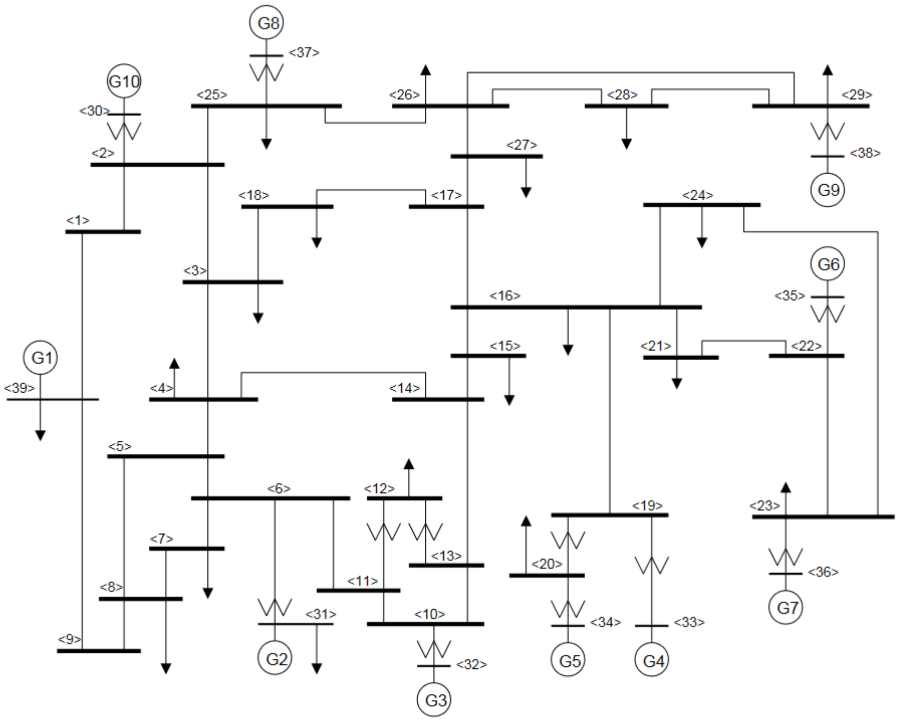

Figure 4.13: Line diagram of IEEE 39 bus benchmark system. Adopted from [54].

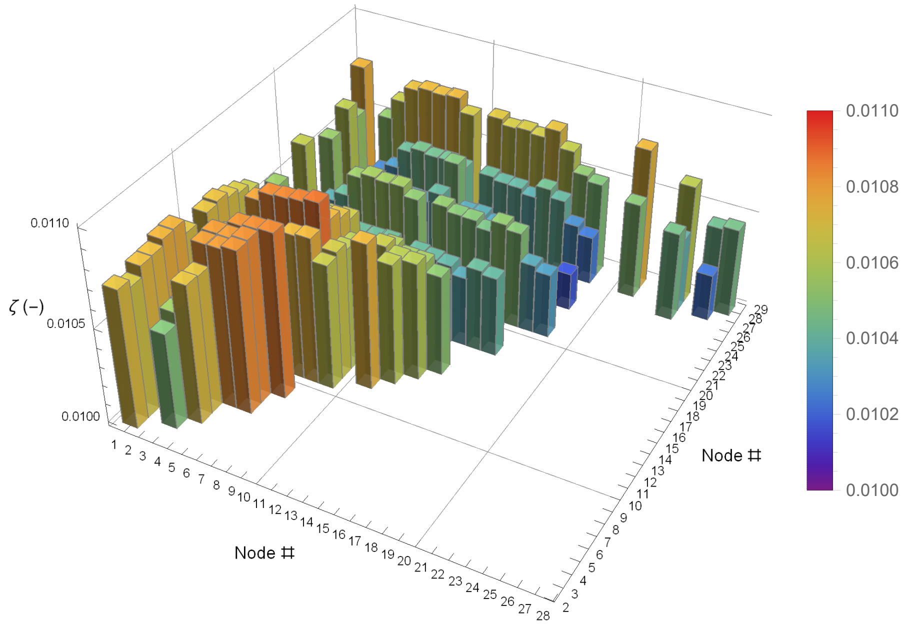

Figure 4.14: Lowest damping ratios for VSCs with vector control connected to different nodes

4.17 4.18 and 4.19. This performance index demonstrates that indeed synchronverter control substantially improves the ability of the system to return to the steady-state compared to other examined control topologies. Interestingly, for RoCoF the $max(Re(\lambda))$ in this case is similar to the vector control which can be explained that this mode is dictated by the PLL. Thus, this again supports the

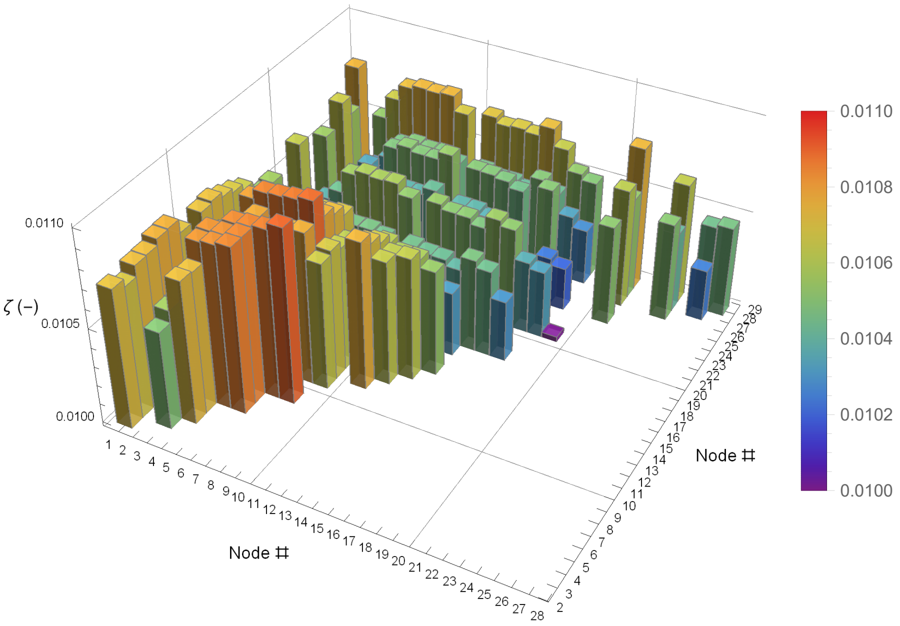

Figure 4.15: Lowest damping ratios for VSCs with RoCoF VSG control connected to different nodes

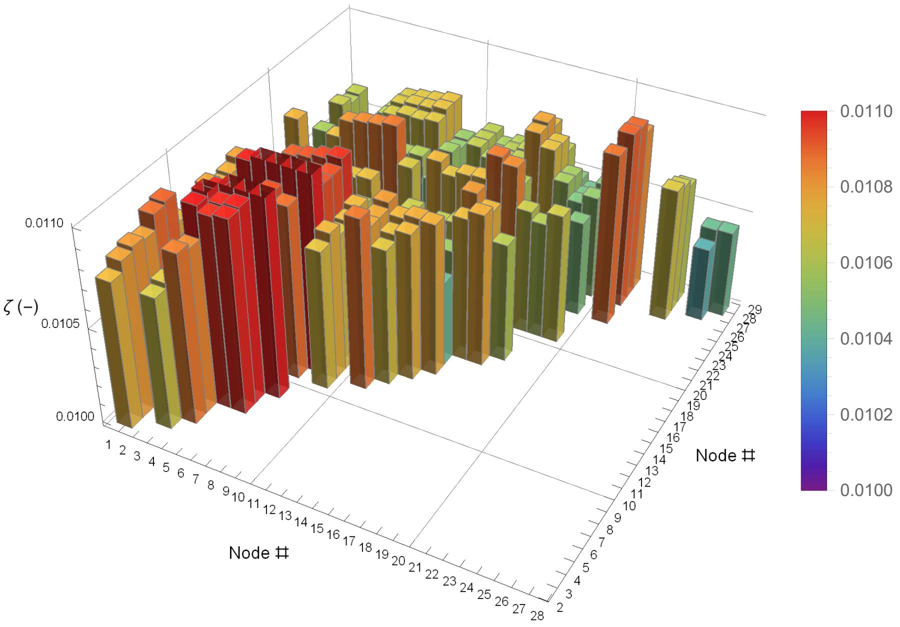

Figure 4.16: Lowest damping ratios for VSCs with synchronverter control connected to different nodes

claim that PLL is one of the major factors that contribute to the performance of the CIGs [15]. It should be noted that for the synchronverter, the placement is indeed important and can influence the value of $max(Re(\lambda))$ of the system considerably.

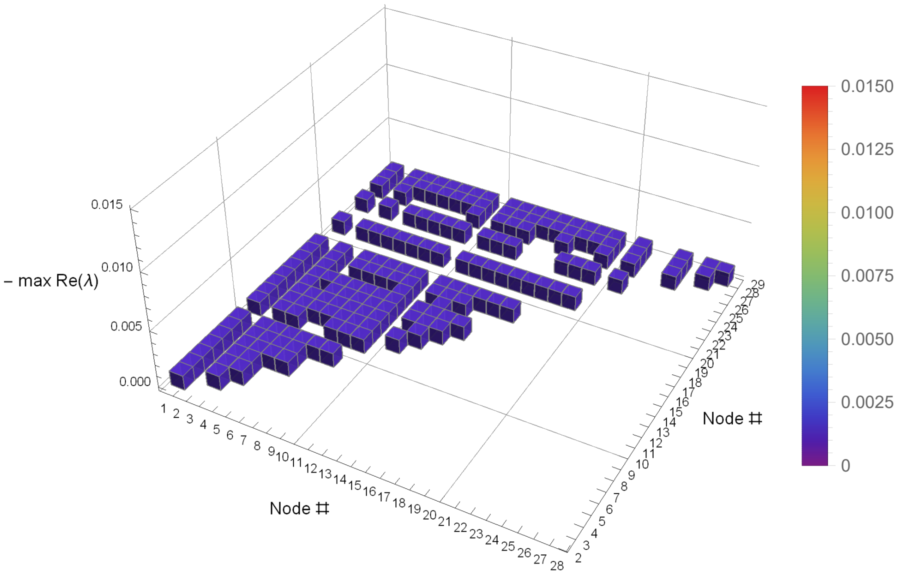

Figure 4.17: $max(Re(\lambda))$ for VSCs with vector control connected to different nodes

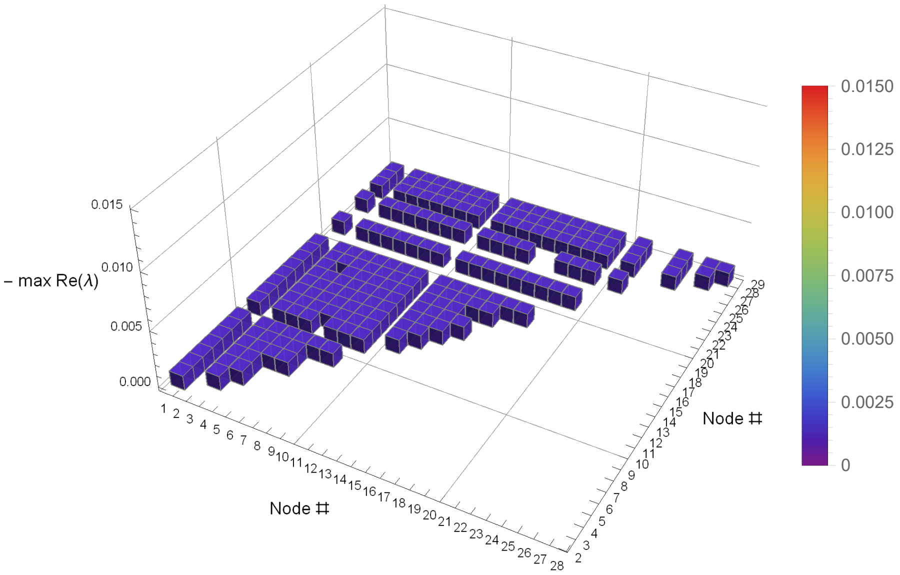

Figure 4.18: $max(Re(\lambda))$ for VSCs with RoCoF VSG control connected to different nodes

### 4.2.4 Summarizing the results

The subsection briefly summarizes the presented results of the comparisons of three examined control topologies. In section 4.2.1, the modal analysis clearly demonstrates that RoCoF VSG improves the overall small-signal stability of the system compared to traditional vector cotnrol. Nevertheless, the synchronverter has better damping and placement of the modes. The simulation results of the system's transient stability fully supported the modal analysis's conclusions. Furthermore, the transient stability study also shows that RoCoF VSG

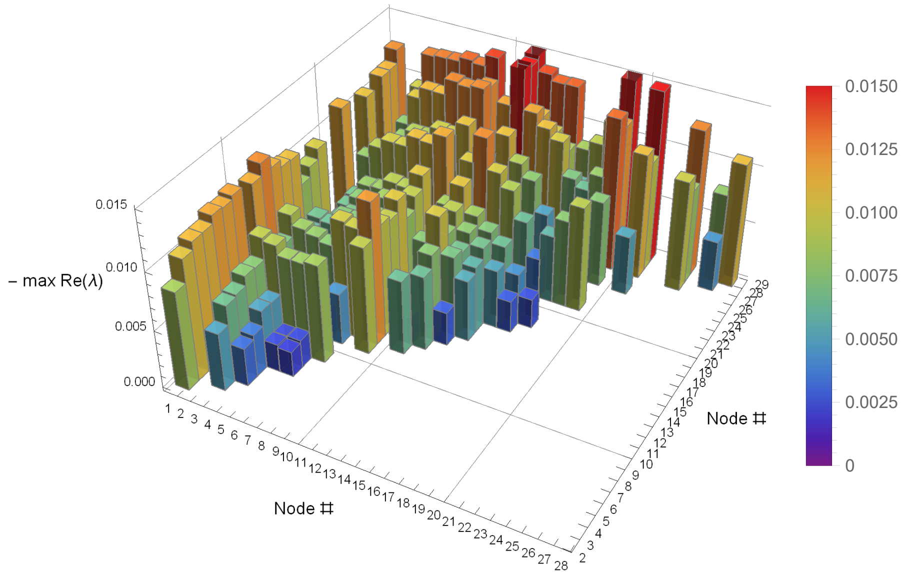

Figure 4.19: $max(Re(\lambda))$ for VSCs with synchronverter control connected to different nodes

and synchronverter can sustain longer clearing times.

The placement analysis yielded that in terms of lowest damping, the RoCoF VSG is better than traditional vector control, however the system with a synchronverter has even higher damping. The obtained $max(Re(\lambda))$ for the different configurations of the network were similar for vector control and RoCoF VSG, which is explained by the PLL modes. For the grid-forming control, however, this index can vary substantially depending on the placement. Therefore, the performance of the system is dependent not only on the placement of the virtual inertia but on the control strategy as well [15]. To sum up, the presented results, in the author's opinion, demonstrate that grid-forming control is preferable to other control strategies.

## 4.3 Increasing virtual inertia capability by adding ESS

The previous section compared three control strategies. The results of the compariosn yielded that the grid-forming type of VSG is preferable to other control topologies. Therefore, this section examines the possibility of increasing the virtual inertia capability of a grid-forming VSG using ESS[1].

For the ESS, the supercapacitor storage was chosen because it has a higher available power reserve than batteries as fig. 1.3 shows. Theoretically, VSGs with supercapacitors using proper control can emulate large synchronous machines

---

[1] In this section sometimes the author refers to the VSG with ESS as just VSG

[55]. It should be noted that generally, virtual inertia is constrained to be total energy storage in VSGs [56]. The constraint can be put as follows: $J_{vsg}\frac{\omega_{vsg}^2}{2} \leq E_{ess}$. Thus, energy storage specifications are given by required inertia.

Also, this section describes an attempt to replace a generator with a VSG with ESS. Hence, the comparison will be between a grid-forming VSG and a conventional SG. Furthermore, a DC bus voltage stabilizer is proposed in order to improve the stability of the system. In this section, firstly, the mathematical model of the VSG with ESS is outlined. Afterwards , a stability analysis of the system with the examined VSG, which includes ESS is conducted. At the end, the quality of frequency control is examined.

### 4.3.1 Mathematical model of the VSG with ESS

Fig. 4.20 shows the block diagram of the VSG with ESS. In this subsection, the necessary changes to the mathematical model of the synchronverter are outlined. The model can be divided into three parts: the electrical part, VSG control, and ESS control.

The mathematical model of the VSG with ESS does not change much. The equations provided in the section 4.1.1 do not change. The model of the ESS is connected to the electrical part of the VSC. Also, the control of the ESS is added.

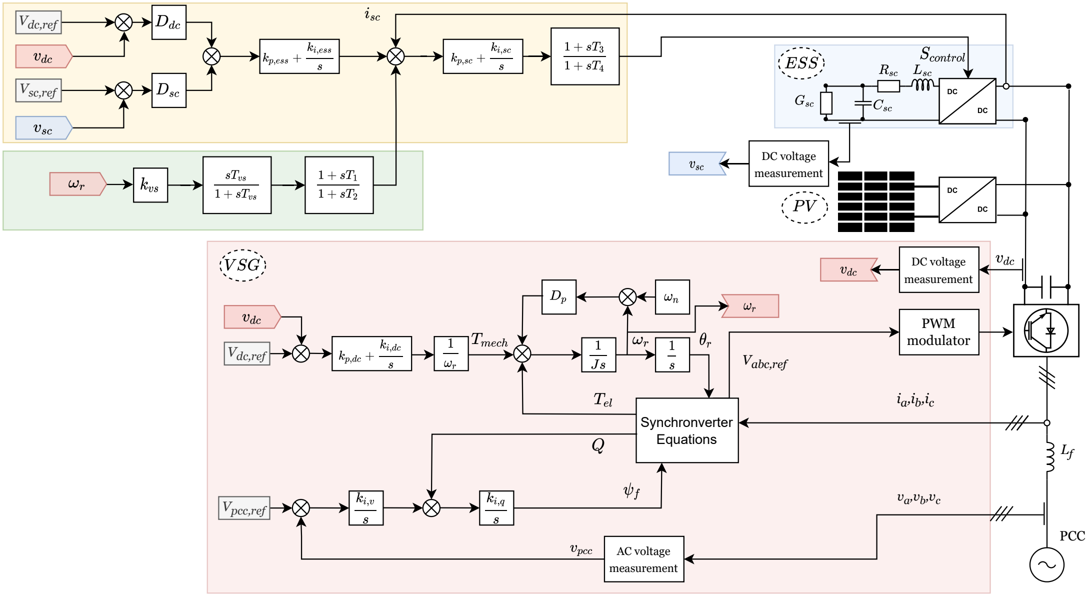

Figure 4.20: Block diagram of the proposed control scheme.

To eq. (3.38) describing the dynamics of the DC bus the power exchanges with the ESS is added:

$$C_{dc}\frac{\mathrm{d}v_{dc}}{\mathrm{d}t} = \frac{p_{pv} + p_{ess} - p_{vsc}}{v_{dc}} \tag{4.22}$$

where $p_{ess}$ is power stored/released from the supercapacitor.

Since the study mostly focuses on the overall dynamics of the PS, the authors chose to use a relatively simple dynamic model of ultracapacitor with bidirectional DC/DC converter provided in [57]. In the figure 4.20, the electric part of supercapacitor ESS is highlighted in blue. The mathematical model that describes the dynamics of bidirectional operation of the supercapacitor storage is as follows:

$$C_{sc}\frac{\mathrm{d}v_{sc}}{\mathrm{d}t} = -(i_{sc} + G_{sc}v_{sc}) \tag{4.23}$$

$$L_{sc}\frac{\mathrm{d}i_{sc}}{\mathrm{d}t} = (v_{sc} - R_{sc}i_{sc} - Sv_{dc}) \tag{4.24}$$

$$i_{dc} = Si_{sc} \tag{4.25}$$

where $C_{sc}$ is ESS cpacitance, $L_{sc}$, $R_{sc}$ is ESS inductance and resistance and $G_{sc}$ is leakage. The control signal $S$ for the average model represents the duty cycle of the converter [57].

### 4.3.2 ESS control and proposed voltage stabilizer for DC bus

The block diagram of the subsystem that controls the power exchange with energy storage is divided into two parts is shown in fig. 4.20. The part of the control which is highlighted in yellow is a naive way of implementing such control. The proposed compensator that stabilizes the DC voltage is highlighted in green.

Let's first analyze the naive part of the proposed control scheme. In the proposed control, both DC voltages are controlled through drooping coefficients. $D_{dc}$ corresponds to DC bus voltage and $D_{sc}$ to supercapacitor voltage. The output of the differences between voltage references and actual values are multiplied by droop coefficients and go to the common voltage controller. The mathematical form of the equations therefore is:

$$i_{ess,ref} = K_{p,ess}\Delta_v + M_{ess} \tag{4.26}$$

where $\Delta_v = D_{dc}(v_{dc,ref} - v_{dc}) + D_{sc}(v_{sc,ref} - v_{sc})$

$$\frac{\mathrm{d}M_{ess}}{\mathrm{d}t} = D_{dc}(v_{dc,ref} - v_{dc}) + D_{sc}(v_{sc,ref} - v_{sc}) \tag{4.27}$$

The controller's output is the current reference that goes into the current controller, and the action produced by that controller goes then into the lead-lag compensator, which improves the control response.

$$\alpha = K_{p,sc}(i_{ess,ref} - i_{ess}) + M_{isc} \tag{4.28}$$

$$\frac{\mathrm{d}M_{isc}}{\mathrm{d}t} = K_{i,sc}(i_{ess,ref} - i_{ess}) \tag{4.29}$$

The output of lead-lag block is control action $S$, which is defined as follows:

$$T_4\frac{\mathrm{d}S}{\mathrm{d}t} = T_3\frac{\mathrm{d}\alpha}{\mathrm{d}t} + \alpha - S \tag{4.30}$$

It should be highlighted that the system with a naive implementation of control is unstable in cases of short circuit faults. Therefore the voltage stabilizer is introduced. A power system stabilizer partially inspires the compensation scheme. Eq. (3.38) and (4.9) result that in case of VSG the DC voltage is directly connected to virtual velocity change. Therefore, the compensation scheme that is based on virtual velocity can reduce DC bus voltage deviations during transients. Hence, this part of ESS control can be referred to as a voltage stabilizer (VS). The ESS will be charged/discharged based on the virtual machine's swing, resulting in smaller deviations of DC bus voltage. The VS consists of three blocks, firstly, the input signal i.e. virtual velocity, is multiplied by the gain. The result then goes into the washout filter, and after that signal goes through the lead-lag compensator.

$$T_w\frac{dv_w}{dt} = K_{vs}\frac{d\omega_r}{dt} - v_w \tag{4.31}$$

where $K_{vs}$ is voltage stabilizer gain, $T_w$ is constant of washout filter and $v_w$ is state variable of the system representing dynamics of washout filter.

$$T_2\frac{di_{vs}}{dt} = T_1\frac{dv_w}{dt} + i_{vs} - v_w \tag{4.32}$$

where $T_1, T_2$ are time constants of lead-lag block and $i_{vs}$ is the output of VS subsystem that goes into current reference that controls ESS current exchange with DC bus of the VSG.

### 4.3.3 Modal analysis

This section analysis the small-signal stability of the IEEE 39 bus system with VSG (parameters are provided in Appendix I). For the comparison of stability, the generator connected to node 37 is replaced by VSG with ESS. Hence, in this study three cases are compared a conventional SG, VSG and VSG with proposed voltage stabilizer for DC bus. The steps for the analysis are similar as described in section 4.2.1.

The computed eigenvalues of the system with VSG w/o VS are presented in tab. 4.4. Tab. 4.5 shows the computed eigenvalues of the same system but with DC voltage stabilizer. The eigenvalues of the conventional IEEE 39 bus system can be found in tab. 4.6. Fig. 4.21 visualizes the eigenvalues of the PS for different cases mentioned above.

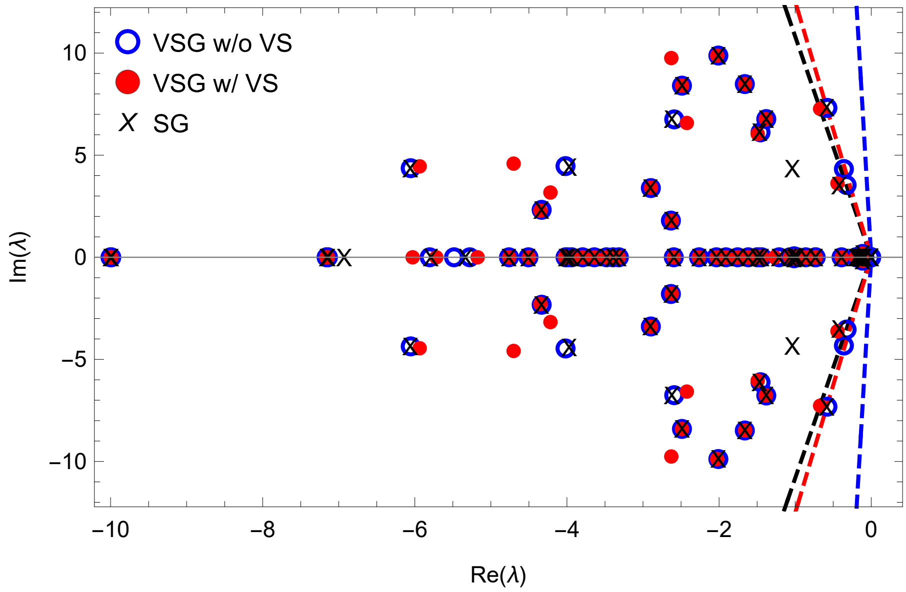

Figure 4.21: Eigenvalues of the system with different devices connected to node 37.

Table 4.4: Computed eigenvalues of the system with VSG w/o VS

| | | | | | | | |
|---|---|---|---|---|---|---|---|
| $-3521.58$ | $-65.42$ | $-5.48$ | $-1.91$ | $-0.18$ | | | |
| $-2287.94$ | $-64.02$ | $-5.28$ | $-1.76$ | $-0.18$ | | | |
| $-467.77$ | $-63.52$ | $-4.76$ | $-1.62$ | $-0.17$ | | | |
| $-104.63$ | $-62.06$ | $-4.51$ | $-1.5$ | $-0.15$ | | | |
| $-103.81$ | $-59.75$ | $-4.02$ | $-1.49$ | $-0.14$ | $-64.47 \pm 1.14j$ | $-12.7 \pm 7.07j$ | $\mathbf{-7.51 \pm 479.57j}$ |
| $-102.69$ | $-50$ | $-3.99$ | $-1.44$ | $-0.1$ | $-6.05 \pm 4.36j$ | $-4.33 \pm 2.32j$ | $-4.02 \pm 4.47j$ |
| $-102.28$ | $-31.54$ | $-3.94$ | $-1.21$ | $-0.1$ | $-2.9 \pm 3.39j$ | $-2.63 \pm 1.8j$ | $-2.59 \pm 6.75j$ |
| $-102.12$ | $-18.04$ | $-3.79$ | $-1.07$ | $-0.1$ | $-2.49 \pm 8.41j$ | $-2.01 \pm 9.88j$ | $-1.66 \pm 8.48j$ |
| $-101.88$ | $-14.71$ | $-3.64$ | $-1$ | $-0.1$ | $-1.46 \pm 6.12j$ | $-1.38 \pm 6.77j$ | $-1.01 \pm 0.05j$ |
| $-101.34$ | $-10$ | $-3.48$ | $-0.97$ | $-0.1$ | $-0.58 \pm 7.32j$ | $-0.36 \pm 4.32j$ | $-0.32 \pm 3.54j$ |
| $-101.17$ | $-9.99$ | $-3.39$ | $-0.86$ | $-0.1$ | $-0.17 \pm 0.01j$ | $-0.11 \pm 0.16j$ | $-0.01 \pm 0.01j$ |
| $-100.91$ | $-7.16$ | $-3.32$ | $-0.73$ | $-0.1$ | | | |
| $-72.89$ | $-7.15$ | $-2.6$ | $-0.73$ | $-0.1$ | | | |
| $-65.97$ | $-7.14$ | $-2.26$ | $-0.39$ | $-0.1$ | | | |
| $-65.89$ | $-5.8$ | $-2.04$ | $-0.2$ | $-0.09$ | | | |
| $-10^{-4}$ | | | | | | | |

In the tab. 4.4, 4.5 and 4.6 the modes with smallest damping ratios are highlighted. For the naive implementation of VSG i.e, without DC VS the smallest damping ratio is $\zeta_{min,vsgw/ovs} = 0.015$. The proposed control scheme i.e, with DC VS improves the smallest damping ratio of the system $\zeta_{min,vsg} = 0.079$. Nevertheless, it is still slightly worse than for a conventional system $\zeta_{min} = 0.092$. In the fig. 4.21 blue dashed lines correspond to the smallest damping ratio of the system

Table 4.5: Computed eigenvalues of the system with VSG w/ VS

| | | | | | | | |
|---|---|---|---|---|---|---|---|
| −3522.58 | −65.89 | −5.79 | −1.91 | −0.18 | | | |
| −2287.94 | −65.41 | −5.33 | −1.76 | −0.18 | | | |
| −478.68 | −64.44 | −4.76 | −1.62 | −0.17 | | | |
| −402.33 | −64. | −4.51 | −1.5 | −0.15 | | | |
| −104.57 | −63.53 | −4.01 | −1.49 | −0.14 | | | |
| −103.81 | −61.83 | −3.98 | −1.44 | −0.1 | $-38.95 \pm 487.41j$ | $-12.7 \pm 7.07j$ | $-7.12 \pm 0.02j$ |
| −102.69 | −59.57 | −3.94 | −1.21 | −0.1 | $-6.06 \pm 4.35j$ | $-4.84 \pm 32.94j$ | $-4.34 \pm 2.32j$ |
| −102.28 | −50. | −3.79 | −1.07 | −0.1 | $-3.97 \pm 4.41j$ | $-2.9 \pm 3.39j$ | $-2.63 \pm 1.8j$ |
| −102.12 | −31.54 | −3.64 | −1. | −0.1 | $-2.62 \pm 6.77j$ | $-2.49 \pm 8.41j$ | $-2.01 \pm 9.88j$ |
| −101.84 | −18.04 | −3.48 | −0.97 | −0.1 | $-1.66 \pm 8.48j$ | $-1.47 \pm 6.13j$ | $-1.38 \pm 6.77j$ |
| −101.34 | −14.71 | −3.39 | −0.86 | −0.1 | $-1.04 \pm 4.36j$ | $-1.01 \pm 0.05j$ | $-\mathbf{0.58 \pm 7.33j}$ |
| −101.17 | −10. | −3.32 | −0.73 | −0.1 | $-0.42 \pm 3.52j$ | $-0.17 \pm 0.01j$ | $-0.11 \pm 0.16j$ |
| −100.91 | −9.99 | −2.6 | −0.73 | −0.1 | | | |
| −72.89 | −7.16 | −2.26 | −0.39 | −0.1 | | | |
| −65.97 | −7.14 | −2.04 | −0.2 | −0.09 | | | |
| −0.04 | −0.02 | −0.01 | | | | | |

Table 4.6: Computed eigenvalues of the system with SG

| | | | | | | | |
|---|---|---|---|---|---|---|---|
| −2370.11 | −65.22 | −6.02 | −2.26 | −0.38 | | | |
| −104.63 | −64.21 | −5.71 | −2.03 | −0.20 | | | |
| −103.83 | −63.97 | −5.17 | −1.91 | −0.18 | | | |
| −102.73 | −63.48 | −4.76 | −1.75 | −0.17 | | | |
| −102.28 | −61.64 | −4.5 | −1.61 | −0.17 | | | |
| −102.15 | −59.51 | −4.02 | −1.49 | −0.15 | $-12.7 \pm 7.06j$ | $-5.94 \pm 4.45j$ | $-4.7 \pm 4.59j$ |
| −102.02 | −50 | −3.99 | −1.49 | −0.14 | $-4.35 \pm 2.28j$ | $-4.21 \pm 3.17j$ | $-2.9 \pm 3.4j$ |
| −101.52 | −31.55 | −3.93 | −1.26 | −0.14 | $-2.63 \pm 9.76j$ | $-2.62 \pm 1.79j$ | $-2.49 \pm 8.41j$ |
| −101.33 | −18.10 | −3.79 | −1.06 | −0.10 | $-2.42 \pm 6.58j$ | $-2.02 \pm 9.88j$ | $-1.65 \pm 8.48j$ |
| −101.16 | −14.69 | −3.64 | −1 | −0.1 | $-1.49 \pm 6.04j$ | $-1.44 \pm 0.02j$ | $-1.39 \pm 6.76j$ |
| −100.91 | −10.00 | −3.48 | −0.97 | −0.1 | $-1.02 \pm 0.05j$ | $-\mathbf{0.67 \pm 7.27j}$ | $-0.44 \pm 3.62j$ |
| −72.89 | −9.99 | −3.44 | −0.86 | −0.1 | $-0.17 \pm 0.01j$ | $-0.11 \pm 0.18j$ | |
| −65.97 | −7.16 | −3.39 | −0.82 | −0.1 | | | |
| −65.89 | −7.15 | −3.31 | −0.73 | −0.1 | | | |
| −65.41 | −7.14 | −2.59 | −0.73 | −0.1 | | | |
| −0.09 | −0.09 | | | | | | |

with VSG w/o DC VS, the gray dashed line shows the smallest damping for the system with VSG that incorporates proposed DC VS, and the black dashed line shows the worst damping ratio for the conventional system. Therefore, all other modes laying between the $x$-axis and dashed line have a higher damping ratio. Overall results clearly show that damping in the case of the naive ESS control scheme is much worse than for other presented cases.

### 4.3.4 Transient stability of VSG with ESS

The previous section was focused on analyzing the system without directly solving differential equations. In this subsection, the results of the transient stability study are presented, and the performance of the proposed control of VSG is analyzed. Several numerical simulations of IEEE 39 bus system model with VSG were conducted, for the purposes of comparing the proposed control strategy of the VSG. First of all, the subsection presentsseveral simulations in order to demonstrate the effect of VS on DC voltage. The scenario of the simulations is following at simulation time $t = 5s$ a three-phase fault occurs on line 15-16, and then the fault is cleared in $t = 5 + t_{cl}$. For the comparison, two clearing times were considered $0.1s$ and $0.2s$. DC bus voltage during simulation is shown in figure 4.22. It is clear from figure 4.22a that for $t_{cl} = 0.1$ the system is stable for both cases. However, DC VS significantly improves overvoltage and damping. For a clearing time of 200ms, the system without DC VS is unstable.

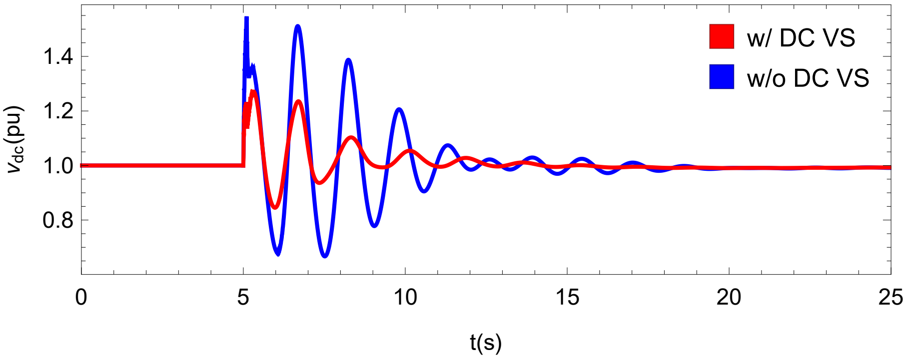

(a) DC voltage during transient for $t_{cl} = 0.2s$t

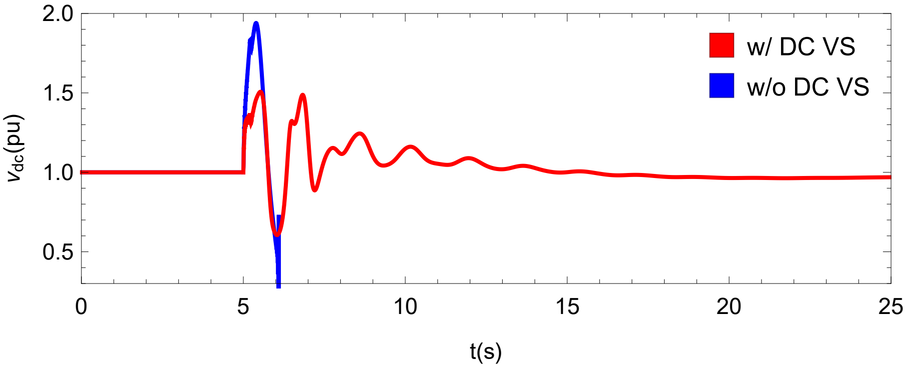

(b) DC voltage during transient for $t_{cl} = 0.2s$

Figure 4.22: VSG's DC voltage during fault on line 15-16

Table 4.7: Comparison of performance for different devices

| Line | VSG | | SG | |
|---|---|---|---|---|
| | max $\Delta\omega$ | max $\delta$ | max $\Delta\omega$ | max $\delta$ |
| $3-18$ | $14.06 \cdot 10^{-3}$ | 108.91° | $14.01 \cdot 10^{-3}$ | 108.54° |
| $4-14$ | $18.16 \cdot 10^{-3}$ | 134.25° | $18.16 \cdot 10^{-3}$ | 134.81° |
| $15-16$ | $18.96 \cdot 10^{-3}$ | 140.83° | $18.96 \cdot 10^{-3}$ | 140.73° |
| $26-28$ | $21.13 \cdot 10^{-3}$ | 179.91° | unstable | unstable |

The efficacy of the DC bus voltage stabilizer was demonstrated in the text above, hence heareafter only the proposed control of VSG is compared to the conventional system. Several simulations were conducted to compare the power system dynamics where VSG repaces SG. The scenarios of the simulations are similar differs only the faulted line. Before the fault, the power system is in a steady state. The fault occurs in time $t = 5s$, then the fault is cleared in $t = 5.2s$ and the faulted line is disconnected. As mentioned previously, the clearing time of no more than $t_{cl} = 0.2$ can be expected in European power systems [52].

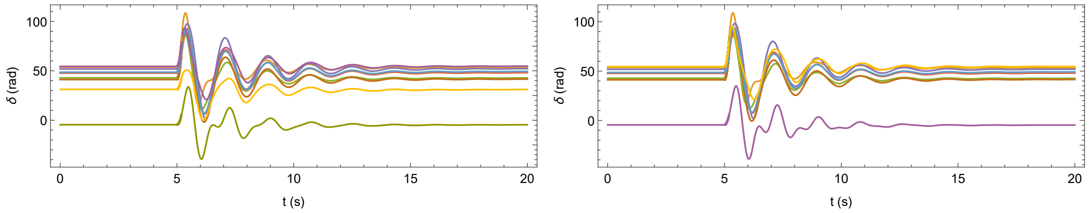

(a) Load angles of generators during transient

(b) Load angles of generators in the system with VSG during transient

Figure 4.23: Fault on the line between nodes 3-18

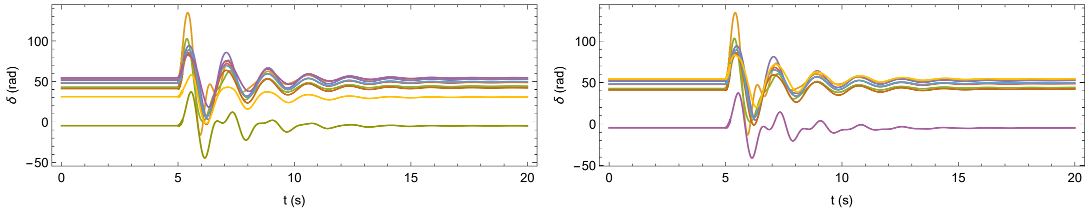

(a) Load angles of generators during transient

(b) Load angles of generators in the system with VSG during transient

Figure 4.24: Fault on the line between nodes 4-14

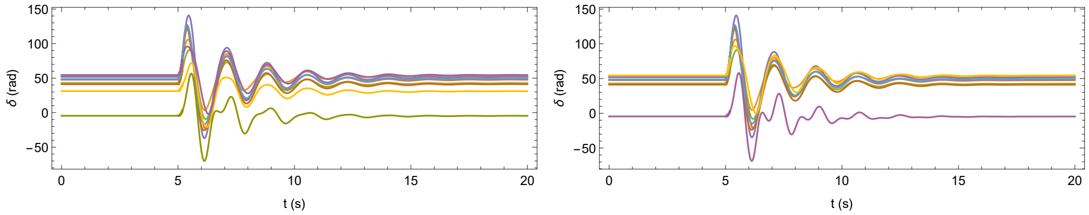

(a) Load angles of generators during transient

(b) Load angles of generators in the system with VSG during transient

Figure 4.25: Fault on the line between nodes 15-16

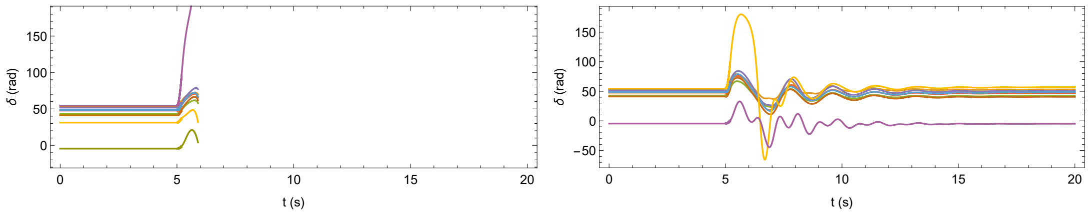

(a) Load angles of generators during transient

(b) Load angles of generators in the system with VSG during transient

Figure 4.26: Fault on the line between nodes 26-28

The results of the simulation show, for the most part, that the conventional grid and the grid with VSG perform similarly when accounted for maximum load angle deviation and angular velocity deviation. In the tab. 4.7 and fig. 4.23 - 4.26 the results are presented. For the first three test cases, the results are virtually indistinguishable. However, in the last chosen case where the fault occurs on the line 26-28, the grid with VSG does not lose synchronism. On the contrary, the grid with conventional generators is unstable. It should be noted that the grid with VSG during simulation almost reaches to the stability limit though maintaining synchronism as fig. 4.26 shows.

### 4.3.5 Control performance

One of the common tests for control quality assessment is the load test. Sudden change in load is common in an electric grid. Therefore, the subsection presents a modified load change test to assess frequency regulation thoroughly. The test case is as follows, in the IEEE 39 bus system, two nodes (8 and 16) have variable loads. Those loads can suddenly change during operation $\pm 50MW$. A random change occurs every $50s$ for each load and with time shift between loads is $25s$. Fig. 4.27 demonstrates how the loads variate during simulation. The simulation is run for $10800s$ to generate enough data for the following computation. Then the grid frequency is sampled, and the number of samples is counted for different frequency ranges. Thus, the tightness of frequency control can be assessed.

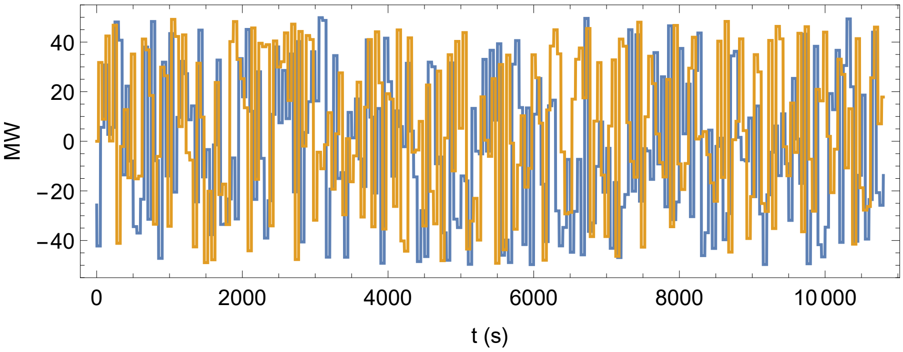

Figure 4.27: Load variation during simulation

Fig. 4.28 shows the histogram of the percentage of samples for different frequency deviations in the system with only synchronous generators. For the conventional grid, the results are as follows: 78.91% of time the frequency is in ±0.1% range of nominal value, 96% of time the frequency is in ±0.15% range of $f_n$ and

100% of time in range ±0.25%. The results of computation for the system with VSG are shown in fig. 4.29. The grid's performance with VSG is quite similar to the conventional grid as expected. During the whole simulation, the frequency is maintained in ±0.25% of $f_n$ range. However, there are small differences: only 75% of time the frequency is in ±0.1% range of nominal value and 94.67% of time in ±0.15% of $f_n$. The resented results prove that frequency control in the system with VSG is essentially similar to the conventional grid.

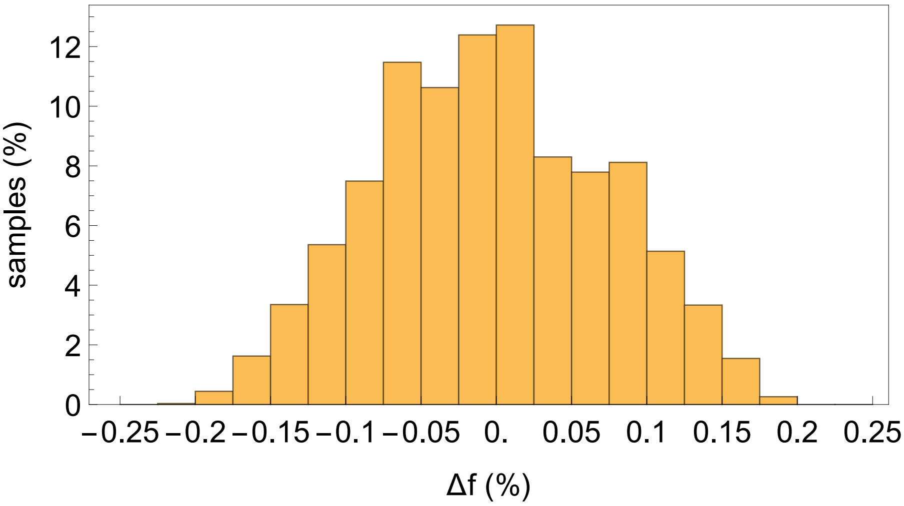

Figure 4.28: Frequency distribution for the conventional system

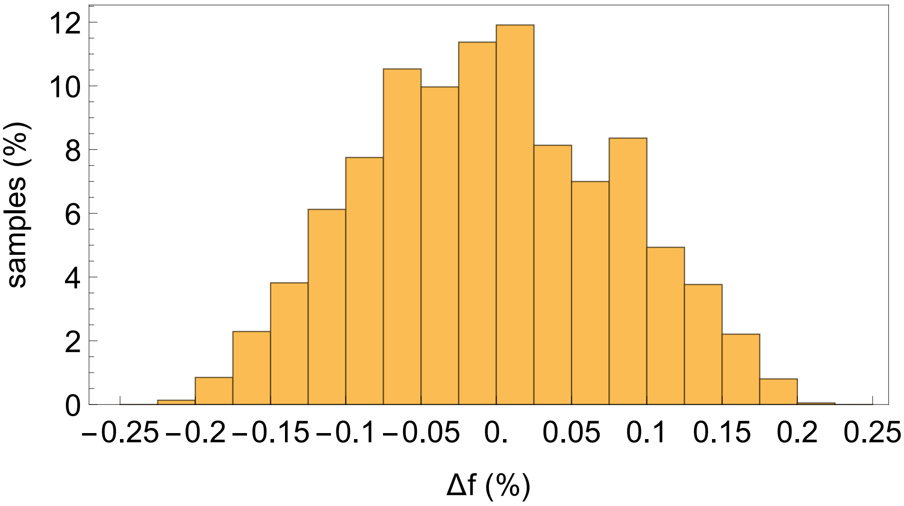

Figure 4.29: Frequency distribution for the system with VSG

### 4.3.6 Summary of the presented analysis

This section briefly summarizes the results presented in the text above. The results of the modal analysis demonstrate that the system with VSG and naive implementation has much worse stability. The system with VSG w/ VS has slightly worse damping than the conventional system. The results of the transient stability study proved that the VSG with naive implementation cannot sustain the long clearing times that can occur in a real power system. In most transient stability studies cases, the system's performance with VSG w/ VS is similar to the conventional grid. However, in one scenario, the system with VSG maintains synchronism, whereas the conventional system is unstable.

Furthermore, the previous section provided results of frequency control quality assessments using a modified load test. The results for the system with VSG were practically the same as for the conventional generators. Hence, this proves that it is possible to replace a synchronous machine without losing the benefits of the inertia provided by it.

# 5. STATCOM with virtual inertia

This chapter investigates the possibility of VSG control application for Static synchronous compensator (STATCOMs). STATCOMs can be used for improving transient stability of the system [46]. The previous chapter demonstrated that grid-forming VSG is superior to other topologies. Hence, the case studies presented in this chapter only compare the grid-forming approach to traditional vector control. A thorough stability analysis of a system with STATCOM is presented hereafter. The region of attraction is estimated using Lyapunov theory for a SMIB case. The results of the analysis illustrate the benefits that VSG control brings if applied to the STATCOMs. Furhtermore, the conclusions reached by analyzing the SMIB case are validated in a larger IEEE 39 bus benchmark system.

## 5.1 Stability of STATCOM with virtual inertia

This section investigates the system's stability with STATCOM for the SMIB case. Furthermore, two topologies, VSG and vector control, for STATCOM are compared. The system's stability is examined using modal analysis, transient stability, and estimation of the region of attraction for both control topologies of STATCOM.

### 5.1.1 STATCOM model

STATCOM is essentially a VSC connected to the grid, with DC side only providing energy storage. Hence, the equations provided in section 3.2.1 are also valid for the STATCOM. The only difference is that in eq. (3.38) $p_{pv} = 0$, thus the dynamics of the capacitor is described as follows:

$$C_{dc}\frac{dv_{dc}}{dt} = \frac{-p_{vsc}}{v_{dc}} \tag{5.1}$$

The control loops modeling described in section 3.2.2 for vector control do not change for the STATCOM operation. Similarly, the mathematical model of synchronverter in $d-q$ frame provided in section 4.1.1 can be applied to STATCOM.

### 5.1.2 Modal analysis

Fig. 5.1 shows the line diagram of the SMIB system with STATCOM. The generator, for simplicity, is modeled with constant power input and field voltage. Since it is a simple system, the full 7-order model of the generator is used. The steps to obtain the system matrix do not change and can be found in section 4.2.1

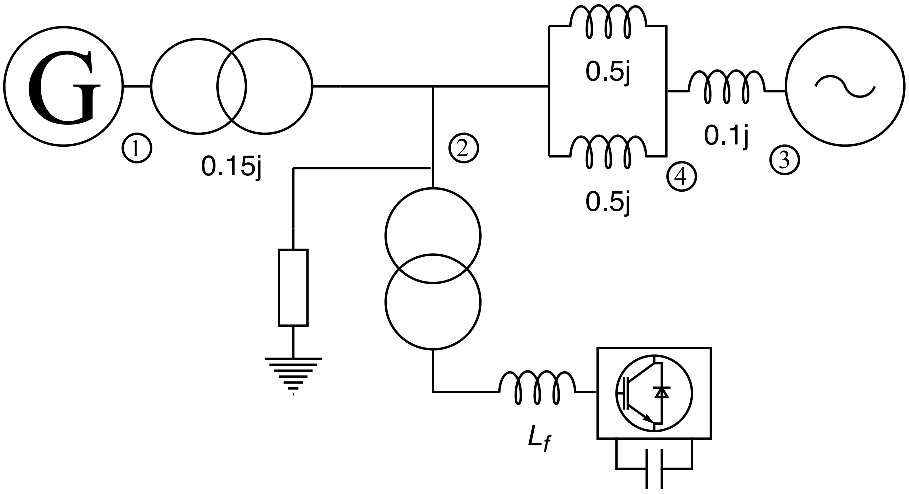

Figure 5.1: Line diagram of SMIB case study system. Adopted from [14]

The computed modes of the SMIB system for different control topologies of the STATCOM are shown in the tab. 5.1 and displayed in fig. 5.2. The red dashed line in fig. 5.2 visualize the lowest damping of the system with synchronverter control, i.e., all modes that lay between $x-$axis and the dashed line have larger damping. As tab. 5.1 shows synchronverter considerably improves the damping and $max(Re(\lambda))$ of the system.

### 5.1.3 Transient stability of SMIB with a STATCOM

This section provides the results of numerical simulations of transients. Firstly, the load change test was conducted in the SMIB system. The load change test is a typical dynamic stability study that demonstrates whether the system can remain stable after a sudden change in load. Also, this test shows the system's ability to damp oscillations and helps to assess the overall quality of control. In the text above, the modal analysis results indicated that synchronverter control should damp oscillations better than traditional vector control.

The load test has the following scenario. In simulation time $t_{sim} = 5s$, the load in node two suddenly increases by 30 MW. The simulation is run for 30 seconds to assess the ability of the system to return to a steady state. Fig. 5.4 and fig. 5.3 show the result of the simulation. Fig. 5.3 demonstrates that

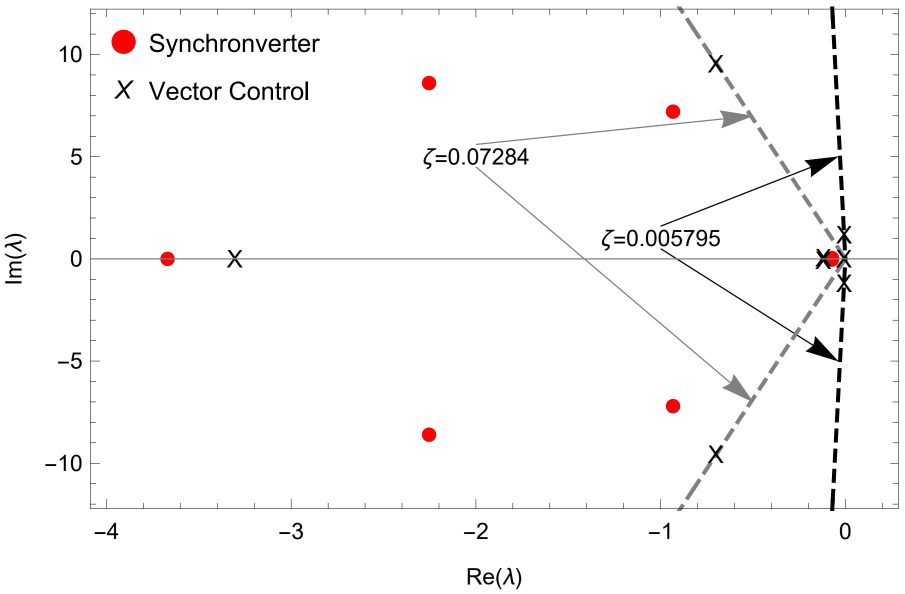

Figure 5.2: The computed eigenvalues of the system.

Table 5.1: Computed eigenvalues of the system with different control strategies

| Control algorithm | Eigenvalues | Min $\zeta$ |
|---|---|---|
| Synchronverter | $-298.122 \pm 2961.75j$,<br>$\mathbf{-74.0969 \pm 1014.53j}$,<br>$-96.4019 \pm 258.276j$,<br>$-2.25383 \pm 8.60414j$,<br>$-0.93304 \pm 7.20548j$,<br>$-6.29137$, $-3.66956$,<br>$-0.0725057 \pm 0.0357883j$ | 0.07284 |
| Vector control | $-61.2246 \pm 1341.88j$,<br>$-11.2496 \pm 864.238j$,<br>$-11.8959 \pm 10.7522j$,<br>$-0.700878 \pm 9.55667j$,<br>$-6.29137$, $-3.30489$,<br>$\mathbf{-0.00686874 \pm 1.18525j}$,<br>$-0.119065 \pm 0.0612463j$,<br>$-0.00749973 + 0j$ | 0.005795 |

synchronverter control has better damping and reaches steady-state much faster, supporting the modal analysis results. The voltage deviation in node 2 during simulation is higher in case of synchronverter (fig. 5.4 ). However, the reference value is reached much faster than in the case of vector control.

The quality of regulation can be quantified by using the following metrics. Most commonly, the integral of the absolute values of the error and integral of the squared error are used [14]. The first metric shows the total area of the error during a transient. The second metric emphasizes the higher deviation

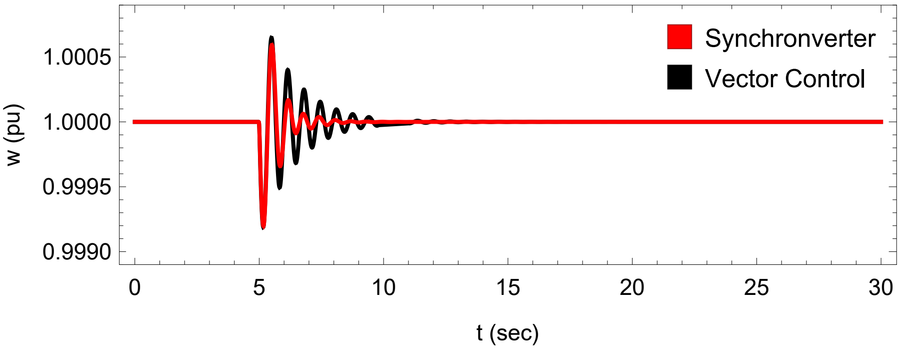

Figure 5.3: The angular velocity of the generator during simulation.

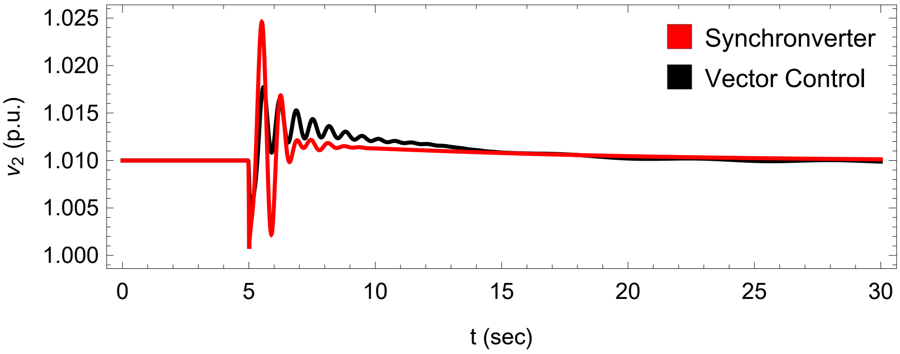

Figure 5.4: The voltage in node 2 during simulation.

Table 5.2: Load test: quality of control

| Control algorithm | Load change | $\int \lvert v_2 - v_{ref} \rvert \mathrm{d}t$ | $\int \lvert v_2 - v_{ref} \rvert^2 \mathrm{d}t$ |
|---|---|---|---|
| Synchronverter | $30MW$ | $24.928 * 10^{-3}$ | $92.216 * 10^{-6}$ |
| | $45MW$ | $35.979 * 10^{-3}$ | $197.525 * 10^{-6}$ |
| | $60MW$ | $46.129 * 10^{-3}$ | $334.415 * 10^{-6}$ |
| Vector control | $30MW$ | $28.039 * 10^{-3}$ | $79.091 * 10^{-6}$ |
| | $45MW$ | $40.405 * 10^{-3}$ | $165.057 * 10^{-6}$ |
| | $60MW$ | $51.669 * 10^{-3}$ | $271.667 * 10^{-6}$ |

from the reference. Several simulations of the load change test were conducted to assess the quality of control. The results of the simulations are presented in tab. 5.2. The comparison of control quality is similar to the load test that is shown ion the fig. 5.4 and 5.3. The overall area of the error is smaller in every case for the synchronverter control since the system with the synchronverter is able to damp oscillations faster. However, the squared error is smaller for the vector control because it does not allow higher deviation from reference though damping oscillations take a longer time. To sum up, the synchronverter is the preferable choice if the primary purpose of the utilized STATCOM to damp power system oscillations, which are a major problem in interconnected areas [39, 46].

Another common transient stability study is the three-phase fault, which is the most severe disturbance n a power system. In the case study, the following scenario was realized. The fault occurs on a transmission line between nodes 2 and 4. After the fault is cleared, the faulty line is disconnected. Therefore, the impedance between nodes 2 and 4 increases by a factor of two. The scenario of this case study is following the system is in steady-state before the three-phase fault occurs. The fault occurs in simulation time $-t_{cl}$ and the fault is cleared in time $t_{sim} = 0s$. The simulation is run for 5 s after the fault is cleared since it is enough time for the system to almost return to a quasi steady-state. Again in this study, two clearing times are considered 100ms and 200 ms.

The results for the $t_{cl} = 0.1s$ are shown in fig. 5.5 and fig. 5.6. The simulation results demonstrate that the system for both control topologies for STATCOM is stable. As fig. 5.5 shows, the load angle increase during the fault is smaller in the case of a synchronverter. The speed deviation from nominal value as well 5.6. It happens in consequence of the increased overall inertia of the system in the presence of a synchronverter. The results for clearing time of 200 ms is presented in fig. 5.7 and fig. 5.8. The vector control is unstable for that clearing time. Synchronverter, on the other hand, performs pretty well. The system almost returns to the steady-state in 5 s after the disturbance.

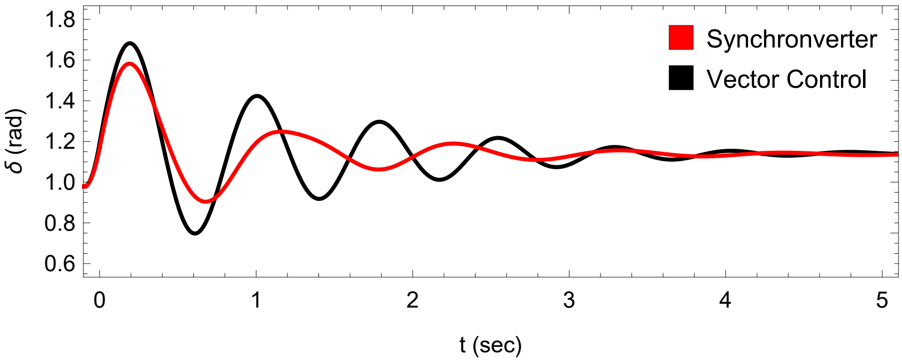

Figure 5.5: The load angle of the generator during simulation of three-phase short circuit for $t_{cl} = 0.1s$.

### 5.1.4 Region of attraction

This subsection estimates the regions of attraction for both examined control topologies. For the analysis, simplified models are used as was explained in the third chapter. Nevertheless, the results of the analysis provided a reasonable estimation for the region of attraction.

Firstly, the estimation of the region of attraction for the system with vector control is done. Fig. 5.9 shows the equivalent circuit with STATCOM. For the analysis, the second-order model of the generator is utilized as section 2.3.5

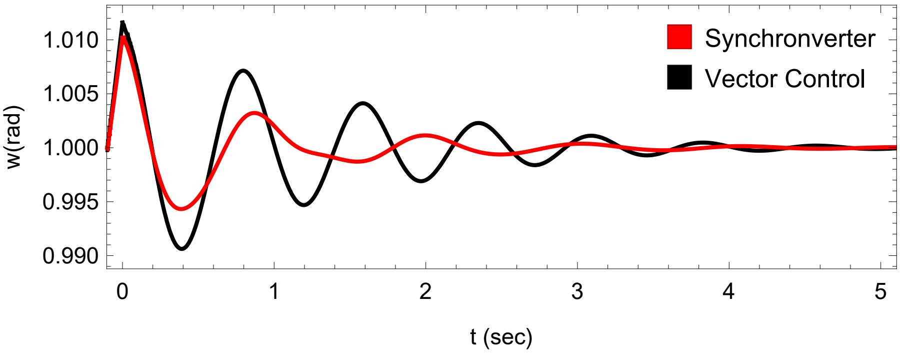

Figure 5.6: The angular velocity of the generator during simulation of three-phase short circuit for $t_{cl} = 0.1s$.

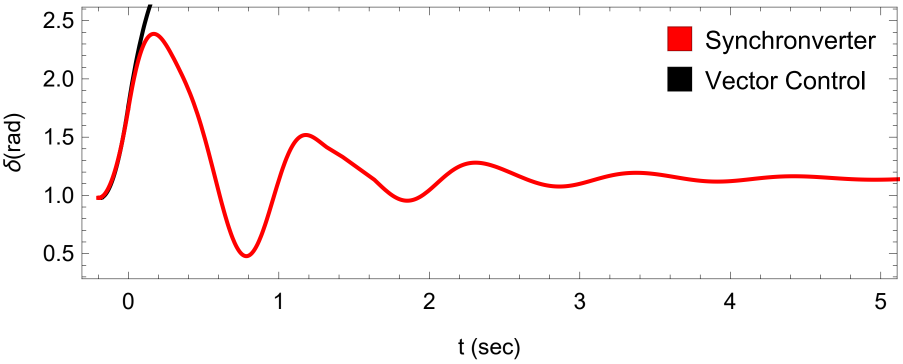

Figure 5.7: The load angle of the generator during simulation of three-phase short circuit for $t_{cl} = 0.2s$.

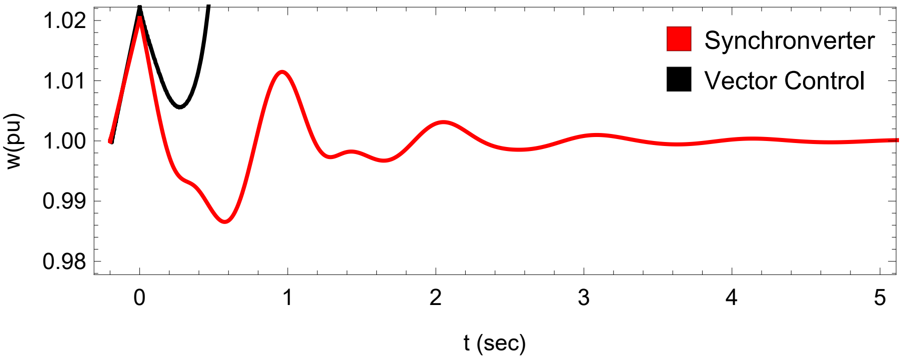

Figure 5.8: The angular velocity of the generator during simulation of three-phase short circuit for $t_{cl} = 0.2s$.

outlines. For the convinience, the subsection restates the model for the analysis:

$$\delta_g = \Delta\omega \tag{5.2}$$

$$J\frac{\mathrm{d}\omega}{\mathrm{d}t} = P_{mech} - P_{el} - D\Delta\omega \tag{5.3}$$

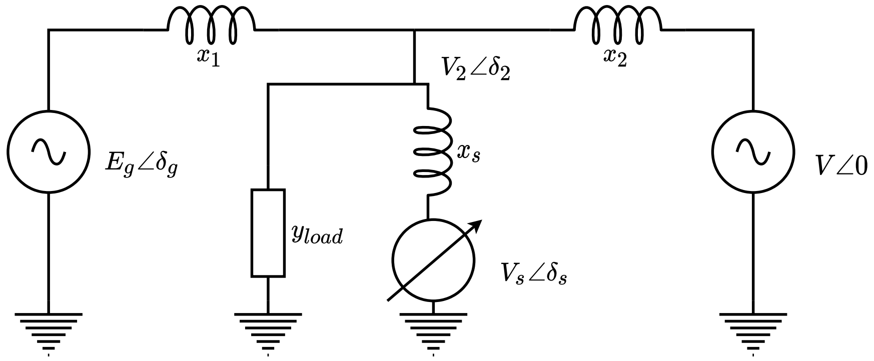

Figure 5.9: The equivalent circuit of the system with STATCOM. Reprinted from [14].

The power produced by the generator is as follows:

$$P_{el} = Re(E_g e^{j\delta_g} I_g^*) \tag{5.4}$$

The current injected by the generator:

$$I_g = \frac{E_g e^{j\delta_g} - V_2 e^{j\delta_2}}{jx_1} \tag{5.5}$$

However, the voltage in node two should be written in terms of STATCOM voltage and grid voltage as in [14, 58] The STATCOM injects current, which is equal to:

$$I_s = \frac{V_s e^{j\delta_s} - V_2 e^{j\delta_2}}{jx_s} \tag{5.6}$$

where $x_s = \omega L_f + \omega L_t$ reactance is a sum of filter and a transformer reactances.

The current flowing into the grid:

$$I_{grid} = \frac{V_2 e^{j\delta_2} - V}{jx_2} \tag{5.7}$$

Thus, the current Kirchhoff law for the node 2 is:

$$I_g + I_s + I_{grid} + y_{load} V_2 e^{j\delta_2} = 0 \tag{5.8}$$

where $y_{load}$ is load admittance.

By solving eq. (5.6) - (5.8) the voltage in second node can be obtained in terms of voltage of STATCOM and grid voltage. Then in eq. (5.4) the $V_2$ can be substituted, and the formula for power injected by generator obtained.

After that, the Lyapunov function can be defined as follows:

$$V(\omega, \delta_g) = \frac{1}{2}J\Delta\omega^2 + \int_{\delta_g(0)}^{\delta_g} (-P_{mech} + P_{el} + D\Delta\omega)\mathrm{d}\delta_g \tag{5.9}$$

And critical value of the function is calcualated as in [36]

$$V_{critical} = \int_{\delta_g(0)}^{\pi-\delta_g(0)} (-P_{mech} + P_{el})\mathrm{d}\delta_g \tag{5.10}$$

The region of attraction of the postfault equilibrium is visualized in fig. 5.18b, as was explained in the second chapter, it is given by the set where $V(\omega, \delta_g) < V_{critical}$. The region oif attraction gives the bounded set of initial conditions that eventually converge to the stable equilibruim $(\delta_{g,stable}, \omega_{stable})$ [14].

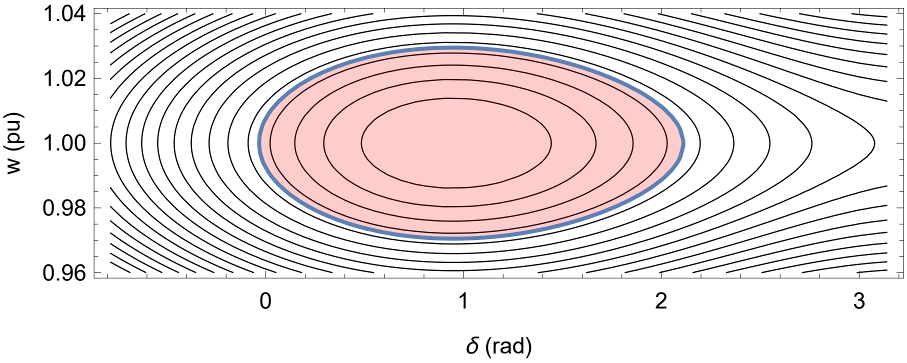

Figure 5.10: The estimated region of attraction of the system with vector control of STATCOM.

The STATCOM controlled using the VSG algorithm can be approximated as a generator for the purpose of the region of attraction estimation. Hence, the inertia of the virtual machine is equal to the inertia that STATCOM provides and the mechanical power input is zero. The simplified model becomes a two-machine system. A number of algorithms exist to estimate the region of attraction for the multimachine system. In this work, the Potential Energy Boundary Surface (PEBS) method is used. This method also estimates critical energy. The second-order model of the generator is used like in the previous computation. The energy function of the i$^{\mathrm{th}}$ generator is:

$$V_i = \frac{1}{2}J\Delta\omega_i^2 + \int_{\delta_i}^{\delta_{i,s}} (-P_{mech,i} + P_{el,i} + D\Delta\omega_i)d\delta_i \tag{5.11}$$

where $(\omega_{i,s}, \delta_{i,s})$ is the stable operating point of the egenerator.

In the PEBS method, the fault-on trajectory is integrated to estimate the critical energy. The maximum of the $V_{PE}$ can be found along the trajectory, which is then considered the critical value $V_{cr}$. The time when the integral of $V_i$ reaches the critical value is the critical clearing time.

Fig. 5.11 vizualizes the energy function of the generator when the second machine (STATCOM)a velocity and load angle is equal to stable values $(\omega_{2,s}, \delta_{2,s})$. It should be emphasized that the PEBS method use assumptions for simplification tha can lead to inacuraces in the result [59].

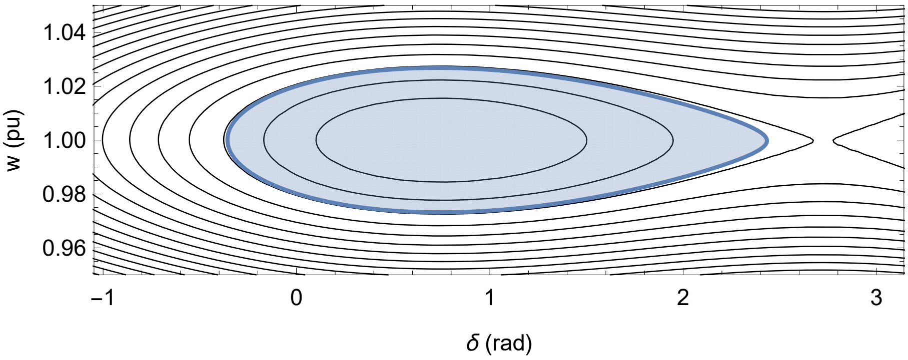

Figure 5.11: The estimated region of attraction of the system with VSG control of STATCOM.

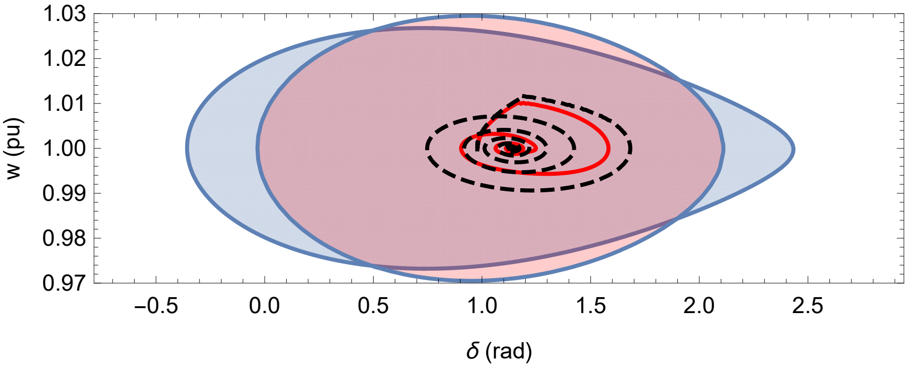

(a) Three-phase fault $t_{cl} = 0.1s$.

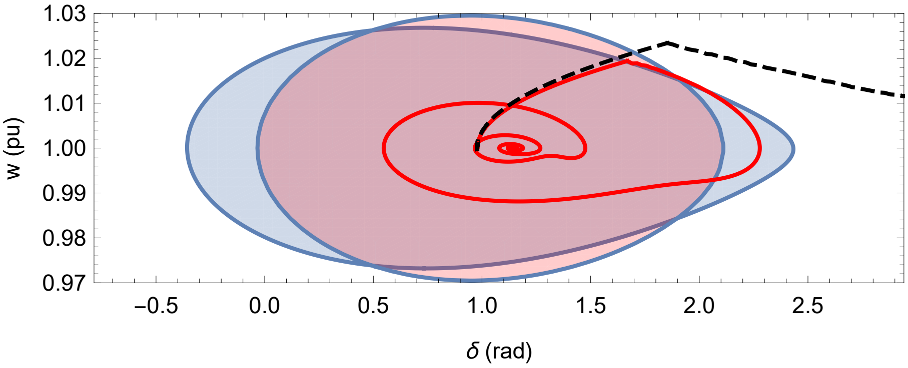

(b) Three-phase fault $t_{cl} = 0.2s$.

Figure 5.12: The region of attraction of the system with synchronverter (Blue), system with vector control (Pink) and the phase-space transient trajectories system with synchronverter (Red), system with vector control (Dashed, Black)

Fig. 5.12 shows the estimated regions of attraction for both control strategies and the phase plot of the fault-on trajectories that were presented in the previous section. It is clear that in the case of the synchronverter, the region of attraction is slightly larger. Nevertheless, there is not much difference. The main difference between two examined control topologies is in the fault-on trajectory. Fig. 5.12b demonstrates that the generator leaves the stable region in the case of vector control. The system with VSG control of STATCOM, on the other hand, remains in the stable region. The main difference is in the total inertia of the system. Hence, the generator speeds up slower and does not leave the region of attraction.

## 5.2 Verification of the results and summary

The previous section analyzed the application of the VSG algorithm for a STATCOM in the SMIB test system. The analysis in SMIB systems gave valuable information and allowed the investigation into the effects of the control algorithm thorougly. Nevertheless, the results provided were obtained for a system with only one generator. This section analyzes the application of virtual inertia to the STATCOM in a larger power system. Furthermore, the interaction of two STACTCOMS are investigated hereafter. This section allows investigating whether the control algorithm of the STATCOMS affects the overall stability of the system. At the end the summary of the examined approach is provided.

### 5.2.1 Validtion in IEEE 39 bus system

IEEE 39 bus system, which was used in the previous studies, was chosen for this analysis. Firstly, the small-signal stability of the system is analyzed. The section presents the analysis of two possible connections of STATCOMs. The first case is STATCOMs are connected to nodes 14 and 18, and the second is for the 14 and 26 nodes. Fig. 5.13 shows the eigenvalues and the system for the first case. It is clear that the damping in the case of the synchronverter is slightly better. Furthermore, the $max(Re(\lambda))$ is smaller for the vector control. Overall, the results are somewhat similar to the conclusions of the previous section. The modes of the system with STATCOMs connected to nodes 14 and 26 are displayed in fig. 5.14. In the second case, the damping of the system with vector control of STATCOMs is much worse than for the VSG control. Similarly, the $max(Re(\lambda))$ is smaller for vector control, hence the system returns to steady-state longer.

To study the transient stability of the system with STATCOMs, a simulation of a three-phase short circuit was done. The scenario is quite similar to the SMIB case. The fault occurs on the line between nodes 15 and 16 (line diagram of the system is shown in fig. 4.13). Then the faulty line is disconnected. Again two clearing times are considered.

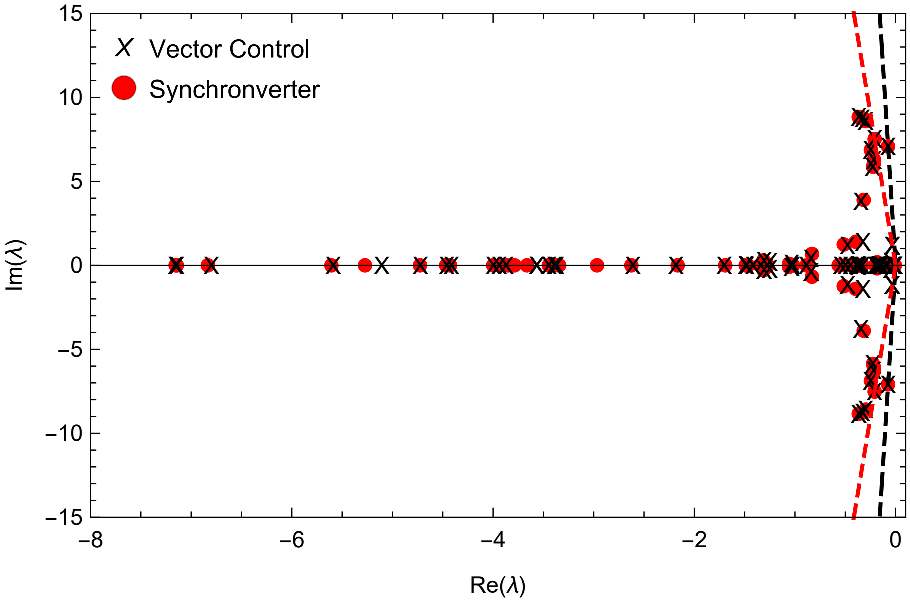

Figure 5.13: Eigenvalues of the system with STATCOMs connected to nodes 14 & 18

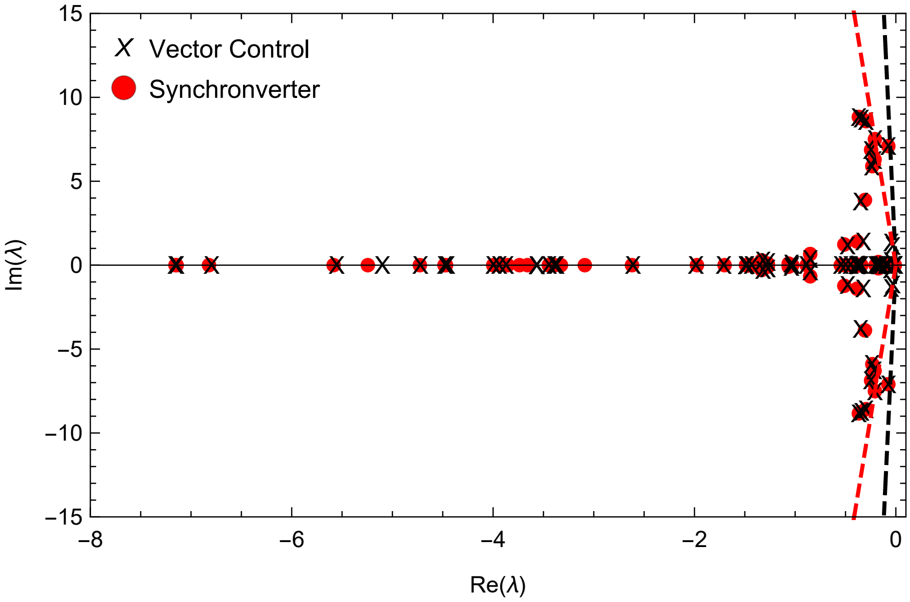

Figure 5.14: Eigenvalues of the system with STATCOMs connected to nodes 14 & 26

The results of the simulations are presented in fig.5.15, 5.16,5.17, 5.18. The results of transient stability analysis are not surprising. Vector control is unstable in both cases for a clearing time of 200 ms. Similar results were obtained in the analysis of the SMIB case. The damping of oscillations is slightly better in the case of VSG control of STATCOM. Tab. 5.3 summarizes the results of comparison. To conclude, the STATCOM with VSG control topology indeed provides inertia to the system, thus improving the overall stability. The damping is also better in the case of VSG control of the STATCOMs.

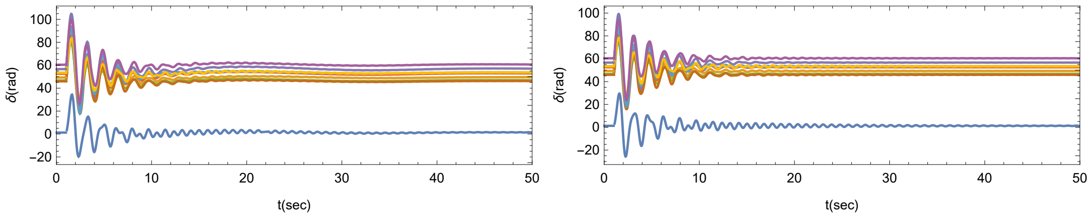

(a) Load angles of generators during transient. STATCOM utilizes vector control.
(b) Load angles of generators during transient. STATCOM utilizes VSG control.

Figure 5.15: Statcoms connected to nodes 14&18. Clearing time is 100ms.

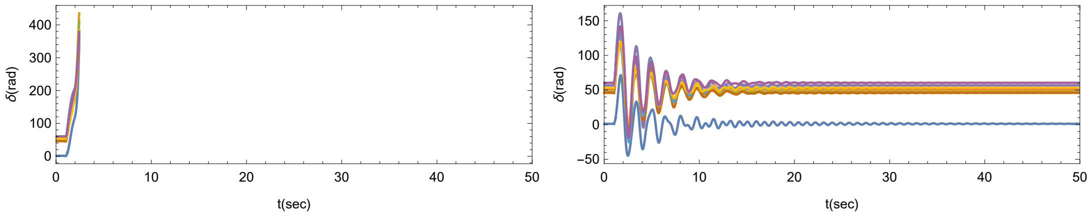

(a) Load angles of generators during transient. STATCOM utilizes vector control.
(b) Load angles of generators during transient. STATCOM utilizes VSG control.

Figure 5.16: Statcoms connected to nodes 14&18. Clearing time is 200ms.

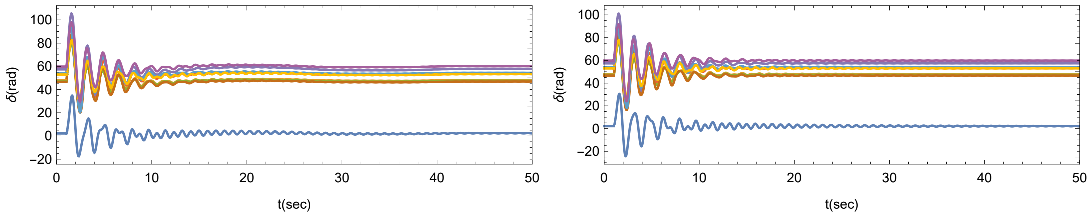

(a) Load angles of generators during transient. STATCOM utilizes vector control.
(b) Load angles of generators during transient. STATCOM utilizes VSG control.

Figure 5.17: Statcoms connected to nodes 14&26. Clearing time is 100ms.

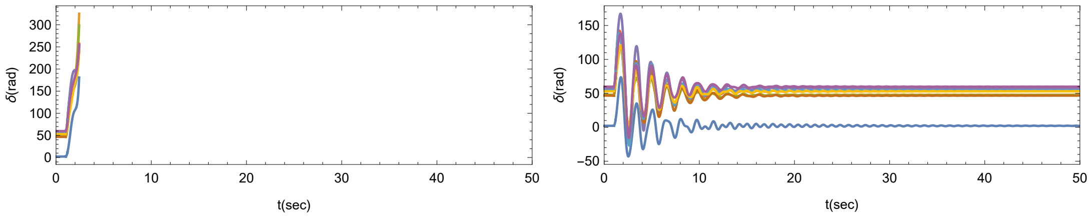

(a) Load angles of generators during transient. STATCOM utilizes vector control.
(b) Load angles of generators during transient. STATCOM utilizes VSG control.

Figure 5.18: Statcoms connected to nodes 14&26. Clearing time is 200ms.

### 5.2.2 Summary of the proposed VSG control for STATCOM.

This chapter investigated the application of grid-forming control algorithm to the STATCOMs. Firstly, the modal analysis of the SMIB system with differ-

Table 5.3: Performance of control strategies in IEEE 39 bus system

| | $t_{cl}$ | | 14&18 | 14&26 |
|---|---|---|---|---|
| Synchronverter | $0.1s$ | $\min\zeta$ | 0.01066 | 0.01055 |
| | | $\max(Re(\lambda))$ | $-0.0073$ | $-0.01028$ |
| | | $\max\delta$ | 99.3° | 101.2° |
| | | $\max\Delta f$ | 0.43 Hz | 0.44 Hz |
| | $0.2s$ | $\max\delta$ | 160.1° | 167.3° |
| | | $\max\Delta f$ | 0.95 Hz | 0.96 Hz |
| Vector Control | $0.1s$ | $\min\zeta$ | 0.01056 | 0.0079 |
| | | $\max(Re(\lambda))$ | $-0.0021$ | $-0.0021$ |
| | | $\max\delta$ | 104.8° | 105.6° |
| | | $\max\Delta f$ | 0.45 Hz | 0.45 Hz |
| | $0.2s$ | | unstable | unstable |

ent control topologies of STATCOM was carried out. The results of the small-signal stabilty determined that in terms of damping and eigenvalue placement the system with VSG control outperforms the traditional one. Then, the transient stability studies were condicted. The results of the transient stability overall confirmed the results of the modal analysis. Furthermore, in the prtesented SMIB case the system with synchronverter control of STATCOM was able to sustain longer clearing times. The chapter also presents an estimation of region of attraction for both control strategies in SMIB system. The region of attraction in case of traditional vector control is slightly smaller. Nevertheless, the main differnce is in the fault-on trajectory of the system. As fig. 5.12 demonstrates the system with virtual inertia indeed does not speed up as much, thus remaining in the stable region. Afterwards, the author examined the effects of VSG control for STATCOMs in a larger power system using modal analysis and numerical simulations of transients. The results in the larger IEEE 39 bus benchmark system supported the conclusions of the analyses conducted in SMIB case. In conclusion, the VSG control is suitable for STATCOMs and do not requier fundamental changes to the hardware. Furthermore, the STATCOMs with virtual inertia improve the transient and small-signal stability of the system.

# 6. Conclusion and Future Work

## 6.1 Summary

Modern power systems have been transitioning towards more sustainable power generation during the last two decades. The zero-carbon grid has tremendous support worldwide. Hence, this trend will probably continue. However, the replacement of conventional generation creates new challenges for grid operators. The inertia response provided by synchronous generators covers the immediate power imbalance. New control techniques have to be utilized to increase the share of RES in the power system. Many researchers concluded that virtual inertia provided by RES power plants could be a solution. CIGs using virtual inertia implementation can potentially be integrated into the grid without significant changes to the power system since they will emulate synchronous generators.

This thesis investigates the grid-forming control of power converters and compares it to other topologies. A grid-forming virtual synchronous generator can potentially replace a SG and provide an inertia response similar to the SG. The thesis firstly outlines different control topologies that can implement virtual inertia. Next, the issue of power system stability is outlined in the text. The main aspects of different types of power system stability are discussed. Also, mathematical tools and modeling for power system analysis are described. Two chapters focus on comparing grid-forming control of CIGs to other control strategies. One of the chapters focuses on PV power plant integration into the grid and analysis the effects of the control on power system stability. The chapter on the application of VSG control for STATCOMs investigates the possibility and conducts a thorough stability analysis.

The thesis presents the results of the research into the application of grid-forming control and its effects on the stability of a power system. In the fourth chapter, firstly, in a common IEEE 9 bus benchmark system, three control topologies are compared. The results of the comparison yielded that grid-forming control improves the small-signal stability and transient stability of the system. It increases the lowest damping of the system and moves eigenvalues to the left i.e. the system returns to steady-state faster. Grid-following control (RoCoF topology) also by implementing virtual inertia enhances the stability of the system compared to traditional vector control. Nevertheless, grid-following control, by all means, has worse stability characteristics than a grid-forming one. Furthermore, the author carries out a study on the effects of virtual inertia placement and the algorithm used for the implementation on the overall stability of the grid using IEEE 39 bus benchmark system. The results of the modal analysis conclude that the placement and control topology utilized for virtual inertia implementation has a major impact on the stability characteristics of the power system. Ultimately, the conducted comparison determined that grid-forming control is preferable to other topologies.

Furthermore, this thesis investigates a way to increase virtual inertia capability by utilizing an Energy Storage System. Also, the author proposes a DC bus voltage stabilizer that improves the system's stability. Modal analysis of the proposed improved control is comparable to a conventional SG. In terms of transient stability, the VSG with ESS is similar to SG. Moreover, in one of the presented cases, the system with VSG remains stable, whereas the conventional system does not. To sum up, the proposed control for grid-forming VSG with ESS allows the replacement of SG without losing the benefits of inertia response.

Lastly, the author examines the possibility of grid-forming control application to STATCOMs. Initially, the stability of the SMIB with STATCOM is analyzed thoroughly. The modal analysis concluded that the small-sgnal stability of the system is improved compared to traditional control. Furthermore, numerical simulations of transients supported the conclusion. Besides, the application of VSG control allows the system to withstand longer clearing times. The fifth chapter also proved an estimation of the region of attraction for both examined topologies. The results concluded that the region of stability does not change much, but the fault-on trajectory does. Since the virtual inertia increases the system's overall inertia, the generator does not accelerate as much, thus remaining in the stable region. Also, the achieved results are then verified in a larger power system. Modal analyses and numerical simulations supported the conclusions reached by analyzing simple SMIB cases.

In conclusion, this thesis demonstrates the grid-forming approach has the potential to be applied in different cases. Mainly it can integrate RES in such a way that the system's stability is not affected. Furthermore, the proposed control improvements for VSG with ESS can possibly replace a SG. This work also shows that grid-forming control can be applied not only to RES power plants but to STATCOMs as well.

## 6.2 Future work

This thesis demonstrates the application of grid-forming VSG can bring benefits and increase the penetration of RES. The author proposed a DC bus voltage stabilizer for VSG with ESS that improves stability and allows to replace SG. Developing ESS models for power system stability studies and improving control of VSG can be very beneficial for the integration of RES. Also, the utilization of ESS with virtual inertia can increase the flexibility of the grid. Furthermore, in the future, such power generation units can provide services for the grid operator in managing system inertia. As COVID lockdowns demonstrated, different conditions can emerge and force grid operators to use conventional power plants. Such conditions should be thoroughly studied to prevent further undesirable power outages.

Overall, new control techniques for power converters are beneficial not only for the integration of the renewables but can improve the conventional grid and take advantage of the potential of existing devices such as STATCOM. A STATCOM with virtual inertia is an interesting proposition that can be employed without changing the hardware.

Also, future studies will focus on investigating the transition of a power system's part with VSG into island mode. The stability studies of larger interconnected grids with grid-forming control are also required to examine the effects in weakly coupled interconnected areas.

# Bibliography

[1] bp p.l.c., “Statistical review of world energy,” 2021.

[2] ENTSO-E, “Central collection and publication of electricity generation.”

[3] AEMO, “Update report-black system event in south australia on 28 september 2016,” 2016.

[4] L. Badesa, G. Strbac, M. Magill, and B. Stojkovska, “Ancillary services in great britain during the covid-19 lockdown: A glimpse of the carbon-free future,” *Applied Energy*, vol. 285, p. 116500, 2021.

[5] F. Milano, F. Dörfler, G. Hug, D. J. Hill, and G. Verbič, “Foundations and challenges of low-inertia systems (invited paper),” in *2018 Power Systems Computation Conference (PSCC)*, pp. 1–25, 2018.

[6] N. Hatziargyriou, J. Milanovic, C. Rahmann, V. Ajjarapu, C. Canizares, I. Erlich, D. Hill, I. Hiskens, I. Kamwa, B. Pal, P. Pourbeik, J. Sanchez-Gasca, A. Stankovic, T. Van Cutsem, V. Vittal, and C. Vournas, “Definition and classification of power system stability - revisited and extended,” *IEEE Transactions on Power Systems*, vol. 36, no. 4, pp. 3271–3281, 2021.

[7] Hydro-Québec, “Technical requirements for the connection of generating stations to the hydro-québec transmission system,” 2019.

[8] eneginet, “Technical regulation 3.2.5 for wind power plants above 11 kw,” 2016.

[9] ENTSO-E, “Need for Synthetic Inertia (SI) for Frequency Regulation,” 2018.

[10] M. Nedd, C. Booth, and K. Bell, “Potential solutions to the challenges of low inertia power systems with a case study concerning synchronous condensers,” pp. 1–6, 2017.

[11] ČEPS, “Kodex přenosové soustavy - část vi.,” 2020.

[12] Nationalgrid, “Electricity ten year statement 2014,” 2014.

[13] A. Saffarian and M. Sanaye-Pasand, “Enhancement of power system stability using adaptive combinational load shedding methods,” *IEEE Transactions on Power Systems*, vol. 26, no. 3, pp. 1010–1020, 2011.

[14] L. Vetoshkin and Z. Müller, “Dynamic Stability Improvement of Power System by Means of STATCOM With Virtual Inertia,” *IEEE Access*, vol. 9, pp. 116105–116114, 2021.

[15] L. Vetoshkin and Z. Müller, “A comparative analysis of a power system stability with virtual inertia,” *Energies*, vol. 14, p. 3277, 06 2021.

[16] A. Riaz, M. R. Sarker, M. H. M. Saad, and R. Mohamed, “Review on comparison of different energy storage technologies used in micro-energy harvesting, wsns, low-cost microelectronic devices: Challenges and recommendations,” *Sensors*, vol. 21, no. 15, 2021.

[17] A. Z. AL Shaqsi, K. Sopian, and A. Al-Hinai, “Review of energy storage services, applications, limitations, and benefits,” *Energy Reports*, vol. 6, pp. 288–306, 2020. SI:Energy Storage - driving towards a clean energy future.

[18] EirGrid/SONI, “Rocof modification proposal - tsos’ recommendations,” 2012.

[19] M. Taul, X. Wang, P. Davari, and F. Blaabjerg, “An overview of assessment methods for synchronization stability of grid-connected converters under severe symmetrical grid faults,” *IEEE Transactions on Power Electronics*, vol. PP, pp. 1–1, 02 2019.

[20] U. Tamrakar, D. Shrestha, M. Maharjan, B. P. Bhattarai, T. M. Hansen, and R. Tonkoski, “Virtual inertia: Current trends and future directions,” *Applied Sciences*, vol. 7, no. 7, 2017.

[21] R. Ofir, U. Markovic, P. Aristidou, and G. Hug, “Droop vs. virtual inertia: Comparison from the perspective of converter operation mode,” 02 2018.

[22] L. Sun, P. Wang, F. Jiang, W. Zhang, M. Zhong, and Y. Wang, “Adaptive virtual inertia control method based on droop control,” pp. 01–06, 2021.

[23] J. Liu, Y. Miura, and T. Ise, “Comparison of dynamic characteristics between virtual synchronous generator and droop control in inverter-based distributed generators,” *IEEE Transactions on Power Electronics*, vol. 31, no. 5, pp. 3600–3611, 2016.

[24] S. D’Arco, J. A. Suul, and O. B. Fosso, “A virtual synchronous machine implementation for distributed control of power converters in smartgrids,” *Electric Power Systems Research*, vol. 122, pp. 180–197, 2015.

[25] Q.-C. Zhong and G. Weiss, “Synchronverters: Inverters that mimic synchronous generators,” *IEEE Transactions on Industrial Electronics*, vol. 58, no. 4, pp. 1259–1267, 2011.

[26] L. Vetoshkin and Z. Müller, “A comparative study of synchronverter stability,” pp. 1–6, 2020.

[27] Q.-C. Zhong, “Four-quadrant operation of ac machines powered by inverters that mimic synchronous generators,” in *5th IET International Conference on Power Electronics, Machines and Drives (PEMD 2010)*, pp. 1–6, 2010.

[28] P. Tielens and D. V. Hertem, “The relevance of inertia in power systems,” *Renewable and Sustainable Energy Reviews*, vol. 55, pp. 999–1009, 2016.

[29] A. Ulbig, T. S. Borsche, and G. Andersson, “Impact of low rotational inertia on power system stability and operation,” *IFAC Proceedings Volumes*, vol. 47, no. 3, pp. 7290–7297, 2014. 19th IFAC World Congress.

[30] M. Saeedian, B. Pournazarian, S. S. Seyedalipour, B. Eskandari, and E. Pouresmaeil, “Emulating rotational inertia of synchronous machines by a new control technique in grid-interactive converters,” *Sustainability*, vol. 12, no. 13, 2020.

[31] J. Khazaei, Z. Tu, and W. Liu, “Small-signal modeling and analysis of virtual inertia-based pv systems,” *IEEE Transactions on Energy Conversion*, vol. 35, no. 2, pp. 1129–1138, 2020.

[32] U. Markovic, O. Stanojev, P. Aristidou, E. Vrettos, D. Callaway, and G. Hug, “Understanding small-signal stability of low-inertia systems,” *IEEE Transactions on Power Systems*, vol. 36, no. 5, pp. 3997–4017, 2021.

[33] J. Alipoor, Y. Miura, and T. Ise, “Power system stabilization using virtual synchronous generator with alternating moment of inertia,” *IEEE Journal of Emerging and Selected Topics in Power Electronics*, vol. 3, no. 2, pp. 451–458, 2015.

[34] S. Coffey, V. Timmers, R. Li, G. Wu, and A. Egea-Àlvarez, “Review of mvdc applications, technologies, and future prospects,” *Energies*, vol. 14, no. 24, 2021.

[35] P. Kundur, J. Paserba, V. Ajjarapu, G. Andersson, A. Bose, C. Canizares, N. Hatziargyriou, D. Hill, A. Stankovic, C. Taylor, T. Van Cutsem, and V. Vittal, “Definition and classification of power system stability ieee/cigre

joint task force on stability terms and definitions," *IEEE Transactions on Power Systems*, vol. 19, no. 3, pp. 1387–1401, 2004.

[36] P. Kundur, *Power System Stability and control.* McGraw Hill, 1994.

[37] A. J. Van Der Schaft and J. M. Schumacher, *An introduction to hybrid dynamical systems*, vol. 251. Springer London, 2000.

[38] P. Anderson and A. Fouad, *Power System Control and Stability.* IEEE Press, 1993.

[39] "Control of power system oscillations," *IFAC Proceedings Volumes*, vol. 30, no. 17, pp. 75–83, 1997. IFAC Symposium on Control of Power Plants and Power Systems (CPSPP'97), Beijing, China, 18-21 August 1997.

[40] K. J. Astrom and R. M. Murray, *Feedback systems.* Princeton, NJ: Princeton University Press, Apr. 2008.

[41] P. W. Sauer and M. A. Pai, *Power system dynamics and stability.* Stipes Publishing L.L.C., 2006.

[42] "IEEE Guide for Synchronous Generator Modeling Practices and Parameter Verification with Applications in Power System Stability Analyses," *IEEE Std 1110-2019 (Revision of IEEE Std 1110-2002)*, pp. 1–92, 2020.

[43] "IEEE Standard for High-Potential Test Requirements for Excitation Systems for Synchronous Machines," *IEEE Std 421.3-2016 (Revision of IEEE Std 421.3-1997)*, pp. 1–19, 2016.

[44] I. C. Report, "Dynamic models for steam and hydro turbines in power system studies," *IEEE Transactions on Power Apparatus and Systems*, vol. PAS-92, no. 6, pp. 1904–1915, 1973.

[45] P. Pourbeik, G. Chown, J. Feltes, F. Modau, S. Sterpu, R. Boyer, K. Chan, L. Hannett, D. Leonard, L. Lima, W. Hofbauer, L. Gerin-Lajoie, S. Patterson, J. Undrill, and F. Langenbacher, "Dynamic models for turbine-governors in power system studies," 01 2013.

[46] N. G. Hingorani and L. Gyugyi, *Understanding FACTS: Concepts and Technology of Flexible AC Transmission Systems.* Wiley-IEEE Press, 2000.

[47] D. Baimel, J. Belikov, J. M. Guerrero, and Y. Levron, "Dynamic modeling of networks, microgrids, and renewable sources in the dq0 reference frame: A survey," *IEEE Access*, vol. 5, pp. 21323–21335, 2017.

[48] N. Kroutikova, C. Hernandez-Aramburo, and T. Green, "State-space model of grid-connected inverters under current control mode," *Electric Power Applications, IET*, vol. 1, pp. 329 – 338, 06 2007.

[49] J. Rocabert, A. Luna, F. Blaabjerg, and P. RodrĂguez, "Control of power converters in ac microgrids," *IEEE Transactions on Power Electronics*, vol. 27, no. 11, pp. 4734–4749, 2012.

[50] M. Karimi-Ghartema, *Enhanced Phase-Locked Loop Structures for Power and Energy Applications.* Wiley-IEEE Press, 2014.

[51] L. Vetoshkin and Z. Müller, "A supervisory mpc for synchronverter," pp. 1–6, 2020.

[52] R.-C. S. P. . D. S. Group, "Determining generator fault clearing time for the synchronous zone of continental europe," tech. rep., ENTSO-E, 2017.

[53] B. K. Poola, D. Groß, and F. Dörfler, "Placement and implementation of grid-forming and grid-following virtual inertia and fast frequency response," in *2020 IEEE Power Energy Society General Meeting (PESGM)*, pp. 1–1, 2020.

[54] I. Hiskens, " IEEE PES Task Force on Benchmark Systems for Stability Controls," 2013.

[55] L. Yang, Z. Hu, S. Xie, S. Kong, and W. Lin, "Adjustable virtual inertia control of supercapacitors in pv-based ac microgrid cluster," *Electric Power Systems Research*, vol. 173, pp. 71–85, 2019.

[56] A. Tayyebi, D. Gross, A. Anta, F. Kupzog, and F. Dörfler, "Interactions of grid-forming power converters and synchronous machines - a comparative study," 02 2019.

[57] A. Ortega and F. Milano, "Generalized model of vsc-based energy storage systems for transient stability analysis," *IEEE Transactions on Power Systems*, vol. 31, no. 5, pp. 3369–3380, 2016.

[58] M. Haque and P. Kumkratug, "Application of lyapunov stability criterion to determine the control strategy of a statcom," *Generation, Transmission and Distribution, IEE Proceedings-*, vol. 151, pp. 415 – 420, 06 2004.

[59] H.-D. Chiang, F. Wu, and P. Varaiya, "Foundations of direct methods for power system transient stability analysis," *IEEE Transactions on Circuits and Systems*, vol. 34, no. 2, pp. 160–173, 1987.

# List of the author’s publications

## Journal papers with impact factor related to the thesis

- L. Vetoshkin and Z. Müller, ”Dynamic Stability Improvement of Power System by Means of STATCOM With Virtual Inertia,” in IEEE Access, vol. 9, pp. 116105-116114, 2021, doi: 10.1109/ACCESS.2021.3106236.
- L. Vetoshkin and Z. Müller, ”A Comparative Analysis of a Power System Stability with Virtual Inertia,” Energies, vol. 14, no. 11, p. 3277, Jun. 2021, doi: 10.3390/en14113277.

## Conference Papers Related to the Thesis

- L. Vetoshkin and Z. Müller, ”A comparative study of synchronverter stability,” 2020 21st International Scientific Conference on Electric Power Engineering (EPE), 2020, pp. 1-6, doi: 10.1109/EPE51172.2020.9269194.
- L. Vetoshkin and Z. Müller, ”A supervisory MPC for synchronverter,” 2020 21st International Scientific Conference on Electric Power Engineering (EPE), 2020, pp. 1-6, doi: 10.1109/EPE51172.2020.9269232.
- L. Vetoshkin, J. Votava, J. Kyncl and Z. Müller, ”Improvement of transient stability using STATCOM combined with optimization,” 2019 20th International Scientific Conference on Electric Power Engineering (EPE), 2019, pp. 1-5, doi: 10.1109/EPE.2019.8778105.
- J. Votava, J. Kyncl, Z. Müller, L. Vetoshkin and J. Rimbala, ”Primary Energy Reduction Using Small CHP Systems,” 2020 21st International Scientific Conference on Electric Power Engineering (EPE), 2020, pp. 1-6, doi: 10.1109/EPE51172.2020.9269204.

## Conference papers not related to the thesis

- J. Votava, J. Kyncl, Z. Müller, L. Vetoshkin and J. Rimbala, ”Optimized Use of the Steam Accumulator in the Combined Heat and Power Production,” 2019 20th International Scientific Conference on Electric Power Engineering (EPE), 2019, pp. 1-5, doi: 10.1109/EPE.2019.8778141.

# Nomenclature

| | |
|---|---|
| AC | Alternating Current |
| CIG | Converter-generation interface |
| DAE | Differential-Algebraic Equations |
| DC | Direct Current |
| ENTSO-E | European Network of Transmission System Operators for Electricity |
| ESS | Energy Storage System |
| Hz | Hertz |
| IEEE | Institute of Electrical and Electronics Engineers |
| PES | Power Engineering Society |
| PEBS | Potential Energy Boundary Surface |
| PCC | Point of Common Coupling |
| PLL | Phase Locked Loop |
| PV | Photovoltaic |
| PS | Power System |
| PSS | Power System Stabilizer |
| PWM | Pulse Width Modulation |
| RoCoF | Rate of Change of Frequency |
| RES | Renewable Energy Source |
| SC | Supercapacitor |
| SG | Synchrnous Generator |
| SMIB | Single Machine Infinite Bus |
| STATCOM | Static synchronous compensator |
| VS | Voltage Stabilizer |
| VSC | Voltage Scource Converter |
| VSG | Virtual Synchronous Generator |
| VISMA | Virtual Synchronous Machine |

| | |
|---|---|
| $\Delta\mathrm{x}$ | State vector |
| $\delta$ | Load Angle |
| $\omega$ | Angular velocity |
| $\psi$ | Magnetic flux |
| $\zeta$ | Damping ratio |
| $\lambda$ | Eigenvalue |
| $\theta$ | Electrical or Mechanical angle |
| $\mathbf{A}$ | State matrix |
| $\mathbf{B}$ | Input matrix |
| $\mathbf{C}$ | Output matrix |
| $\mathbf{D}$ | Feedforward matrix |
| $d-$axis | Direct axis |
| $q-$axis | Quadrature axis |
| $P$ | Power |
| $J$ | Inertia |
| $T_{dq}$ | Park transformation matrix |
| $T_{el}, T_{mech}$ | Torque electrical or mechanical |
| $t_{cl}$ | Clearing time |
| $D$ | Damping |
| $\mathbf{v}$ | Vector of nodal voltages |
| $\mathbf{i}$ | Vector of current injected at each node |
| $\mathbf{I}$ | Identity matrix |
| $\mathbf{Y}$ | Admitance matrix |
| $f$ | Frequency |
| pu | Per Unit |
| w/ | With |
| w/o | Without |

# List of Figures

# Appendix

## Appendix I. Parameters of VSG w/ ESS

$J_v = 46.5$, $D_p = 0.1$, $K_{p,dc} = 0.79$, $K_{i,dc} = 0.31$, $K_{i,v} = 0.15$, $K_{i,q} = 0.9$, $K_{vs} = 0.03$, $T_{vs} = 46$, $T_1 = 0.05$, $T_2 = 0.025$, $T_3 = 0.0016$, $T_4 = 0.008$, $K_{p,sc} = 0.19$, $K_{i,sc} = 0.159$, $K_{p,ess} = 0.25$, $K_{i,ess} = 0.01$ $D_{dc} = 0.63$, $D_{sc} = 0.3$, $C_{dc} = 1155.7mF$, $C_{sc} = 1643F$, $L_f = 0.135mH$